

DEVELOPMENT OF ROLLING-TYPE PARABOLIC-SURFACE FLOOR  
ISOLATOR (RPF) AND DETERMINATION OF MECHANICAL PROPERTIES

A THESIS SUBMITTED TO  
THE GRADUATE SCHOOL OF NATURAL AND APPLIED SCIENCES  
OF  
MIDDLE EAST TECHNICAL UNIVERSITY

BY

CEM EREN ASLAN

IN PARTIAL FULFILLMENT OF THE REQUIREMENTS  
FOR  
THE DEGREE OF MASTER OF SCIENCE  
IN  
CIVIL ENGINEERING

JANUARY 2026



Approval of the thesis:

**DEVELOPMENT OF ROLLING-TYPE PARABOLIC-SURFACE FLOOR  
ISOLATOR (RPFI) AND DETERMINATION OF MECHANICAL  
PROPERTIES**

submitted by **CEM EREN ASLAN** in partial fulfillment of the requirements for the degree of **Master of Science in Civil Engineering, Middle East Technical University** by,

Prof. Dr. Naci Emre Altun  
Dean, **Graduate School of Natural and Applied Sciences**

\_\_\_\_\_

Prof. Dr. Erdem Canbay  
Head of the Department, **Civil Engineering**

\_\_\_\_\_

Prof. Dr. Uğurhan Akyüz  
Supervisor, **Civil Engineering, METU**

\_\_\_\_\_

**Examining Committee Members:**

Prof. Dr. Ahmet Yakut  
Civil Engineering, METU

\_\_\_\_\_

Prof. Dr. Uğurhan Akyüz  
Civil Engineering, METU

\_\_\_\_\_

Prof. Dr. Eray Baran  
Civil Engineering, METU

\_\_\_\_\_

Prof. Dr. Murat Altuğ Erberik  
Civil Engineering, METU

\_\_\_\_\_

Assist. Prof. Dr. Kaan Kaatsız  
Civil Engineering, Başkent University

\_\_\_\_\_

Date: 16.01.2026

**I hereby declare that all information in this document has been obtained and presented in accordance with academic rules and ethical conduct. I also declare that, as required by these rules and conduct, I have fully cited and referenced all material and results that are not original to this work.**

Name Last name : Aslan, Cem Eren

Signature :

## **ABSTRACT**

### **DEVELOPMENT OF ROLLING-TYPE PARABOLIC-SURFACE FLOOR ISOLATOR (RPFI) AND DETERMINATION OF MECHANICAL PROPERTIES**

Aslan, Cem Eren  
Master of Science, Civil Engineering  
Supervisor: Prof. Dr. Uğurhan Akyüz

January 2026, 132 pages

Acceleration demand acting on non-structural components in buildings can exceed permitted limits and result in significant financial losses. Facilities such as data centers, museums, power transmission systems, and high-technology buildings are particularly vulnerable due to the presence of highly sensitive and costly equipment, often exceeding the value of the structural system itself. Although seismic base isolation is widely adopted to mitigate structural damage, it has been demonstrated that floor-level accelerations in base-isolated buildings may still exceed acceptable limits, resulting in loss of functionality of critical non-structural components. Consequently, further reduction of accelerations transmitted to such elements is of paramount importance. Floor isolation systems provide an effective supplementary strategy to address this challenge. However, existing rolling-type floor isolators reported in the literature are predominantly limited to spherical or conical surface geometries. In this study, a novel rolling-type floor isolator incorporating a parabolic surface geometry is proposed, exploiting the inherent advantages of parabolic profiles in seismic response control. An analytical model of the proposed system was

first developed, and the corresponding equation of motion were derived and solved. Based on the analytical findings, two distinct prototypes were designed, fabricated, and tested. The experimental results demonstrate that the developed rolling-type parabolic-surface floor isolator (RPFI) is capable of reducing the accelerations transmitted to non-structural elements by up to 90%. These findings confirm that the proposed floor isolator significantly mitigates seismic demands on non-structural components.

Keywords: Floor Isolation, Seismic Isolation, Acceleration Reduction, Seismic Protection, Parabolic Surface Isolator

## ÖZ

### **YUVARLANMA ESASLI PARABOLİK YÜZEYLİ KAT İZOLATÖRÜ GELİŞTİRİLMESİ VE MEKANİK ÖZELLİKLERİNİN BELİRLENMESİ**

Aslan, Cem Eren  
Yüksek Lisans, İnşaat Mühendisliği  
Tez Yöneticisi: Prof. Dr. Uğurhan Akyüz

Ocak 2026, 132 sayfa

Deprem etkisi altında yapılarda, özellikle yapısal olmayan elemanlara etkileyen ivmelerin belirli sınır değerleri aşması, ciddi ekonomik kayıplara yol açabilmektedir. Veri merkezleri, müzeler, elektrik iletim sistemleri ve yüksek teknoloji tesisleri gibi yapılar, yapısal sisteme kıyasla daha pahalı ve hassas ekipmanlar içermeleri nedeniyle bu tür ivme taleplerine karşı oldukça duyarlıdır. Bu tür yapılarda, bina genelinde sismik izolasyon uygulanmış olsa dahi, kat seviyelerinde oluşan ivmelerin kabul edilebilir limitlerin üzerine çıkabildiği ve bunun sonucunda yapısal olmayan elemanların işlevini yitirebildiği bilinmektedir. Bu nedenle, söz konusu elemanlara iletilen ivmelerin azaltılması büyük önem taşımaktadır. Bu amaca yönelik olarak, kat izolatörleri etkili bir çözüm alternatifi sunmaktadır. Ancak mevcut uygulamalar ve literatür incelendiğinde, yuvarlanma esaslı kat izolatörlerinin çoğunlukla küresel veya konik yüzey geometrileri ile sınırlı kaldığı görülmektedir. Bu çalışmada, parabolik yüzey geometrisinin sunduğu avantajlar dikkate alınarak yuvarlanma esaslı parabolik yüzeyli bir kat izolatörü geliştirilmiştir. Öncelikle önerilen sistem için analitik bir model oluşturulmuş ve hareket denklemleri türetilmiştir. Elde edilen analitik çözüm sonuçları doğrultusunda iki farklı prototip tasarlanmış, üretilmiş ve test edilmiştir. Yapılan deneyler sonucunda, geliştirilen yuvarlanma esaslı parabolik yüzeyli kat izolatörünün, altına yerleştirilen yapısal olmayan elemanlara aktarılan

ivmeleri %90'a varan oranlarda azalttığı gözlemlenmiştir. Elde edilen bulgular, önerilen kat izolatörünün yapısal olmayan elemanlara etkileyen sismik talepleri önemli ölçüde düşürdüğünü ve deprem sırasında yüksek performans sergilediğini ortaya koymaktadır.

Anahtar Kelimeler: Kat İzolasyonu, Sismik İzolasyon, İvme Azaltımı, Parabolik Yüzeyle İzolatör

To my father...

## ACKNOWLEDGMENTS

The author wishes to express his deepest gratitude to his supervisor Prof. Dr. Uğurhan Akyüz for their guidance, advice, criticism, encouragements and insight throughout the research.

I would like to express my deepest gratitude to Prof. Dr. Haluk Sucuoğlu for his invaluable guidance and constant support throughout the duration of this research. His insightful advice and constructive criticisms played a pivotal role in refining the direction of this study.

I would like to extend my sincere gratitude to Dr. Kaan Kaatsız and Dr. Fırat Soner Alıcı for their support and for providing a professional environment that fostered my academic growth. I appreciate both of them for their leadership and for the opportunities provided under their supervision, which allowed me to balance my professional responsibilities with my research goals. Working alongside both has been an invaluable experience that has prepared me for my future career.

I would also like to express my appreciation to Dr. Cansu Yaşar and Dr. Sadun Tanışer for their collaboration and support during our shared project work. The opportunity to work alongside them was incredibly rewarding; their technical expertise and the collaborative environment they helped create significantly contributed to the practical insights integrated into this thesis.

I am also deeply grateful to Dr. Salim Azak for his exceptional technical support and assistance in the laboratory. His profound knowledge of experimental procedures and his willingness to share his expertise were vital to the successful execution of the tests conducted for this study. I truly appreciate his patience and the meticulous care he provided throughout the laboratory phase, ensuring a productive and safe working environment.

I would also like to extend my sincere appreciation to my colleagues, Onur Yardımcı, Erdem Çelik, Fatih Erikçi, and Ozan Karakoç, for their support. I am equally grateful to my future colleagues, Serhat Yardımcı, Canyoldaş Çaylı, Anıl Baran, Onur Divrik and Zerdeşt Taşdemir, whose support and camaraderie I look forward to as I continue my academic journey. Lastly, I would like to thank my dear friend Mazlum Meşe for his steadfast friendship and encouragement throughout the most demanding stages of this work.

Beyond the academic and professional support I received, this thesis would not have been possible without the unwavering love and encouragement of my family. I would like to express my deepest gratitude to my mother, Songül Aslan, whose endless support and belief in me have been my greatest source of strength throughout my life. I am also profoundly grateful to my brothers, Mehmet Aslan and İlhan Aslan, for their constant presence, motivation, and the unique bond we share. Their presence in my life has provided the emotional foundation necessary to complete this demanding journey, and I dedicate this achievement to them.

Finally, I wish to dedicate a special note of remembrance to my late father. Although he is no longer with us, his memory has been a guiding light throughout my master journey and my career as an engineer. The values of perseverance and integrity he instilled in me remain the cornerstone of my work. I carry his legacy with me in every challenge I overcome, and I hope this achievement would have made him proud.

## TABLE OF CONTENTS

ABSTRACT .....	v
ÖZ.....	vii
ACKNOWLEDGMENTS .....	x
TABLE OF CONTENTS .....	xii
LIST OF TABLES .....	xv
LIST OF FIGURES .....	xvii
CHAPTERS	
1 INTRODUCTION .....	1
1.1 Problem Statement.....	1
1.2 Floor Isolation Concept .....	3
1.3 Review of Past Studies on Floor Isolation Systems .....	6
1.3.1 Active and Hybrid Floor Isolators .....	6
1.3.2 Passive Floor Isolators.....	10
1.3.3 Discussion About Past Floor Isolation Studies .....	20
1.4 Objective and Scope .....	22
2 DEFINITION OF PARABOLIC GEOMETRY FOR FLOOR ISOLATORS AND METHODOLOGY .....	25
2.1 A New Geometry for Floor Isolators.....	25
2.2 Methodology.....	29
2.2.1 Analytical Study .....	30
2.2.2 Experimental Study .....	31
2.2.3 Discussion on Methodology .....	32

3	ANALYTICAL STUDY OF ROLLING-TYPE PARABOLIC-SURFACE FLOOR ISOLATOR (RPFI).....	33
3.1	Derivation of the Equation of Motion for Parabolic Surfaces .....	33
3.2	Solution of the Equation of Motion .....	37
3.3	Parametric Study for Damping Coefficient .....	45
3.4	Updated Analytical Study Results after Damping Calculation.....	47
3.5	Brief Summary of Analytical Study .....	53
4	EARTHQUAKE GROUND MOTIONS .....	55
5	INTRODUCTION OF TEST SETUP AND INSTRUMENTATION.....	65
5.1	Test Setup.....	65
5.1.1	Determination of Experimental Setup Requirements .....	65
5.1.2	Design of Test Setup .....	68
5.1.3	Design and Finite Element Analysis of Isolated Slab.....	69
5.2	Instrumentation and Data Calibration Process.....	72
5.3	Discussion about the Test Setup and Instrumentation .....	81
6	DYNAMIC TESTS AND RESULTS.....	83
6.1	Production of Prototypes.....	83
6.2	Introduction of Tests .....	85
6.3	Determination of Force-Deformation Relationship .....	86
6.4	Free Vibration Tests.....	93
6.4.1	Free Vibration Test Result for the First Prototype with Surface Equation $z=0.48x^2$ .....	93
6.4.2	Free Vibration Test Result for the Second Prototype with Surface Equation $z=0.192x^2$ .....	98
6.5	Harmonic Tests .....	100

6.5.1	Results of the Harmonic Tests for the First Prototype with Surface Equation $z=0.48x^2$ .....	100
6.5.2	Results of the Harmonic Tests for the Second Prototype with Surface Equation $z=0.192x^2$ .....	103
6.6	Strong Ground Motion Tests .....	105
6.6.1	Analysis of Strong Ground Motion Test Results for the Prototype with Surface Equation $z=0.48x^2$ .....	106
6.6.2	Analysis of Strong Ground Motion Test Results for the Prototype with Surface Equation $z=0.192x^2$ .....	112
6.7	Discussion about the Test Results .....	122
7	SUMMARY AND CONCLUSION .....	125
	REFERENCES .....	129

## LIST OF TABLES

### TABLES

Table 3.1 Comparison of the damping ratio obtained from the experiment and the damping ratio obtained by using Equation 3.14 .....	46
Table 4.1 General information about strong ground motions in GM Set-1 .....	60
Table 4.2 Seismic parameters of selected strong ground motions in GM Set-1 .....	60
Table 4.3 Characteristic properties of scaled strong ground motions in GM Set-1 .....	61
Table 4.4 General information about strong ground motions in GM Set-2 .....	62
Table 4.5 Seismic parameters of selected strong ground motions in GM Set-2 .....	63
Table 4.6 Characteristic properties of scaled strong ground motions in GM Set-2 .....	64
Table 5.1 Technical specifications of accelerometers used in the measurement system .....	75
Table 6.1 Information on harmonic loads used to determine force-deformation relationship.....	89
Table 6.2 Device parameters obtained from bilinear models derived using experimental data .....	91
Table 6.3 Friction coefficient calculated by using the free oscillation test results of the first prototype of RPF1 whose surface equation is $z=0.48x^2$ .....	95
Table 6.4 Damping ratio calculated by using the free vibration test results of the first prototype of RPF1 whose surface equation is $z=0.48x^2$ .....	97
Table 6.5 Harmonic test protocol used in the experiments of the first prototype with surface equation $z=0.48x^2$ .....	101
Table 6.6 Harmonic test protocol used in the experiments of the prototype with surface equation $z=0.192x^2$ .....	103
Table 6.7 Maximum displacement and rotation responses of isolated slab of the first prototype under GM Set-1 .....	108
Table 6.8 Acceleration Reduction Ratios from Experiments Conducted with GM Set-1 Acceleration Records for the First Prototype.....	111

Table 6.9 Maximum displacement and rotation responses of isolated slab of the second prototype under GM Set-1 .....	114
Table 6.10 Acceleration reduction rates from experiments conducted with GM Set-1 acceleration records for the second prototype .....	117
Table 6.11 Maximum displacement and deck rotation responses of the second prototype at isolated slab under GM Set-2 .....	119
Table 6.12 Acceleration amplifications at isolated slab from experiments conducted with GM Set-2 acceleration records for the second prototype .....	121

## LIST OF FIGURES

### FIGURES

Figure 1.1 An example of floor isolation.....	4
Figure 1.2 An example of an entire floor application presented in Nacamuli & Sinclair (2011) .....	5
Figure 1.3 Passive and active controlled hybrid platform proposed by Xu & Li (2006) .....	8
Figure 1.4 MR-damped semi-active floor isolation system proposed by Lin & Loh (2008).....	9
Figure 1.5 Frequency-dependent active floor isolator proposed by Shi et al. (2014) .....	10
Figure 1.6 Ball-in-Cone system proposed by Vargas & Bruneau (2006).....	12
Figure 1.7 The Roll-n-Cage (RNC) isolator proposed by Ismail et al. (2009) .....	14
Figure 1.8 Spring-based passive floor isolator proposed by Koumoussis & Moysidis (2019).....	16
Figure 1.9 Rail-based floor isolator system proposed by Zavala et al. (2020) .....	17
Figure 1.10 Floor isolator proposed by Walsh et al. (2024) .....	18
Figure 2.1 Comparison of different types of surfaces.....	26
Figure 2.2 Comparison of parabolic surfaces obtained with different $A$ values.....	28
Figure 2.3 Flowchart showing the methodology of the study. ....	29
Figure 3.1 Geometry of the proposed parabolic floor isolator.....	33
Figure 3.2 Parabolic isolator system a) free body diagram b) kinetic diagram .....	34
Figure 3.3 Acceleration reduction ratio results obtained after a parametric study conducted with 1% damping ratio .....	40
Figure 3.4 Displacement capacity utilization ratio results obtained after a parametric study conducted with 1% damping ratio.....	41
Figure 3.5 Two-dimensional CAD drawings of the first prototype of the RPFII ....	44
Figure 3.6 Effective damping ratio results calculated by using Equation 3.14 .....	47

Figure 3.7 Relationship between acceleration reduction ratio calculated with new damping ratios and device geometry .....	49
Figure 3.8 Relationship between displacement utilization ratio calculated with new damping ratios and device geometry .....	51
Figure 3.9 Two-dimensional CAD drawings of the second prototype of the RPF	52
Figure 4.1 Moderate level, 5% damped acceleration design spectrum according to Design Specification for Electrical Transmission Systems and Communication Facilities Under Earthquake Effects (2021) .....	56
Figure 4.2 Acceleration spectra of scaled seismic ground motion records and design acceleration spectrum for GM Set-1 .....	59
Figure 4.3 Acceleration spectra of scaled seismic ground motion records and design acceleration spectrum for GM Set-2 .....	62
Figure 5.1 Schematic representation of the elements that make up the experimental setup .....	67
Figure 5.2 CAD Model of the experimental setup consisting of support legs, shake table, modular platform, and the safety frame .....	67
Figure 5.3 Shaking table which installed in the laboratory .....	69
Figure 5.4 CAD drawings of modular platform (isolated slab) .....	70
Figure 5.5 The installed isolated slab in the laboratory .....	71
Figure 5.6 The position of the potentiometers used during the experiments .....	73
Figure 5.7 Test measurement system layout. ....	75
Figure 5.8 Mounting the accelerometers manufactured in the laboratory side by side to compare the measurements of branded accelerometers. ....	76
Figure 5.9 The accelerometer fixed directly on the hydraulic actuator connecting piece on the direction of excitation. ....	77
Figure 5.10 Potentiometers and accelerometers are placed on both corners of the isolated slab for acceleration data verification. ....	78
Figure 5.11 Raw acceleration data from one of the accelerometers under dynamic action. ....	79

Figure 5.12 Comparison of displacement data derived from calibrated and processed accelerometer data and raw displacement data from the potentiometer. ....	80
Figure 6.1 Technical drawings of the first prototype of the RPF1 .....	83
Figure 6.2 Image of the first prototype of the RPF1 .....	84
Figure 6.3 Technical drawings of the second prototype of a RPF1.....	84
Figure 6.4 Images of the second prototype of the RPF1 .....	85
Figure 6.5 Flowchart showing dynamic tests .....	85
Figure 6.6 The modified test setup for obtaining the force-deformation curves of floor isolators (the element that prevents horizontal movement and allows vertical movement is enclosed in a red circle). ....	87
Figure 6.7 Hysteresis results obtained from Test 7 for the floor isolator with a parabolic surface whose surface equation is $z=0.48x^2$ .....	90
Figure 6.8 Hysteresis results obtained from Test 7 for the floor isolator with a parabolic surface whose surface equation is $z=0.192x^2$ .....	91
Figure 6.9 Displacement-time plot of the isolated slab with a parabolic surface whose surface equation is $z=0.48x^2$ , obtained from free vibration experiments.....	94
Figure 6.10 Displacement-time plot of the isolated slab with a parabolic surface whose surface equation is $z=0.192x^2$ , obtained from free vibration experiments ..	98
Figure 6.11 Displacement demands during harmonic tests obtained on the isolated slab located above the floor isolator with surface equation $z=0.48x^2$ .....	102
Figure 6.12 Displacement demands during harmonic tests obtained on the isolated slab located above the floor isolator with surface equation $z=0.192x^2$ .....	104
Figure 6.13 Displacement responses of the first prototype under selected strong ground motions from GM Set-1 .....	107
Figure 6.14 Acceleration responses for the first prototype obtained under selected strong ground motions from GM Set-1 .....	110
Figure 6.15 Displacement and deck rotation responses of the second prototype under selected strong ground motions from GM Set-1 .....	113
Figure 6.16 Acceleration responses for the second prototype obtained under selected strong ground motions from GM Set-1 .....	116

Figure 6.17 Displacement and deck rotation responses of the second prototype under selected strong ground motions from GM Set-2 ..... 118

Figure 6.18 Acceleration responses for the second prototype obtained under selected strong ground motions from GM Set-2 ..... 120

# CHAPTER 1

## INTRODUCTION

### 1.1 Problem Statement

The primary goal in earthquake engineering is to minimize loss of life and property during earthquakes. Nonetheless, safeguarding valuable, costly, and delicate equipment within structures has emerged as a progressively significant problem. It is known that, especially in special structures like data centers, the total economic value of non-structural elements and building equipment can exceed the cost of load-bearing system in many cases. Therefore, even if structures remain standing after earthquakes, serious economic losses and functional disruptions can occur as a result of damage to the equipment inside them.

The overturning, displacement, or acceleration of non-structural elements exceeding permissible thresholds due to seismic events results in a total loss of functionality for these elements. Numerous studies in literature report serious damage to sensitive equipment such as servers, medical devices, and museum artifacts, particularly those exposed to high accelerations. A striking example of this situation is the damage to non-structural elements observed after the major earthquake that occurred in Chile on February 27, 2010, which was comprehensively compiled by Miranda et al. (2012). This study clearly demonstrated that the earthquake caused widespread and serious damage not only to the structural system but also to non-structural elements within the building.

During earthquakes, the inoperability of high-precision and high-cost devices located in structures such as data centers, museums, hospitals, and electrical transmission infrastructure causes not only direct economic losses but also disruptions to critical services. For example, damage to medical devices in hospitals

can limit emergency response capacity or failures in data centers can lead to significant data loss and extended service interruptions. In this context, the protection of non-structural elements should be considered an integral part of building safety.

Seismic isolation systems applied at the building scale to reduce this type of damage can offer a partial solution by reducing the seismic effects transmitted to the superstructure to a certain extent. However, even in base-isolated structures, floor accelerations can exceed the tolerance limits of sensitive equipment in some cases. Furthermore, base isolation applications require high costs in terms of design, implementation, and maintenance, making them not always a viable option, especially for the retrofitting of existing structures.

Therefore, it is necessary to develop alternative and complementary approaches that focus directly on the equipment to be protected. At this point, the concept of floor isolation comes to the fore. Floor isolation aims to reduce the acceleration, and displacement demands to which sensitive and expensive equipment is exposed by means of isolators placed underneath this equipment. This approach offers a more flexible and economical way compared to isolation systems applied at the building scale.

The use of floor isolators offers a significant advantage in both the new and existing buildings, as they can be implemented without requiring major intervention in the structural system. Furthermore, floor isolation applications stand out as a cost-effective solution because they focus solely on the equipment that needs protection, independent of the building's overall behavior. With these characteristics, floor isolation is considered an important solution for reducing non-structural element damage and associated economic losses during earthquakes and is increasingly recognized as a significant engineering approach. General information regarding floor isolation is provided in Chapter 1.2.

## 1.2 Floor Isolation Concept

Non-structural elements within the structure, which often have much higher economic and functional value than the structure itself, retain their functionality after an earthquake. Electrical transmission and distribution systems, data centers, hospitals, museums, industrial facilities, and high-tech infrastructure are prominent examples of such structures. The equipment used in such structures, such as circuit breakers, current and voltage transformers, GIS units, server racks, medical devices, or precision production machines, often have low displacement capacities and limited acceleration resistance. Therefore, even if the load-bearing system is unharmed, the acceleration demands these components are subjected to during an earthquake can result in significant functional and economic losses.

Even in base-isolated structures, the accelerations at floor levels can exceed acceptable limits for sensitive non-structural elements, particularly due to high mode effects and the dynamic behavior of rigid equipment. Especially on upper floors or in heavy equipment embedded in rigid floors, the acceleration reduction provided by foundation isolation may not be sufficient. This situation can cause critical equipment to fail and the device to lose its function, even if the load-bearing system remains intact after an earthquake.

Floor isolators, developed as a solution to this problem, aim to directly reduce the acceleration demands transmitted to non-structural elements by creating an additional seismic isolation layer at the level where these elements are located.

Floor isolators can be thought of as similar to the classic isolators used in foundations; however, the system being isolated here is not the entire structure, but only a specific floor or the equipment group on that floor. This approach offers a much more economical and targeted solution than isolating the entire building, especially in structures with only a limited number of critical pieces of equipment. Thus, isolation focuses on the elements that really need to be protected, preventing unnecessary structural interventions. Nacamuli & Sinclair (2011) presented an

example system of a floor isolator application in his research, as shown in Figure 1.1.

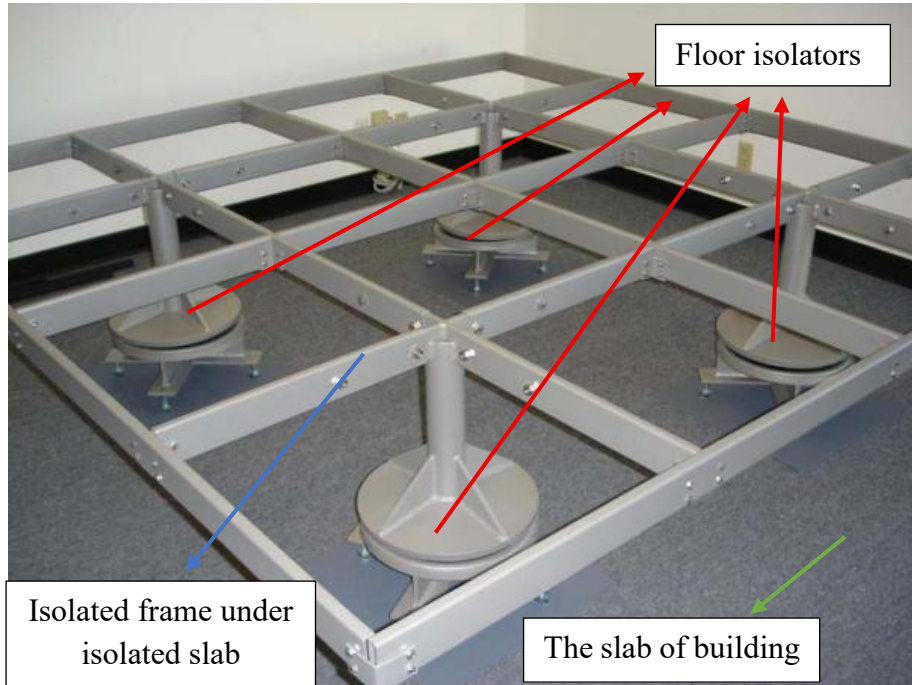


Figure 1.1 An example of floor isolation

One of the most important advantages of floor isolators is that they can be applied regardless of the level at which the element to be protected in the structure. The non-structural component may be located at ground level, on intermediate floors, or on the top floor. Heavy and sensitive equipment located on upper floors is at greater seismic risk because floor accelerations generally increase as the height of the structure increases. The floor isolator approach eliminates this disadvantage by creating a local isolation plane at the point where the equipment is located. Thus, lower acceleration requirements are achieved for the relevant element, independent of the general dynamic behavior of the structure.

In terms of application, floor isolators can be designed in two basic ways. In the first approach, only a specific device or group of devices is individually isolated. In this case, the isolators are placed directly under the relevant equipment, and the equipment is dynamically separated from the building's floor. This method is highly

suitable for localized elements such as a single server cabinet, electrical cabinet, or valuable items in museums. In the second approach, an entire floor or a specific area is isolated. In this method, all equipment and non-structural elements on that floor are isolated together, creating a "floating platform." This is a preferred solution, particularly for data centers, control rooms, or areas where multiple sensitive pieces of equipment are located together. Nacamuli & Sinclair (2011) presented an example of an entire floor isolator application in his research, as shown in Figure 1.2.

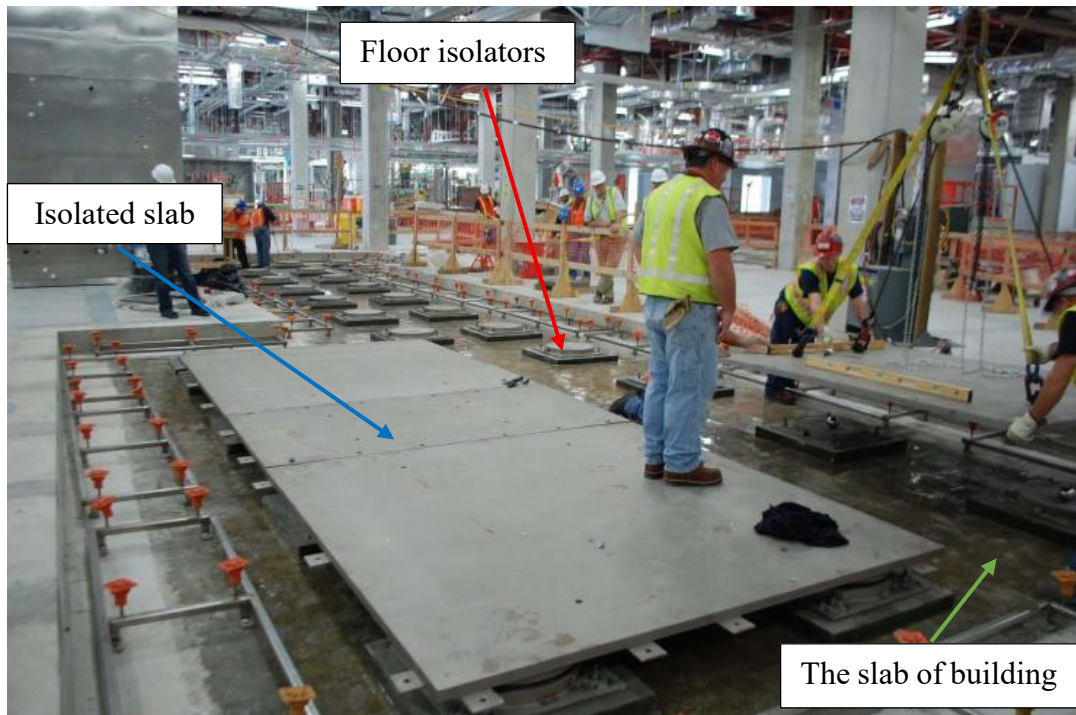


Figure 1.2 An example of an entire floor application presented in Nacamuli & Sinclair (2011)

The application procedure for this kind of floor isolation application adheres to a specific order. First, the existing structure's floor is raised by a certain amount, and an intermediate void is created. This void provides the volume for the floor isolators to be installed. The isolators are connected to the main structural system of the building at this level, and a new secondary platform or floor is constructed on top. This new platform is the structural element on which the isolated equipment sits and which moves relative to the isolators during an earthquake.

During an earthquake, while the main structure moves, the accelerations of the isolated platform are significantly reduced thanks to the isolators. The low horizontal stiffness of the isolators extends the effective period of the system, reducing acceleration demands, while the provided damping mechanism ensures that relative displacements are kept under control. Thus, both the accelerations affecting the equipment are reduced and excessive displacement of the isolators is prevented.

Consequently, floor isolators represent an advanced design approach in modern earthquake engineering that aims not only to ensure the safety of the structural system but also to maintain functional continuity and minimize economic losses. Floor isolators enable the targeted isolation of only the necessary areas, without requiring the isolation of the entire structure, particularly for the protection of critical infrastructure and high-value equipment.

### **1.3 Review of Past Studies on Floor Isolation Systems**

Various types of floor isolators have been suggested in academic studies on floor isolation. These scholarly investigations encompass both analytical and experimental research. Certain studies have been exclusively proposed analytically and advance purely by numerical modeling. Moreover, floor isolators have been examined through both analytical and experimental methods. The investigations of floor isolators can be categorized into two separate types: active floor isolators and passive floor isolators.

#### **1.3.1 Active and Hybrid Floor Isolators**

Active floor isolators are systems that use sensors, control algorithms, and actuators to reduce the accelerations caused by earthquakes or vibrations affecting the floors within a structure. These systems monitor the structure's response in real time, generate counterforces, and thus keep the accelerations affecting the equipment

under control. Unlike passive isolators, they could adapt to changing load and movement conditions.

Equipment used in ultra-precise manufacturing processes such as semiconductor production and optical devices can be affected even by low-level environmental vibrations; if this type of structure located in seismic zones, they are at serious risk. As a solution to these challenges, Xu & Li (2006) propose a dual-layer, passive and active controlled hybrid platform that can reduce both micro-vibrations and seismic effects (Figure 1.3). This hybrid platform system has been designed to reduce the sensitivity of high-tech equipment to micro-vibrations and prevent damage during earthquakes. In the proposed system, passive isolation reduces the acceleration response during an earthquake, while active control mitigates velocity-induced vibrations during standard operation circumstances. Within the scope of the study, an analytical model supported by magnetostrictive actuators and the LQG (Linear Quadratic Gaussian) control algorithm was developed, and numerical simulations were performed on a high-tech facility using this model. In another study for a similar system, Xu et al. (2008) presents an experimental evaluation of a two-layer hybrid platform developed to protect high-tech equipment from both micro-vibrations and seismic effects. The hybrid platform aims to reduce acceleration response during earthquakes with its passive layer and suppress velocity-based micro-vibrations under normal operating conditions with its active layer. The platform was placed on a three-story building model and tested under both traffic-induced ground motion and earthquake records (El Centro, Northridge, and Hachinohe) applied using a shaking table. Piezoelectric actuators and a velocity feedback control algorithm were used for active control; dampers with adjustable stiffness and damping characteristics and a leaf spring system were integrated for passive behavior. Up to 80% acceleration reduction was achieved against the earthquake records. Under micro-vibration conditions, the active layer provided a significant 80% reduction in velocity response. It was also determined that the platform offers effective protection against instantaneous impact-type disturbances.

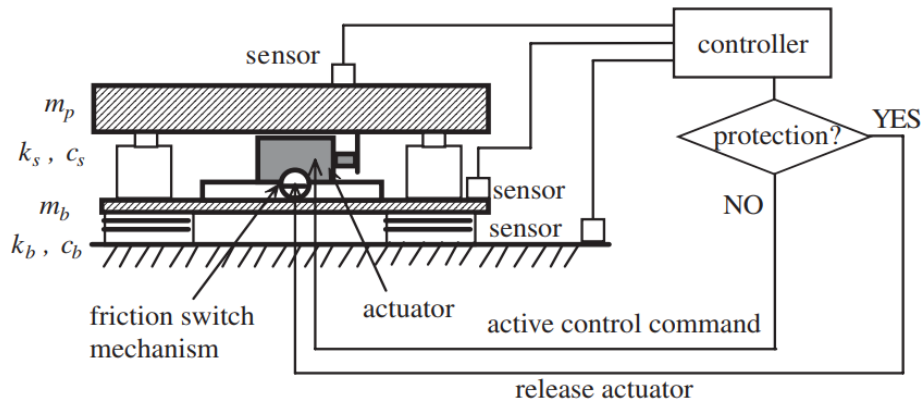


Figure 1.3 Passive and active controlled hybrid platform proposed by Xu & Li (2006)

The semi-active isolation systems proposed by Gavin & Zaicenco (2007) can optimize system response in real time thanks to their variable damping or stiffness characteristics and can demonstrate superior performance, particularly in terms of acceleration reduction. Gavin & Zaicenco (2007) address an aspect often neglected in the literature by considering not only the performance of semi-active equipment isolation but also controller reliability and failure probabilities. The findings show that when supported by appropriate control strategies, semi-active systems can provide more flexible and higher-performance seismic protection for sensitive systems such as hospital and data center equipment compared to passive isolation solutions.

The MR-damped semi-active floor isolation system developed by Lin & Loh (2008) offers a significant contribution by combining the reliability of passive isolation with the adaptability of active control (Figure 1.4). The rolling pendulum system provides a low-friction recall mechanism, while controlling the MR damper with continuously-optimal LQR or fuzzy logic algorithms enables the system to effectively adapt to different PGA levels. Results validated by shaking table tests demonstrate that semi-active floor isolation can reduce not only isolated floor accelerations but also the structure's global seismic response. In this respect, the study offers an experimentally validated, adaptable, and fail-safe solution in the

literature on semi-active equipment and floor isolation, indicating higher performance potential compared to passive and fixed-gain control approaches.

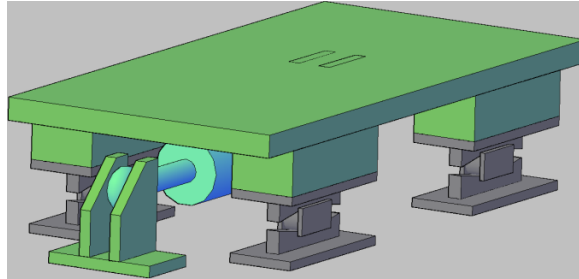


Figure 1.4 MR-damped semi-active floor isolation system proposed by Lin & Loh (2008)

The literature on active and semi-active control-based seismic isolation systems has primarily focused on fixed-gain optimal control methods (LQR) and rule-based semi-active algorithms. Fixed-gain LQR controllers are widely used due to their mathematical simplicity and stability properties; however, they cannot meet the varying demands of system dynamics across different frequency bands with the same effectiveness. This situation becomes particularly apparent under excitations with broadband and time-dependent frequency content, such as earthquakes. Shi et al. (2014) made a significant contribution to literature by extending the LQR control framework with frequency-dependent gain scheduling to overcome this limitation (Figure 1.5). Adapting control gains according to the instantaneous frequency content allows for more aggressive control forces in resonance regions and more limited control forces at higher frequencies. This approach can be considered a more flexible and performance-oriented solution compared to passive and fixed-gain active control strategies in studies on semi-active equipment isolation and the protection of sensitive systems.

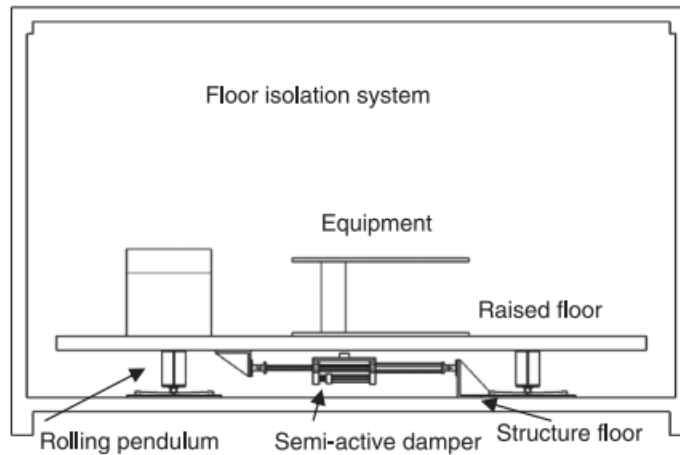


Figure 1.5 Frequency-dependent active floor isolator proposed by Shi et al. (2014)

As a result of a comprehensive literature review on seismic isolation technologies, a study inventory focusing on active and semi-active floor isolator systems has been compiled. Upon examining these studies, it is observed that various mechanical systems integrated with control algorithms such as linear quadratic regulators (LQR) and fuzzy logic have been developed. The main purpose of these studies is to minimize the acceleration, and displacement demands affecting the superstructure by providing instantaneous responses to changing earthquake characteristics and to optimize structural safety.

### 1.3.2 Passive Floor Isolators

In the literature, passive floor isolators, as well as active floor isolation techniques, constitute an important area of research and application. Unlike active systems, which require complex sensor networks, data processing algorithms, and uninterruptible external power sources, passive isolators operate entirely based on the system's internal mechanical properties and geometry. These systems automatically trigger when the ground acceleration affecting the structure during a seismic event exceeds a certain threshold value. Their primary function is to dampen down the seismic energy transmitted to the structure by decoupling the dynamic interaction between the superstructure and substructure, thereby keeping the

displacement and acceleration demands on the superstructure elements within safe limits.

Upon reviewing the existing literature and application examples, passive floor isolation systems can be categorized under three main groups based on their operating principles and geometries. The first group in this classification consists of rolling-based isolators that reduce acceleration through the movement of a ball or rolling element between two surfaces. The second category includes hybrid systems equipped with rails or springs that limit the movement of the structure to a specific trajectory and provide a restoring force. Finally, the third group consists of systems designed as alternatives to traditional floor isolator approaches. These systems contribute to floor isolator studies by using a different floor isolator model or different materials.

#### **1.3.2.1 Rolling-type Floor Isolator**

Floor isolation systems have gained increasing attention in the literature in recent years, particularly for reducing high floor accelerations on non-structural elements and sensitive equipment. In this context, Ball-in-Cone (BIC) type floor isolators offer an innovative solution that, unlike classic base isolation, aims to limit acceleration demands only at specific floors or deck levels without significantly altering the global behavior of the structure. In the experimental study by Vargas & Bruneau (2006), the BIC system was considered in conjunction with the structural fuse concept and used to control increased floor accelerations in a steel frame (Figure 1.6). The basic operating principle of the Ball-in-Cone system is based on the production of a gravity-based restoring force through the rolling of a spherical ball on a conical surface. This mechanism provides low-stiffness horizontal behavior in situations where friction is limited, significantly reducing the accelerations transmitted to the floor by extending the effective period of the system. Similar to pendulum-type or spherical-surface isolators in the base isolation literature, this approach offers a more compact, locally applicable, and floor-system-integrated

solution thanks to the Ball-in-Cone geometry. Experimental findings obtained in the study by Vargas & Bruneau (2006) show that the BIC system provides significant reductions, particularly in upper floor accelerations, and effectively limits acceleration demands that are critical for non-structural components. Furthermore, the passive nature of the BIC system eliminates the energy requirements, control complexity, and reliability issues encountered in semi-active or active systems. Vargas & Bruneau (2006) have demonstrated that such passive floor isolators can make a critical contribution, particularly in the protection of non-structural elements.

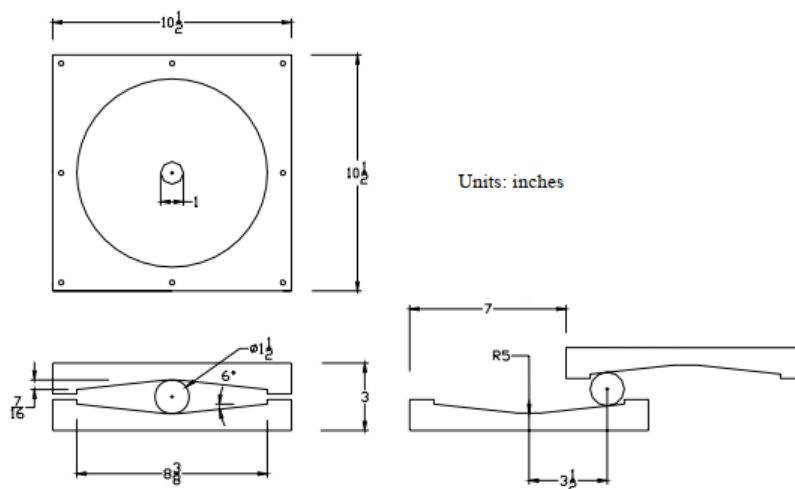


Figure 1.6 Ball-in-Cone system proposed by Vargas & Bruneau (2006)

Cui & Bruneau (2008) investigated the experimental performance of isolated floor systems to reduce the accelerations experienced by non-structural elements in critical structures during earthquakes. The study evaluated two different solutions, which is a system based on multi-directional springs and a concrete ball-in-cone type floor isolator, by using six-degree-of-freedom shake table tests. The experimental results showed that both systems significantly reduced floor accelerations and could safely carry the design vertical loads. In particular, for the ball-in-cone system, it was found that rolling friction was decisive for the hysteretic behavior and that peak accelerations could be kept nearly constant over certain displacement ranges. In a similar study, Cui (2012) evaluated two different isolated floor systems developed using concrete ball-in-cone (BIC) isolators and multi-directional spring units through

full-scale shaking table tests, and their acceleration–displacement behavior was examined in detail. Experimental results revealed that BIC isolators effectively limit floor accelerations through nonlinear rolling and friction mechanisms and change the system frequency depending on displacement. This study systematically establishes not only the performance of ball-in-cone-based floor isolators but also their design and modeling principles, serving as a fundamental reference in the literature.

Chung et al. (2009) demonstrated that while linear isolators carry the risk of resonance and excessive displacement, particularly in near-fault earthquakes, nonlinear rolling isolation systems can naturally limit this problem. In the study, the equation of motion for a rolling isolator with an eccentric connection were derived analytically, revealing that the system's frequency changes depending on displacement. Numerical analyses showed that even if the isolator's linear equivalent frequency coincides with the dominant earthquake frequency range, resonance does not occur and acceleration amplification remains limited due to nonlinear behavior.

Ismail et al. (2009) proposed the Roll-n-Cage (RNC) isolator, designed to protect high-precision equipment from seismic and micro-vibration effects (Figure 1.7). This system, which has a rolling-based mechanism, incorporates features such as energy dissipation through metallic dampers, return to the initial position through a gravity centering mechanism, and excessive displacement control through shock-absorbing buffers. The authors modeled the mechanical behavior of the system using the finite element method in ANSYS and performed comprehensive dynamic analyses in SAP2000 using Bouc-Wen hysteretic parameters. Tests conducted under 36 different earthquake records and harmonic ground motions claimed that the RNC isolator reduced equipment accelerations by 98% and kept displacements within operational limits.

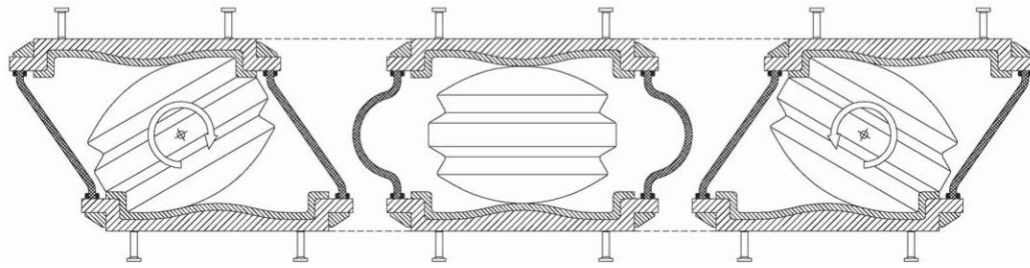


Figure 1.7 The Roll-n-Cage (RNC) isolator proposed by Ismail et al. (2009)

Nacamuli & Sinclair (2011) explained the nonlinear force-displacement behavior of the Ball-N-Cone isolator, which consists of steel balls and conical-surfaced cups, and emphasized that accelerations on the isolator plane can be limited to approximately 0.1–0.15g levels thanks to the low surface slope. Examples from applications show that the isolators have been successfully used in data centers, raised floors, and precision equipment platforms, reducing acceleration demands compared to traditional anchoring and rigid fastening methods.

When reviewing the literature on ball-in-cone-type rolling-based floor isolators, it is generally observed that single-axis or linear models are used. To demonstrate the inadequacy of this approach, Harvey & Gavin (2013) examined the dynamic behavior of rolling isolation systems in detail under multi-axis motion, large rotations, and slip-free rolling conditions, revealing that such systems have a nonholonomic and chaotic structure. In the study, the equation of motion for a four-ball, double-curve rolling surface were derived using the Lagrange approach. It was shown that the potential energy is strongly dependent on the surface geometry and that the horizontal and rotational motions are nonlinearly coupled. Experimental free vibration measurements and numerical simulations confirmed that small differences in initial conditions lead to completely different trajectories and that the system has a positive Lyapunov exponent. It was also emphasized that the parabolic surface assumption is insufficient to capture this complex behavior, while realistic surface geometries clearly reveal the chaotic response. Similarly, a simplified multi-axis model that preserves nonlinear and nonholonomic behavior for rolling-based isolation systems was proposed by Harvey et al. (2014) and validated with shake

table experiments. The study showed that in systems with parabolic-conical surface geometry, rolling damping enhanced by viscoelastic coatings significantly reduced displacement demands and improved performance without increasing peak accelerations. Furthermore, it was found that peak displacement and acceleration values can be reliably predicted despite the chaotic character. These findings demonstrate that practical and reliable modeling approaches are possible for rolling isolation systems.

Bin & Harvey (2022) proposed a dual-mode floor isolation system in which floor isolators can perform both isolation and energy absorption functions in low-intensity earthquakes and high-intensity earthquakes, respectively. Experimental and numerical results show that the isolator effectively reduces floor accelerations before the impact. After the impact, it can limit the floor displacement demands of the main structure through nonlinear interaction. The study demonstrates that floor isolators can contribute not only to content protection but also to reducing structural response under certain conditions.

Another study conducted on rolling-based floor isolators involves increasing surface friction by applying different coatings to the rolling surface. Vargas et al. (2022) experimentally investigated the behavior of rolling-type floor isolation systems, considering different surface coatings, and validated it using the real-time hybrid simulation (RTHS) method. The study showed that elastomeric surface coatings reduce displacement demands by increasing rolling resistance and damping, while having a limited effect on peak accelerations. The results reveal that surface properties are a decisive design parameter in the performance of floor isolation systems.

Literature reviews have shown that rolling-based floor isolators demonstrate high levels of effectiveness in seismic isolation applications. These types of isolators stand out due to both their practical applicability and their superior performance in reducing the accelerations transmitted to the superstructure. Current studies reveal

that rolling-based systems offer an effective solution for protecting non-structural elements and provide a reliable alternative for controlling floor accelerations.

### 1.3.2.2 Floor Isolators with Rail and Spring

In addition to rolling-type floor isolators, which are frequently referenced in the literature on passive floor isolation technologies, systems consisting of rails or springs stand out as the second main design group. These systems provide a different kinematic approach to the seismic isolation mechanism by ensuring that structural movement occurs along a predetermined linear trajectory. One such spring-based system, a lightweight and compact floor isolator suitable for use in sensitive areas like museums, was proposed by Koumousis & Moysidis (2019) (Figure 1.8). The effectiveness of this isolator, consisting of a low-stiffness core and high-deformation-capacity outer components, has been tested through experimental studies and time-domain analyses. The findings reveal that the proposed system reduces the accelerations transmitted to the superstructure by 40-80%.

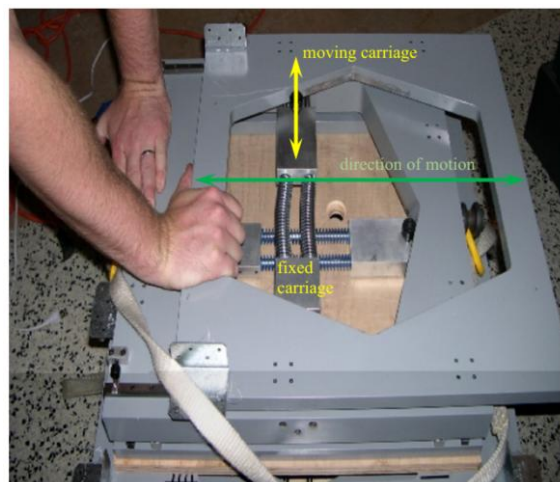


Figure 1.8 Spring-based passive floor isolator proposed by Koumousis & Moysidis (2019)

A rail-based floor isolator system for use in museums has been proposed by Zavala et al. (2020) (Figure 1.9). This developed isolator consists of cross-directional linear bearings with a low friction coefficient and springs that provide restoring force. The system prevents the object from tipping over by achieving long natural vibration periods even under low gravitational loads for lightweight objects, while also significantly reducing the acceleration response. In the study, the dynamic behavior of the system was analyzed using mathematical models and shake table tests were performed on a prototype.

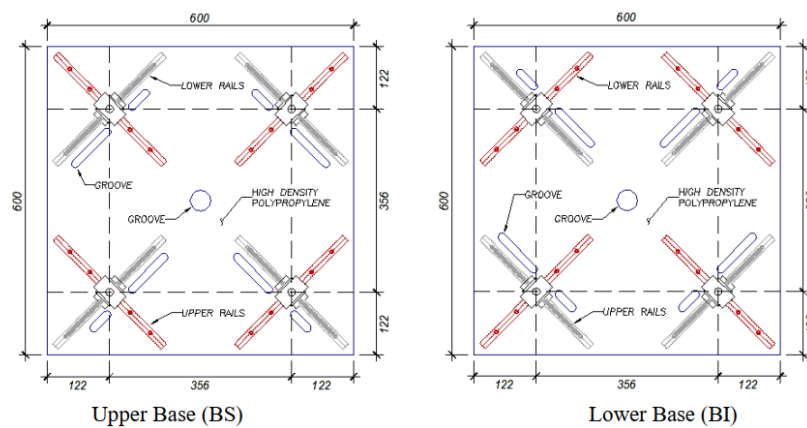


Figure 1.9 Rail-based floor isolator system proposed by Zavala et al. (2020)

Another type of floor isolator that uses both rails and springs was proposed by Walsh et al. (2024) (Figure 1.10). They designed devices based on the Adaptive Returning Force (ARF) principle to reduce the acceleration and stresses transmitted to equipment. This system, which offers displacement-dependent stiffness and exhibits a three-stage nonlinear behavior, consists of rails that operate independently on both horizontal axes. Numerical analysis findings have shown that the proposed system does not transfer high-frequency movements to the superstructure. This feature demonstrates the system's success in reducing the demands on the elements above it during an earthquake, functioning like a low-pass filter.

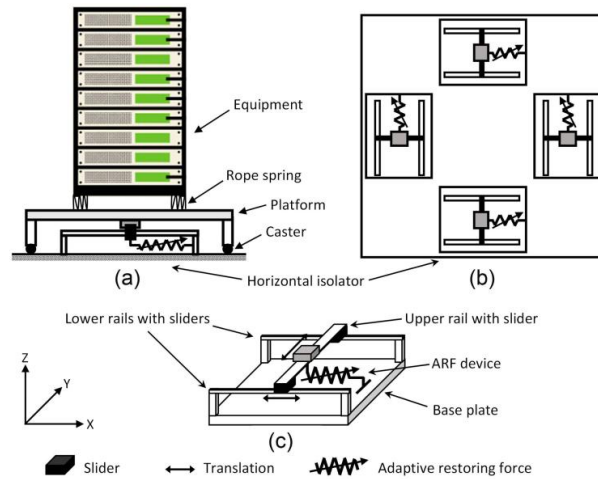


Figure 1.10 Floor isolator proposed by Walsh et al. (2024)

Based on these studies, it is seen that rail and spring-based floor isolators offer an effective alternative, especially for lightweight and sensitive structures. Thanks to their linear kinematics, low friction, and adaptable stiffness properties, these systems significantly reduce the accelerations transmitted to the superstructure, thereby improving seismic performance.

### 1.3.2.3 Alternative Passive Floor Isolators

In addition to the types of floor isolators commonly studied in the literature, there are also alternative floor isolator studies that adopt different approaches from these systems. These studies aim to provide alternatives to existing floor isolator solutions and offer innovative approaches to improve system performance. The floor isolators developed in this context incorporate various material types and unique floor isolator design concepts, differing from traditional applications, and present new design possibilities in the field of seismic isolation.

The literature on reducing the transmission of machine-induced vibrations to building floors has primarily focused on classical passive isolation systems (springs, rails and rolling-type) and active and semi-active control approaches. While passive systems offer simplicity and reliability, they may exhibit limited performance under

low-frequency excitation due to resonance issues. Active and semi-active systems, on the other hand, provide adaptability but are not suitable for every application due to energy requirements, control complexity, and reliability issues. The lever-type inertia compensator isolation system proposed by Ivovich & Savovich (2001) offers an innovative compromise between these two approaches. By using an auxiliary mass and lever mechanism to create controlled anti-resonance in the system, it enables a significant reduction in transmitted vibrations, particularly under low-frequency harmonic excitation.

Ceiling-mounted suspended floor isolators are also described in the literature unlike systems traditionally installed at ground level. In this context, Mahmoud & Chulahwat (2015) proposed a floor isolator based on the hybrid use of suspended and sliding mechanisms. For this system, which operates on the principle of a multi-tuned mass damper (MTMD), the authors present a comprehensive analytical model focused on the optimization of vertical and horizontal floor distributions.

Earthquakes, particularly those occurring in Latin America, have caused devastating damage to both structural and non-structural components of critical buildings such as hospitals. As a solution to this problem, Morales et al. (2018) proposed a new ground isolation system (RTB - Recycled Tire Bearing) developed using recycled car tires as a low-cost, sustainable, and locally sourced solution. The RTB system provides isolation against both horizontal and vertical ground accelerations thanks to the special geometric arrangement of the tires.

An analysis of alternative systems for floor isolation reveals the emergence of novel models that prioritize economic efficiency and deviate from conventional design paradigms. Although such systems are not widely used in literature or in practice, innovative and original approaches are being presented in the context of floor isolator research. These studies offer different perspectives in the field of seismic isolation, providing alternative solutions to traditional isolator designs.

### 1.3.3 Discussion About Past Floor Isolation Studies

In the literature, floor isolators can be categorized into two main groups: active or semi-active and passive systems. Active floor isolators measure the instantaneous response of the structure or platform using sensors, control algorithms, and actuators, and generate opposing forces. The main advantage of these systems is their ability to adapt to different earthquake characteristics and frequency contents and to perform well even at low vibration amplitudes. As seen in the systems proposed by Xu & Li (2006), Lin & Loh (2008), and Shi et al. (2014), active or semi-active control effectively reduces both micro-vibrations and earthquake effects. However, this high performance also brings significant engineering and operational risks, such as complex hardware, continuous energy requirements, dependence on control algorithms, and system reliability.

In contrast, passive floor isolators reduce seismic effects solely through their geometry and mechanical properties, without requiring any external energy or active control mechanisms. These systems create a natural decrease in stiffness and an increase in period by utilizing the relative movement generated during an earthquake, thereby limiting acceleration demands. In the literature, passive floor isolators are grouped into three main categories: rolling-based systems, rail-and-spring-based systems, and alternative designs. Rolling-based systems, such as Ball-in-Cone, can significantly reduce floor accelerations thanks to gravity-based recall mechanisms and low effective stiffness. Rail-and-spring-based systems, on the other hand, offer a linear path of motion and adjustable stiffness, making them particularly effective in protecting light and delicate equipment.

When comparing active and passive floor isolators, active systems theoretically have a high-performance potential because they can reduce not only seismic effects but also micro-vibrations affecting non-structural components. However, despite these advantages, high initial investment costs, continuous maintenance requirements, dependence on external power sources, and the risk of control system failures create significant limitations for these types of systems. Particularly during sudden and

violent events such as earthquakes, the inability to guarantee that active systems will operate continuously and reliably poses a serious reliability issue. In contrast, passive floor isolators exhibit more predictable behavior due to their simpler, mechanically based components and offer long-term operational safety with low maintenance requirements. For these reasons, passive floor isolators stand out as a more practical, reliable, and sustainable solution for critical infrastructure and facilities that require continuous operation.

This balance point is also the main reason for choosing a rolling-based passive floor isolator in this study. Rolling-based systems reduce floor-level accelerations thanks to their low effective stiffness and reduce the risk of permanent displacement through gravity-based recall mechanisms. The literature shows that rolling-type passive systems reduce the accelerations affecting non-structural elements, especially under seismic effects, and are thus successful in protecting non-structural elements. Furthermore, unlike active systems, these systems operate without requiring external energy, offering a clear advantage in terms of reliability during earthquakes.

In the literature, it is observed that the vast majority of rolling-based plate isolators have been developed based on spherical or conical surface geometries. While these geometries are preferred due to manufacturing ease and analytically definable constant slope characteristics, they do not allow the system's stiffness and recall characteristics to vary throughout displacement. In contrast, parabolic surface geometry provides variable slope and thus variable effective stiffness to the rolling mechanism, allowing the system to exhibit more flexible behavior at small displacements and more restrictive behavior at large displacements. This situation indicates that the potential advantages offered by parabolic surfaces have not yet been sufficiently investigated and that they may offer a more effective solution, particularly in terms of improving the balance between acceleration reduction and displacement control.

In this context, the rolling-based parabolic-surface floor isolator (RPFI) developed within the scope of this thesis combines the reliability of passive systems with the

high acceleration reduction potential of rolling-based mechanisms, positioning itself as a balanced, applicable, and high-performance solution in the field of floor isolation.

#### **1.4 Objective and Scope**

The primary objective of this study is to develop an innovative floor isolator based on parabolic surface geometry with a rolling principle. The study aims to determine in detail the mechanical properties of the proposed rolling-type parabolic-surface floor isolator (RPFI). It is intended that the findings obtained in this regard will offer a unique design approach to floor isolator research and provide an alternative solution to existing seismic isolation systems.

The scope of this study primarily involves deriving the equation of motion for the floor isolator by adopting an analytical approach for the RPFI system. To this end, the dynamic behavior of a ball moving on a parabolic surface was examined, and the system's equation of motion was obtained analytically. The derived equation of motion was solved by using earthquake ground motion records selected in accordance with the seismic hazard determined in the study, and numerical solutions representing the dynamic response of the isolator were obtained. As a result of these analyses, two different RPFI prototypes were determined and manufactured to meet the expected performance criteria of the RPFI system. Through experimental studies conducted on the manufactured prototypes, the mechanical properties and dynamic behavior of the RPFI were determined, and the results obtained from analytical and numerical studies were verified with experimental data. Thanks to this comprehensive approach, the performance of the proposed RPFI was evaluated within a holistic framework.

The outline of this study can be given below:

- Chapter 2 explains why a parabolic surface floor isolator was studied and outlines the advantages of the parabolic surface. Additionally, the methodology of this study is discussed in this chapter.
- In Chapter 3, the equation of motion for the parabolic surface is obtained and solved by using the strong ground motion sets selected in Chapter 4.
- Chapter 4 discusses the selection of strong ground motion sets used during analytical study and experimental work.
- Chapter 5 examines the experimental setup and measurement devices.
- Chapter 6 focuses on experimental results.
- Chapter 7 provides a general summary.



## CHAPTER 2

### DEFINITION OF PARABOLIC GEOMETRY FOR FLOOR ISOLATORS AND METHODOLOGY

#### 2.1 A New Geometry for Floor Isolators

A detailed review of the academic literature on floor isolators is presented in Chapter 1.3, where numerous experimental and theoretical studies conducted by various researchers are examined and compared to provide a clear understanding of different types of floor isolation systems. Floor isolators with different materials, structural types, and geometric properties are evaluated in terms of their performance, areas of application, and behavioral characteristics. The findings from the reviewed studies offer a broad perspective on the existing floor isolator technologies, highlighting the main advantages and limitations of each type while summarizing key examples from the literature.

In literature review, it was observed that the surface geometries of rolling-type floor isolators are generally designed as either conical or spherical. This observation formed an important foundation for understanding how the geometry of an isolator influences the system's energy dissipation capacity and acceleration reduction performance. The findings from the analyzed studies clearly demonstrated that surface geometry has a significant impact on the overall performance of the isolator. In particular, the shape of the surface curve directly affects the stiffness variation, energy dissipation capability, and acceleration reduction efficiency of the system.

Based on these findings discussed in Chapter 1.3.3, this study aims to develop a rolling-type floor isolator with a new surface profile that serves as an alternative to conventional conical and spherical geometries. The comparison of the existing surfaces and the proposed parabolic surfaces is presented in Figure 2.1. The primary objective is to investigate how changes in surface geometry influence the overall

performance of the device and to design an isolator capable of achieving improved results. In this context, a new isolator model is proposed in which the surface geometry is defined by a parabolic equation represented by the parabolic function  $z = Ax^2$ , which forms the basis for examining the relationship between geometric configuration and mechanical performance.

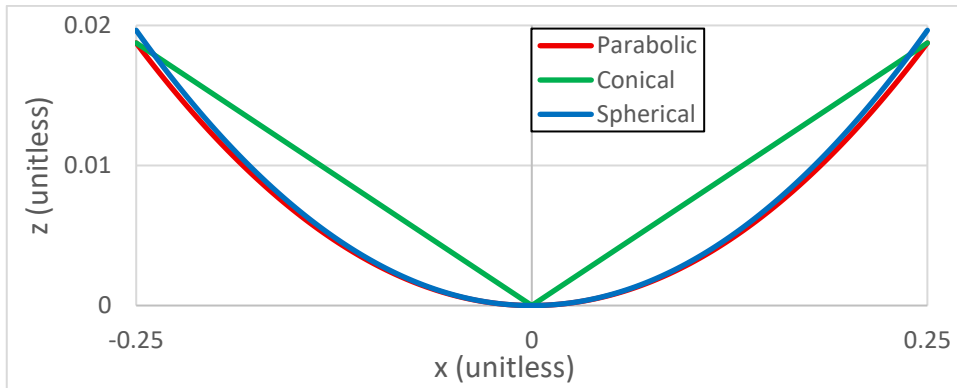


Figure 2.1 Comparison of different types of surfaces.

Rolling-type parabolic surface isolators offer several structural and dynamic advantages over conical and spherical surface isolators due to their unique geometric configuration. The most significant distinction is that the surface slope changes with the displacement of the rolling element. This characteristic introduces an inherent nonlinear behavior, resulting in variable stiffness where the isolator's restoring force increases as displacement grows. Consequently, at small displacements, the system exhibits greater flexibility, effectively reducing the accelerations transmitted to the structure. At larger displacements, however, the increased stiffness limits excessive movement, preventing the isolator from exceeding its displacement capacity. This adaptive response provides an optimal balance between acceleration reduction and structural safety, ensuring both improved performance and reliability under varying loading conditions.

In addition, the parabolic surface geometry generates a variable potential energy profile throughout the motion of the rolling element. This variation enables the system to dissipate energy more uniformly, leading to more stable energy dissipation and enhanced re-centering capability. In contrast, spherical surface isolators exhibit

constant curvature, which limits this balance and restricts the system's ability to adapt to varying displacement levels. Parabolic geometry, however, provides a more gradual and controlled increase in the potential energy curve, contributing to improved overall stability and performance of the isolator.

Another significant advantage of parabolic surface geometry is the efficient use of the isolator's displacement capacity. As the surface slope increases with the position of the rolling element, the restoring force is activated earlier, preventing the system from reaching large displacements. In this way, effective acceleration reduction is achieved without utilizing the full displacement capacity of the isolator. This characteristic not only enhances performance efficiency but also allows for a reduction in the overall size of the isolator, enabling more compact and cost-effective design solutions.

Furthermore, the parabolic surface geometry extends the effective period of the system at low displacement levels, thereby reducing the accelerations transmitted to the structure and minimizing the influence of high-frequency components. Since the surface can be mathematically defined by the equation  $z = Ax^2$ , the stiffness profile and period characteristics can be easily optimized by adjusting the parameter  $A$ . This provides greater design flexibility compared to spherical or conical isolators, allowing the isolator's performance to be tailored to specific structural and seismic requirements. Figure 2.2 shows the parabolic surfaces obtained with different  $A$  values.

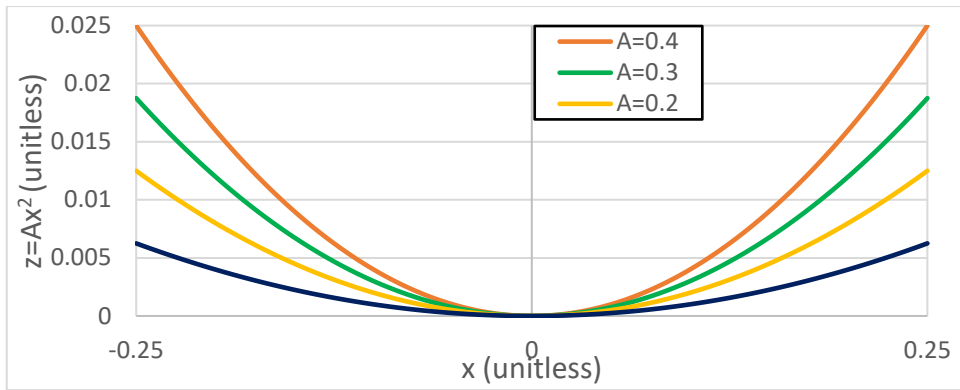


Figure 2.2 Comparison of parabolic surfaces obtained with different  $A$  values

In conclusion, the primary reason for preferring rolling-type parabolic-surface floor isolators (RPFI) lies in the superior dynamic properties provided by their unique surface geometry. In these floor isolators, the surface slope changes with the displacement of the rolling element, resulting in a naturally nonlinear stiffness behavior. At small displacements, the system exhibits greater flexibility, effectively reducing the base accelerations transmitted to the structure. At larger displacements, the increasing slope enhances stiffness, ensuring effective control of displacement limits. This variable slope also modifies the potential energy profile of the system, enabling more balanced energy dissipation performance, which enhances both the energy absorption capacity and the re-centering capability of the isolator. Furthermore, parabolic geometry allows the restoring force to increase with displacement, enabling efficient acceleration reduction before the maximum displacement capacity is reached. Since the parabolic surface can be defined by the equation  $z = Ax^2$ , the design parameters can be easily adjusted, allowing optimization of the system according to specific performance requirements. These characteristics make parabolic surface isolators a promising alternative to conical and spherical isolators in terms of both design flexibility and seismic performance. Therefore, this study aims to investigate parabolic surface floor isolators experimentally and analytically, optimize their geometric parameters, and quantitatively demonstrate their performance advantages through comparison with other surface geometries.

## 2.2 Methodology

This section briefly introduces the experimental and analytical studies conducted to comprehensively determine the structural behavior, dynamic characteristics, and performance limits of the proposed floor isolator system. A multi-stage research program was followed to determine the system's performance. A comprehensive workflow diagram showing the stages of the research process is presented in Figure 2.3. This flow diagram shows the project flow, starting with analytical work and continuing with experimental work.

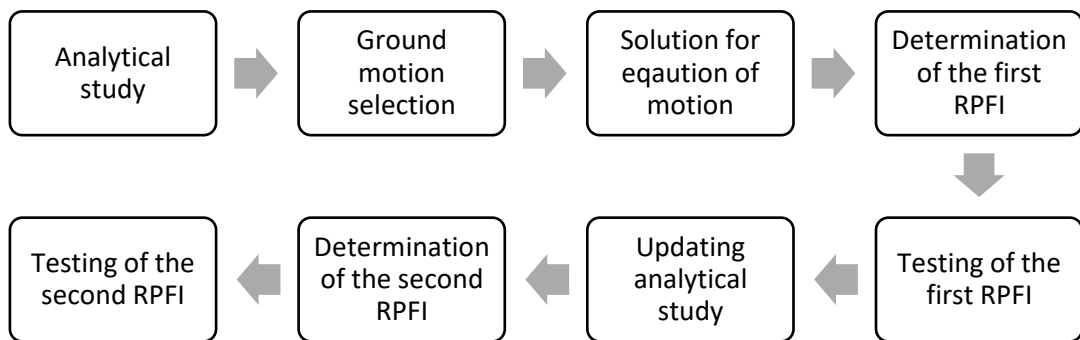


Figure 2.3 Flowchart showing the methodology of the study.

The methodology presented in the workflow diagram in Figure 2.3 can be classified into two main groups: analytical and experimental studies, encompassing both theoretical and applied approaches to the work carried out. These two main components of the research aim to validate the system's performance both through mathematical models and physical tests. In this context, general information on analytical study is discussed in Chapter 2.2.1, while general information on experimental work is discussed in Chapter 2.2.2.

### 2.2.1 Analytical Study

A comprehensive analytical study was conducted to determine the dynamic behavior and design parameters of the rolling-based parabolic-surface floor isolator (RPFI) developed in this study. The primary objective of this analytical approach is to predict the proposed isolator's acceleration reduction capacity, displacement demands, and overall dynamic characteristics under different seismic inputs, and to determine the appropriate geometric and mechanical parameters before proceeding to the experimental stage. In this context, the motion of a mass rolling on a parabolic surface was mathematically modeled, the fundamental dynamic equations of the system were established, and how the isolator behavior changes depending on the surface geometry and damping characteristics was investigated. Using the obtained model, parametric analyses were performed for different parabolic surface geometries; the balance between acceleration reduction performance and displacement capacity was evaluated, and the appropriate surface curves and capacity values for experimental prototypes were determined. Thus, the analytical study enabled both the rational selection of the isolator geometry and the target-oriented planning of the experimental program. The detailed mathematical derivations, numerical solutions, and parametric results of this analytical framework are presented in detail in Chapter 3.

Additionally, the selection of strong ground motions and the scaling process were also carried out at this stage. The selected strong ground motions were used both as input data in analytical study and in experimental studies. The use of this common dataset enabled the direct comparison of experimental findings with analytical results and the mutual validation of the analytical study. The selection criteria for strong ground motions, the scaling methodology, and a detailed technical discussion of the strong ground motions are presented in Chapter 4.

### 2.2.2 Experimental Study

An experimental program was designed to validate the isolator geometries determined in analytical study and the predicted dynamic behavior under actual physical conditions. Within this scope, a special test setup was created to ensure that the developed RPII prototypes could be tested in a safe, repeatable, and representative manner. In the design of the experimental setup, criteria such as the stroke, speed, and load capacity of the hydraulic actuator and the expected displacement requirements of the isolators were evaluated together. In addition, the design of the isolated floor and safety frame placed on the isolator was carried out to ensure both the structural integrity and measurement reliability of the system. Accelerometers and displacement sensors were installed as measurement systems, and the calibration and accuracy of the data were checked. Thus, the experimental environment was prepared to enable the physical observation and reliable measurement of the behaviors predicted in the analytical model. Detailed information on the design of this experimental setup is presented in Chapter 5.

By using the experimental setup discussed in Chapter 5, a systematic experimental program was conducted to determine the mechanical and dynamic performance of the proposed RPII prototypes. The primary objective of these experiments was to directly measure the isolator's acceleration reduction capacity, displacement demands, damping characteristics, and recall behavior under seismic effects and to compare them with analytical results. In this regard, loading tests revealing the force-displacement relationships on the isolators, free vibration tests, and strong ground motion tests were performed. Prototypes with different parabolic surface geometries were tested to experimentally evaluate the effects of surface curvature on system performance. The obtained data enabled the quantitative determination of the isolators' acceleration reduction ratios, displacement capacity utilization, and dynamic stability, revealing the system's effectiveness under real earthquake conditions. A detailed analysis and discussion of these experimental findings are presented in Chapter 6.

### **2.2.3 Discussion on Methodology**

The methodology followed in this study is based on a comprehensive framework aimed at reliably evaluating a rolling-type parabolic-surface isolator both theoretically and experimentally. First, the fundamental dynamic characteristics of the system, the surface geometry–performance relationship, and the expected acceleration and displacement demands were predicted by using analytical modeling. This allowed the design parameters to be rationally established before proceeding to the experimental phase. This analytical pre-evaluation enabled the creation of a targeted experimental program instead of random prototyping. Subsequently, specially designed test setup was used to test isolator prototypes under controlled conditions and directly measure their behavior under real earthquake records. This approach allowed analytical results to be compared with experimental observations, comprehensively validating the system's reliability and performance. As a result, the methodology provides a robust validation process.

## CHAPTER 3

### ANALYTICAL STUDY OF ROLLING-TYPE PARABOLIC-SURFACE FLOOR ISOLATOR (RPFI)

#### 3.1 Derivation of the Equation of Motion for Parabolic Surfaces

This section aims to understand the basic working principle of the floor isolation device through an analytical study. To determine the parameters of a parabolic surface isolator, the equation of motion on a theoretical parabolic surface was derived based on the geometric variables. The equation of the parabolic surface is assumed to be  $z = Ax^2$ , and the relevant calculations are performed parametrically. Figure 3.1 presents this geometry and some relevant specific parameters. In this figure, the value  $x_{max}$  represents the maximum horizontal displacement of the parabolic floor isolator, while  $z_{max}$  denotes the maximum vertical displacement observed during this maximum horizontal displacement. The parameter  $R(x)$  indicates the equivalent radius, which varies dependent on the variable  $x$  relative to a fixed-point  $O$ . Consequently, the value of  $R(x)$  is not constant but changes with  $x$ .

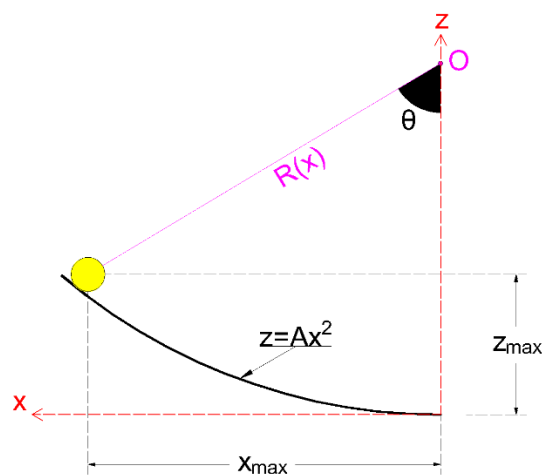


Figure 3.1 Geometry of the proposed parabolic floor isolator

The free-body diagram and kinetic diagram used in the calculation of the analytical equation are shown in Figure 3.2 as obtained in the tangential and normal coordinate axes. In the Free-Body Diagram (FBD), one of the fundamental forces acting on the system is the weight (denoted by  $W$ ). This force acts along the direction of gravity, specifically in the negative  $z$ -axis direction. Another important force present in the FBD is the damping force ( $F_d$ ). This force represents the damping effect of the system and is applied in the direction opposite to the motion, along the horizontal axis. The last force present in the FBD is the earthquake excitation (denoted by  $m\ddot{u}_f$ ), which is used to model the effect of the earthquake. The earthquake effect is applied to the system along the horizontal  $x$ -axis. In the Kinetic Diagram (KD), the inertia is analyzed. These forces are shown along the normal ( $n$ ) and tangential ( $t$ ) axes defined at the point where the motion is being examined.

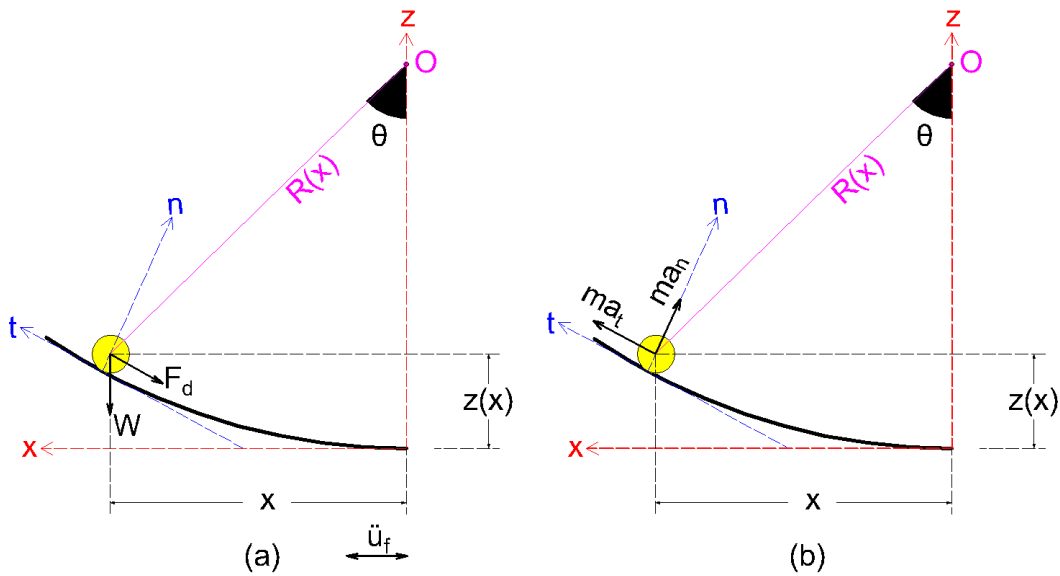


Figure 3.2 Parabolic isolator system a) free body diagram b) kinetic diagram

The position vector of the ball moving on the parabolic surface shown in Figure 3.2 can be written as in Equation 3.1.

$$\hat{r} = x\hat{i} + (Ax^2)\hat{k} \quad (3.1)$$

The velocity vector of the object moving on the parabolic surface can be found by using the position vector given in Equation 3.1. To determine velocity vector, the first derivative of the position vector in Equation 3.1 is taken. The velocity vector of the moving ball on parabolic surface is given in Equation 3.2.

$$\hat{v} = \frac{d\hat{r}}{dt} = \dot{x}\hat{i} + (2Ax\dot{x})\hat{k} \quad (3.2)$$

The acceleration vector can be found by taking the derivative of the velocity vector. The acceleration vector is given in Equation 3.3.

$$\hat{a} = \frac{d\hat{v}}{dt} = \ddot{x}\hat{i} + (2A\dot{x}^2 + 2Ax\ddot{x})\hat{k} \quad (3.3)$$

The tangent vector is required to obtain the equation of motion. The tangent vector for the parabolic surface is as given in Equation 3.4.

$$\hat{T} = \hat{i} + (2Ax)\hat{k} \quad (3.4)$$

The damping force can be written as  $F_d = -c\hat{v}$ , depending on the velocity vector given in Equation 3.2. By using this information, the equilibrium equation can be written as Equation 3.5.

$$(-W\hat{k} - m\ddot{u}_f\hat{i} - c\hat{v}) \cdot \hat{T} = m\hat{a} \cdot \hat{T} \quad (3.5)$$

When all vectors are substituted into Equation 3.5, Equation 3.6 is obtained.

$$(-W\hat{k} - m\ddot{u}_f\hat{i} - c(\dot{x}\hat{i} + 2Ax\dot{x}\hat{k})) \cdot (\hat{i} + 2Ax\hat{k}) = m(\ddot{x}\hat{i} + (2A\dot{x}^2 + 2Ax\ddot{x})\hat{k}) \cdot (\hat{i} + 2Ax\hat{k}) \quad (3.6)$$

If the vector operations in Equation 3.6 are performed, the equality given in Equation 3.7 is obtained.

$$-2Amgx - m\ddot{u}_f - c(\dot{x} + 4A^2x^2\dot{x}) = m(\ddot{x} + 4A^2x\dot{x}^2 + 4A^2x^2\ddot{x}) \quad (3.7)$$

If the expressions in Equation 3.7 are rearranged, Equation 3.8 is obtained.

$$(1 + 4A^2x^2)m\ddot{x} + (1 + 4A^2x^2)c\dot{x} + (2Ag + 4A^2\dot{x}^2)mx = -m\ddot{u}_f \quad (3.8)$$

$F_d$  given in Figure 3.2 represents the damping force and accounted for parametrically in the calculations. Although there are various mechanisms that provide damping force, the primary source of damping force in the proposed floor isolator is the friction effect. In rolling-based isolator systems, the friction force occurs in the point contact area between the rolling element and the surface of the isolator. Although the friction force generated due to the limited contact area is limited in magnitude, it retains its characteristic of being the fundamental component that determines the total damping capacity of the system. In other words, the damping force is directly dependent on the friction coefficient between the rolling element and the contact surface and the interface interaction. In particular, surface roughness arising from the manufacturing processes of parabolic surfaces increases friction resistance, thereby increasing the damping capacity of the system. This highlights the decisive role of manufacturing precision on damping performance.

In the solution of the equation of motion, the damping effect of the system is included with damping ratio (denoted by  $\xi$ ). The accurate determination of the system's damping ratio  $\xi$ , and the subsequent calculation of the damping force, cannot be achieved without free vibration experiments. Due to this necessity, the damping ratio was initially adopted as an assumed value of 1% in the first phase of the analytical study, and the analytical solution was carried out by using this value. Experimental studies were conducted on the first prototype designed based on the results of this analytical work, and the actual damping ratio of the system was determined through these experiments. In the design process of the second prototype, the damping ratio value was calculated using the mathematical relationship defined for double-curved surface seismic isolators in the TEC (2018). The validity and accuracy of this mathematical relationship were checked and confirmed by means of the results obtained from the first prototype experiments.

The damping coefficient,  $c$ , can be written as  $c = 2m\xi\omega_n$  in terms of the damping ratio. Additionally, entire equation is divided by  $m$  and the final form of the equation of motion, which includes the damping ratio, is presented in Equation 3.9.

$$(1 + 4A^2x^2)\ddot{x} + (1 + 4A^2x^2)(2\xi w_n)\dot{x} + (2Ag + 4A^2\dot{x}^2)x = -\ddot{u}_f \quad (3.9)$$

With reference to the equation of motion in Equation 3.9, the natural frequency of the system is also calculated parametrically as in Equation 3.10.

$$w_n = \sqrt{2Ag + 4A^2\dot{x}^2} \quad (3.10)$$

As a result, the equations of motion of the parabolic surface isolator were obtained. This parametric study aims to determine a parabolic surface suitable for the desired design targets by obtaining a solution set for the specified  $x$  and  $z$  sets. By numerically obtaining the parabolic system response using different  $A$  coefficients, a parametric solution will be realized, and the most suitable geometries for the desired performance targets can be determined.

### 3.2 Solution of the Equation of Motion

For the equation of motion obtained parametrically in Equation 3.9, a solution set was obtained by using MATLAB (2024) the software to determine the final numerical parameters that will determine the geometry of the parabolic surface. This solution set was calculated with  $x_{max}$  and  $z_{max}$  variables according to the equation of motion of the system, considering the isolator dimensions, production possibilities, and damping target. In these variables,  $x_{max}$  represents the maximum displacement in the horizontal direction and the displacement capacity of the parabolic surface isolator, and  $z_{max}$  represents the height between the lowest center point of the isolator and the top point of the isolator (isolator surface depth - maximum parabola vertical distance). The final solution set for these variables was derived by evaluating several interlocking constraints and objectives. The primary performance target guiding this selection was the desired 80% reduction in acceleration response, a value derived from the work of Vargas & Bruneau (2006). By using selected ground motions, a dynamic solution (Newmark solution) was performed for each  $x_{max}$ - $z_{max}$  combination, and acceleration, velocity, and

displacement data were obtained. The average results obtained from the ground motion set were compiled.

To create the target set of  $x_{max}$  and  $z_{max}$  variables used in the parametric equation, the limits of each variable were determined. While creating the target set of the  $x_{max}$  variable corresponding to the highest displacement, the target set was created by considering this maximum displacement limit. Accordingly, considering the modularity of the floor isolator and the production stage of the isolator, a range of displacement capacity ( $x_{max}$ ) was determined as the highest 40 cm and the lowest 15 cm. In this value range, 6 different values with 5 cm intervals were determined, and a solution set was formed for the  $x_{max}$  variable. Limits for the variable  $z_{max}$ , which corresponds to the isolator surface depth, were determined considering the production conditions and material thickness. Accordingly, for the depth of the isolator ( $z_{max}$ ) variable, a parameter set was formed by determining 31 different values with an increase of 0.1 cm in a range of minimum 1 cm and maximum 4 cm, considering the material thickness. As a result of the combinations generated using these  $x_{max}$  and  $z_{max}$  sets, the dynamic solution results are obtained under the GM Set-1 discussed in Chapter 4.

The damping ratio of the device is a critical parameter in analytical solutions, as it significantly influences the device's performance under seismic loading. However, the damping ratio of the device cannot be accurately determined without test results. In this context, the damping calculation method recommended by the TEC (2018) for circular-surface friction isolators was examined. Although the approach defined in the specification exhibits geometric similarities to parabolic-surfaced isolators, there is no experimental evidence confirming its validity for such systems. While direct application of this method might appear reasonable due to geometric similarities, differences in surface configuration can lead to variations in energy dissipation mechanisms. For this reason, the damping calculation defined in the specification was not adopted in the design of the first prototype. Instead of using this calculation method, the closest experimental data available in the literature was

used as a reference in parametric study for determining the prototype. In the determination of the damping ratio, the data obtained from the conducted floor isolator experiments by Vargas & Bruneau (2006) were taken as reference. Specifically, the test results pertaining to conical surface floor isolators, which exhibit close dimensional proximity despite lacking complete geometrical similarity, were adopted as the primary reference point. In this context, the 1% constant damping ratio obtained from the conical surface isolator experiments was adopted as the initial assumption. Although this value has not been directly verified for the parabolic surface system, it was used as a temporary reference to guide the design process in parametric analyses of the first prototype.

After the damping assumption, Equation 3.9 was solved for different parabolic surfaces, and the results were compiled. The geometry of the first prototype with a parabolic surface was determined by evaluating the results obtained. Two basic criteria for selecting the device geometry were defined in the parametric study. The first of these is the acceleration reduction ratio (ARR). The acceleration reduction ratio is defined as the ratio of the difference between the maximum ground acceleration (PGA) and the absolute maximum acceleration measured on the isolated slab to the maximum ground acceleration (PGA). This value is a critical performance metric that indicates the degree to which the isolator mitigates seismic loads. The relationship for acceleration reduction ratio is given in Equation 3.11.

$$ARR(\%) = \frac{|\ddot{x}_{g,max}| - |\ddot{x}_{slab,max}|}{|\ddot{x}_{g,max}|} * 100 \quad (3.11)$$

The second criterion for device selection is the displacement capacity utilization ratio (DCUR). The displacement capacity utilization ratio expresses the ratio of the absolute maximum displacement demand on the isolated slab to the displacement capacity of floor isolator. This parameter indicates how much of its displacement capacity of the isolator utilizes under seismic loads. The relationship for displacement capacity utilization ratio is given in Equation 3.12.

$$DCUR(\%) = \frac{|x_{max,isolator}|}{|x_{design,isolator}|} * 100 \quad (3.12)$$

The parametric study related to the acceleration reduction ratio and displacement capacity utilization ratio is presented in Figure 3.3 and Figure 3.4, respectively. These results were obtained by taking the average of the results calculated for the 17 strong ground motions in the GM Set-1 discussed in Chapter 4.

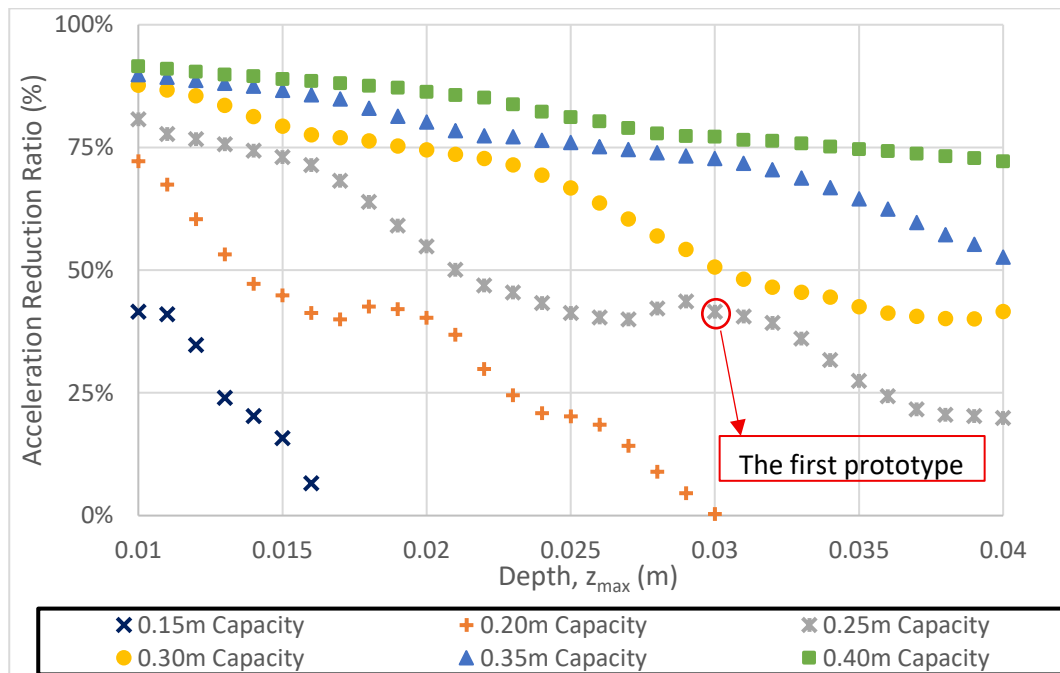


Figure 3.3 Acceleration reduction ratio results obtained after a parametric study conducted with 1% damping ratio

When examining the acceleration reduction ratio presented in Figure 3.3, it is observed that, as a general trend, as the displacement capacity of the floor isolator increases, the acceleration reduction ratio of the system also increases. This situation shows that isolators with higher displacement capacity can more effectively reduce the accelerations transferred to the floor isolated system during an earthquake. However, this increase in displacement capacity also directly requires an increase in the size of the isolators. The increase in isolator dimensions leads to higher production costs and difficulties in maintaining the modular structure, making it an undesirable situation both economically and in terms of applicability. For this reason,

in the selection of the prototype, the displacement capacity was carefully kept below the value of  $x = 0.4 \text{ m}$ .

Another important finding obtained from the Figure 3.3 is the inverse relationship between the maximum depth of the isolator and the acceleration reduction ratio. This trend, which is expected due to the nature of dynamic behavior, is also clearly evident in the analysis results. In other words, as the depth of the parabolic surface increases, the acceleration reduction ratio shows a decreasing trend.

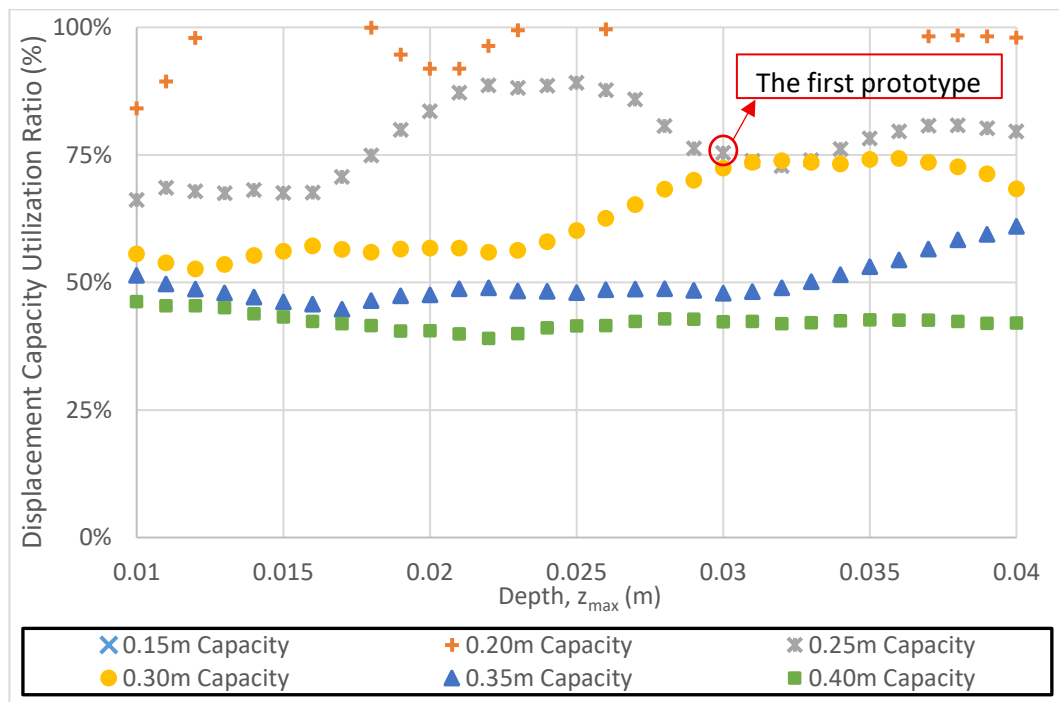


Figure 3.4 Displacement capacity utilization ratio results obtained after a parametric study conducted with 1% damping ratio

In Figure 3.4, a distinct inverse proportionality is observed between the displacement capacity of the floor isolator and displacement capacity utilization ratio. As the system's displacement capacity increases, the displacement utilization ratio of that capacity decreases. According to the data presented in Figure 3.4, the devices with a 0.4m displacement capacity exhibited the lowest displacement capacity utilization ratio. Conversely, devices with 0.15m and 0.2m displacement capacities were observed to exceed their displacement capacity. Furthermore, devices possessing

displacement capacities ranging between 0.25m and 0.35m demonstrated a relatively more balanced performance.

When investigating the effect of  $z_{max}$  which is another parameter of isolator, on the results, it was concluded that this parameter does not significantly influence the device's capacity utilization ratio. This outcome stems from the assumption of a constant damping ratio in the analytical model. However, it is hypothesized that the device geometry affects the damping mechanism, and different device geometries may inherently possess different damping ratios. Therefore, it is probable that the results in this section of the analytical study do not fully reflect the actual system behavior. Following the experimental tests of the initial prototype, which will be determined based on these first analytical results, the validity of the effective damping ratio formula prescribed in the TEC (2018) will be tested. Subsequently, the revised damping ratio calculation, informed by the acquired experimental data, will be employed in the design of the second prototype. These stages will be discussed in detail in the following sections of this chapter.

Based on these observations, it was concluded that the design should ensure compliance with displacement limits while remaining feasible to manufacture within reasonable tolerances. Accordingly, the objective was to identify a balanced prototype that enhances the performance of the isolator, while also accounting for production challenges and constraints associated with modularity.

In order to maintain modularity conditions and meet performance targets, the displacement capacity of the isolator has been set at  $x_{max} = 0.25m$  and the maximum isolator depth ( $z_{max}$ ) has been selected as 0.03 m, thus establishing the initial design geometry. The calculated acceleration reduction ratio and displacement utilization ratio for this design are 0.41 and 0.75, respectively. Selected geometry for first prototype is marked in Figure 3.3 and Figure 3.4.

However, the main purpose of the first prototype is not only to fulfill the performance criteria but also to test the manufacturability of the parabolic surface geometry. Therefore, the first prototype will be manufactured based on the specified

dimensions. Through the findings obtained during the manufacturing process, the manufacturing tolerances will be examined in detail and the feasibility of producing more precise surface geometries (lower  $z_{max}$  values) will be verified by running quality control processes. Thus, it has been adopted as a strategic approach to move towards designs with lower z-height in the prototype alternatives to be produced in the following stages, thus both benefiting from the experience gained during the production process and achieving the targeted acceleration reduction rate.

At this point, it is important to emphasize that the acceleration reduction ratios obtained were calculated under the assumption of 1% structural damping. It is possible that the assumed damping ratio of 1% adopted at the onset of the analytical study differs from the system's actual damping ratio (either lower or higher). This inconsistency will inevitably lead to variations in critical performance parameters such as the system's acceleration reduction ratio and displacement capacity utilization ratio. Consequently, the current analytical results obtained under the 1% damping ratio assumption will be recalculated and updated using the realistic damping ratio value determined after the first prototype experiments. This re-analysis is of critical importance for ensuring that the theoretical model aligns more accurately with the experimental data.

As a result, the parabolic surface of the first prototype with a parabolic surface is defined as presented in Equation 3.13.

$$x_{max} = 0.25m, z_{max} = 0.03 m \rightarrow z = 0.48x^2 \quad (3.13)$$

The production drawings of the first prototype, whose parabolic surface equation is given in Equation 3.13, were modeled using Solidworks (2024) program. CAD drawings of the prototype are given in Figure 3.5.

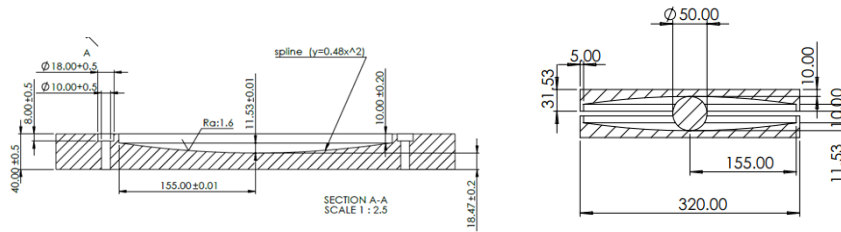


Figure 3.5 Two-dimensional CAD drawings of the first prototype of the RPI

In this section, the basic equation of the first prototype geometry is briefly presented. In the process of deriving the equation, the symmetry of the surface about z-axis and the ease of mathematical operations like differentiation and integration were considered as the primary criteria. In the light of these criteria, the equation of the parabolic surface was defined in a simple form as  $z = Ax^2$ . This equation provides a suitable basis for both the simplification of analytical calculations and a more explicit study of the dynamic behavior of the system. Using the determined parabolic surface equation, the equations of motion of the isolator were derived and it was seen that these equations depend on the coefficient  $A$ . Manufacturing conditions, size limitations and performance targets were evaluated together, and a parametric study was carried out to finalize the geometry of the device prototype. With this study, the effects of different  $A$  parameters on the displacement capacity and acceleration reduction performance of the isolator were systematically investigated.

As a result of the evaluation of the obtained results, a prototype of a RPI that meets the displacement capacity and reasonably meets the performance targets has been determined. The final design was finalized to have a displacement capacity of 250 mm and the relevant parabolic surface equation was determined as  $z = 0.48x^2$ . Thus, the basic geometrical parameters and capacity of the first parabolic isolator to be produced were clarified and the design phase of the first prototype was successfully completed.

### 3.3 Parametric Study for Damping Coefficient

In order to increase the accuracy and reliability of the analytical study, the damping ratio, which is one of the most important parameters directly affecting the behavior of the isolator, must be calculated accurately. It is essential to compute the damping for every geometry examined in the parametric analysis, not solely for a single surface. The changes in the geometry of the parabolic surface influence the dynamic behavior of the system, hence causing variations in the damping ratio. Therefore, it is necessary to calculate a unique damping ratio for each parabolic surface.

The corresponding damping ratio can be determined experimentally through direct free oscillation experiments or analytically by using various mathematical approaches. However, conducting experimental studies for each parabolic surface separately is not feasible in terms of time, cost and practical difficulties. Upon reviewing the existing literature and current regulations, it is evident that no damping calculation method is explicitly suggested for an isolator with parabolic surfaces. However, mathematical damping calculation methods are proposed in the specifications for frictional isolators with curved surfaces that are geometrically similar to parabolic surfaces. The effective damping ratio calculation recommended is given in Equation 3.13 within Chapter 14 of TEC (2018). The equivalent radius ( $R_{eq}$ ) in Equation 3.13 was determined by using MATLAB (2024). For each parabolic surface, the equivalent radius closest to this surface was determined. The parameter denoted by  $D$  is the displacement capacity of the floor isolator. Finally, the friction coefficient has been determined. Using Equation 3.14 and the damping ratio obtained from the first prototype experiments, the friction coefficient was calculated as 0.01, and this ratio was used for all other surfaces.

$$\xi_{eff} = \frac{2}{\pi} \left[ \frac{\mu_e}{\mu_e + D/R_{eq}} \right] \quad (3.14)$$

In order to use this calculation method in the damping calculation of parabolic isolator, its accuracy needs to be verified. Therefore, the damping obtained from this

proposed calculation method is compared with the experimental results. The damping ratio calculated using Equation 3.14 is compared with the damping ratio obtained from the free oscillation experiment of the first prototype. The results obtained are presented in Table 3.1. As a result of this comparison, it is seen that Equation 3.13 can be used in the calculation of the parabolic surface isolator.

Table 3.1 Comparison of the damping ratio obtained from the experiment and the damping ratio obtained by using Equation 3.14

<b>Parabolic Surface Equation</b>	<b>Experimental Damping Result (%)</b>	<b>Analytical Damping Result (%)</b>
$z=0.48x^2$	4.75	4.82

In conclusion, the analyses and comparisons show that Equation 3.14 provides a feasible method for the approximate calculation of the damping ratio of a parabolic isolator. The strong correlation between the Equation 3.14 and the data from free oscillation experiments validates the accuracy and reliability of the analytical method. According with these findings, Equation 3.14 has been integrated into the analytical code created in to enable the calculation of the damping ratio independently for isolator prototypes with varying parabolic surface geometries. Thus, the specific damping ratios for each surface geometry were automatically calculated and the analysis results were systematically compiled according to these values. This approach reduces the need for experimental studies and allows fast and efficient determination of the damping characteristics of parabolic isolator with different surface geometries.

The parametric study previously performed in Chapter 3.2 with 1% damping ratio for the parabolic surface isolator was repeated with the new damping ratios. The dynamic study repeated utilizing various parabolic surfaces and a modified damping ratio, employing the GM Set-1 discussed in Chapter 4. As a result of this study, the displacement capacity ( $x_{max}$ ) and depth ( $z_{max}$ ) dependent effective damping results of the parabolic surface are presented in Figure 3.6.

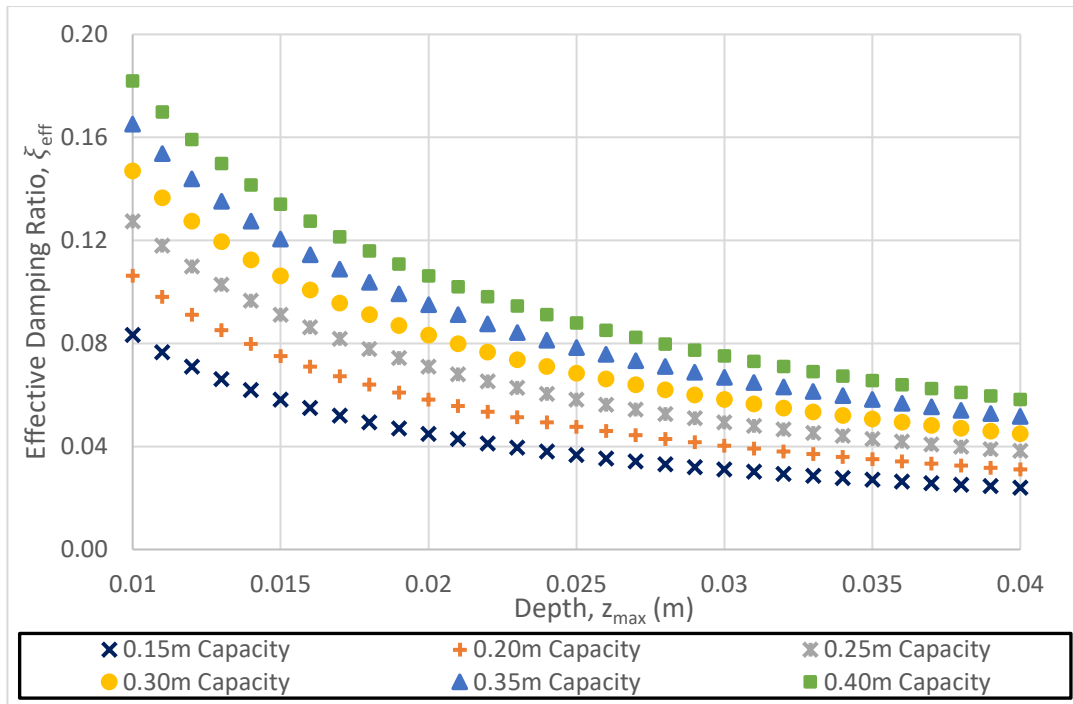


Figure 3.6 Effective damping ratio results calculated by using Equation 3.14

Figure 3.6 presents the depth dependence of the effective damping ratios for different capacity values in the range of 0.15 m - 0.4 m within the scope of the parametric study performed for the parabolic floor isolator. The plot clearly illustrates that effective damping for each capacity value has a declining trend as depth increases. However, as the capacity value increases, it is observed that higher effective damping ratios are achieved at each depth level. This finding indicates that increasing the isolator displacement capacity positively affects the damping performance. As a result of this study, the effective damping ratios of different parabolic surfaces were calculated. The parametric study was repeated by using these effective damping ratios and the results are given in Chapter 3.4.

### 3.4 Updated Analytical Study Results after Damping Calculation

The damping ratio results from Chapter 3.3 were evaluated within the scope of the parametric study mentioned in Chapter 3.2, and the study was performed again. This stage involved considering various damping ratios for each parabolic surface

geometry, providing a more precise assessment of the system in the analysis. This method facilitated simultaneous assessment of the effects of surface shape and the appropriate damping ratio on system efficacy.

Calculated new damping ratios were used to determine the geometry of the second prototype with a parabolic surface. As with the first prototype, two main performance criteria were taken into account in this selection process. These are the acceleration reduction ratio, which expresses the capacity of the isolator to reduce the accelerations transferred to the floor isolated system, and the displacement capacity utilization ratio, which reveals the safe operation performance of the isolator within the prescribed limits.

The reanalysis performed in this chapter, based on the unique damping ratios for each parabolic surface, allowed for a more accurate, reliable and realistic description of the second prototype. This approach not only increased theoretical accuracy, but also provided a more rational engineering basis for the design process. Thus, the process of identifying the second prototype has become more compatible with performance targets and more feasible in terms of production and application.

The acceleration reduction results obtained from repeated parametric study by using new damping ratios are compiled. This study reveals the effect of different capacity (0.15 m-0.4 m) and device depth on acceleration reduction performance. The data obtained are presented in Figure 3.7 with device depth ( $z_{max}$ ) on the horizontal axis, acceleration reduction ratio (%) on the vertical axis and a different symbol for each device capacity.

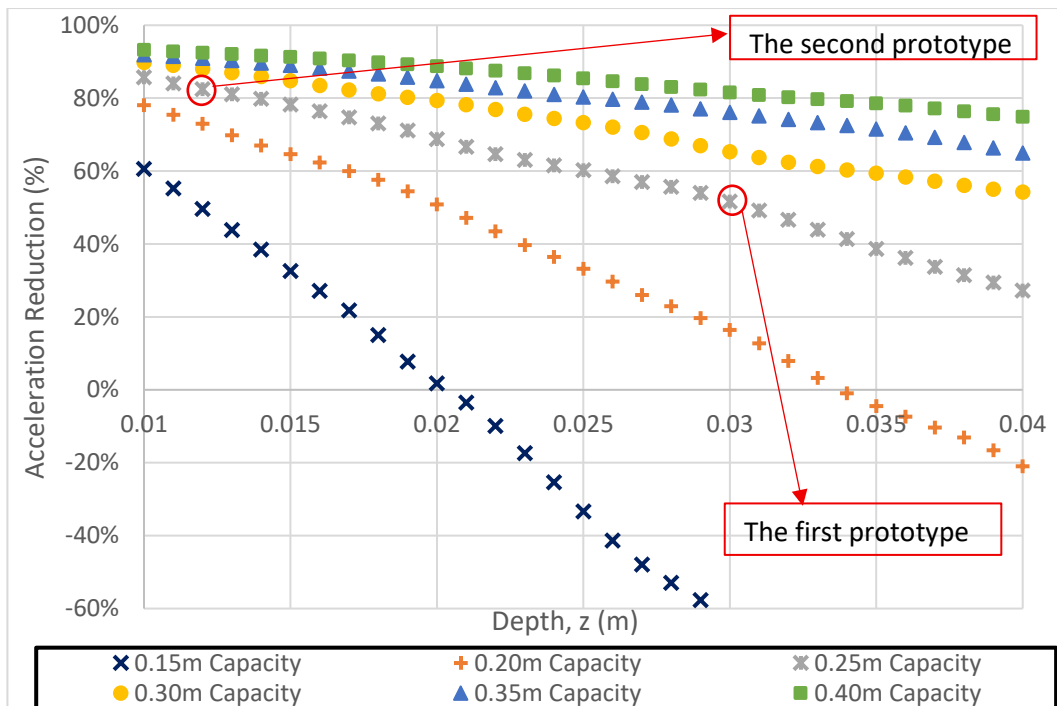


Figure 3.7 Relationship between acceleration reduction ratio calculated with new damping ratios and device geometry

The primary objective of this study is to develop a parabolic surface floor isolator capable of achieving more than 80% reduction in acceleration. The results of the parametric analyses indicate that the displacement capacity of the isolator is a critical parameter governing its acceleration reduction performance. As illustrated in Figure 3.7, systems with displacement capacities of 0.40 m and 0.35 m achieve acceleration reduction exceeding 80% across a wide range of depth values. This finding demonstrates that larger displacement capacities contribute to more effective seismic performance and are capable of meeting the targeted performance criteria. Nevertheless, an increase in displacement capacity does not always yield an optimal solution, particularly when factors such as cost efficiency, scalability, and modular adaptability are taken into account. Therefore, it is essential to identify an optimum isolator geometry that ensures economic feasibility, maintains modularity, and simultaneously satisfies the study’s performance requirements.

Conversely, systems with lower displacement capacities, such as 0.15 m and 0.20 m, perform substantially below the targeted acceleration reduction threshold. In such

cases, the system fails to provide effective seismic isolation due to inadequate displacement capacity, and in certain instances, the isolator even amplifies the acceleration transmitted to the isolated slab rather than reducing it. Notably, in the system with a capacity of 0.15 m, the acceleration reduction ratio assumes negative values, indicating that the isolator amplifies the seismic response of the slab. This outcome highlights the inadequacy and potential risk of low-capacity isolators in terms of seismic performance.

The findings further suggest that medium-capacity systems, particularly those with displacement capacities of 0.25 m and 0.30 m, achieve a more balanced performance, combining effective acceleration reduction with structural modularity. Parametric analyses confirm that these configurations can achieve approximately 80% acceleration reduction, thereby representing a promising compromise between performance and modularity. However, acceleration reduction ratio is not a sufficient criterion alone in selecting the geometry of the second prototype. In addition, the displacement capacity utilization ratio must be considered alongside the reduction in acceleration. The extended parametric study conducted with varying damping ratios demonstrates the combined influence of displacement capacity and device depth on the utilization efficiency of the isolator. The corresponding data are presented in Figure 3.8, where the horizontal axis represents device depth ( $z_{\max}$ ), the vertical axis denotes the displacement capacity utilization ratio (%), and different symbols are used to distinguish the capacities of the tested systems.

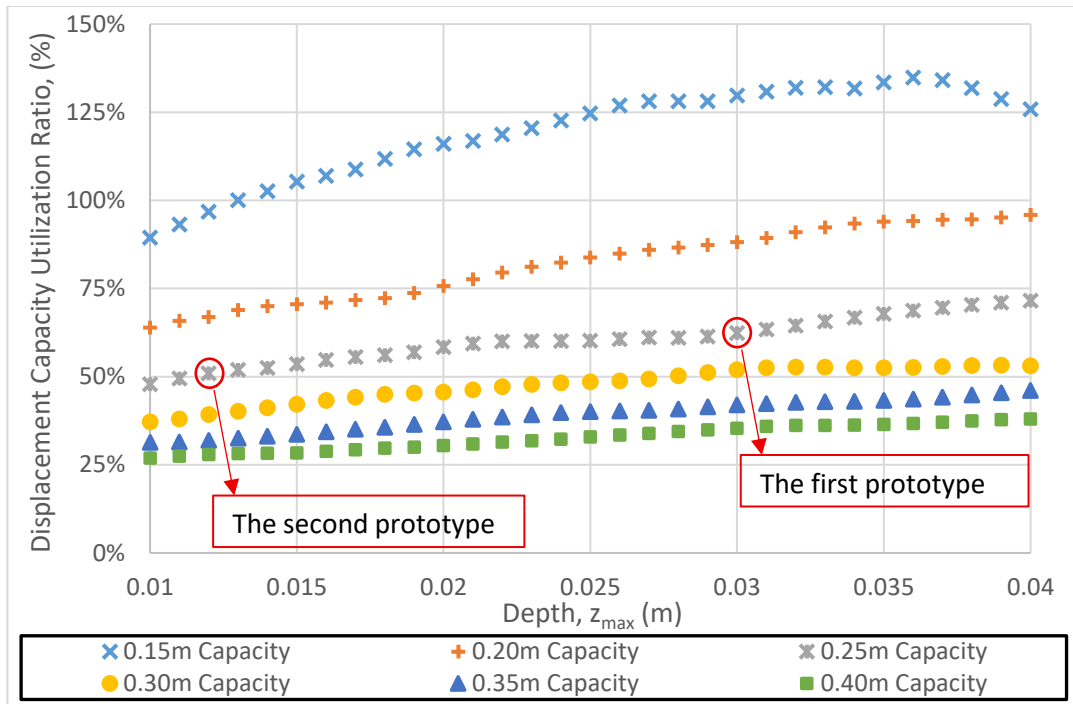


Figure 3.8 Relationship between displacement utilization ratio calculated with new damping ratios and device geometry

Figure 3.8 presents the outcomes of a parametric study examining the relationship between device depth ( $z_{max}$ ) and displacement capacity utilization ratio (%) in seismic isolation systems with varying displacement capacities (0.15 m–0.40 m). The analysis reveals a pronounced inverse correlation between isolation depth and utilization rate across all configurations. This relationship arises because, as the depth increases, the damping ratio decreases correspondingly, as illustrated in the depth–damping ratio curve in Figure 3.6. A reduction in damping ratio leads to an increased displacement demand, which in turn elevates the displacement capacity utilization rate of the device. When systems with different displacement capacities are compared, distinct behavioral patterns emerge. Low-capacity systems (0.15 m–0.25 m) exhibit proportionally higher utilization rates, whereas higher-capacity configurations (0.35 m–0.40 m) demonstrate significantly lower demand. This non-linear response underscores the critical role of displacement capacity in the design of isolation systems. While an increase in displacement capacity generally enhances

performance metrics, the findings indicate that this improvement is strongly influenced by the depth parameter.

The results highlight the complex interaction between displacement capacity and device depth, emphasizing the necessity of integrated design strategies that account for both parameters simultaneously. In particular, the consistent performance observed in medium-capacity systems (0.25 m–0.30 m) across varying depths suggests that isolators within this range represent the most promising candidates for final product selection.

The geometry of the second prototype of the parabolic isolator was determined by considering these results. The selected prototype should show at least 80% acceleration reduction and should not exceed displacement limits. The geometry that satisfies these criteria has been selected and is shown in Figure 3.7 and Figure 3.8. The equation of selected parabolic surface is presented in Equation 3.15.

$$x_{max} = 0.25m, \quad z_{max} = 0.012m \rightarrow z = 0.192x^2 \quad (3.15)$$

The production drawings of the second prototype, whose parabolic surface equation is given in Equation 3.15, were modelled using Solidworks (2024) software. CAD drawings of the prototype are given in Figure 3.9.

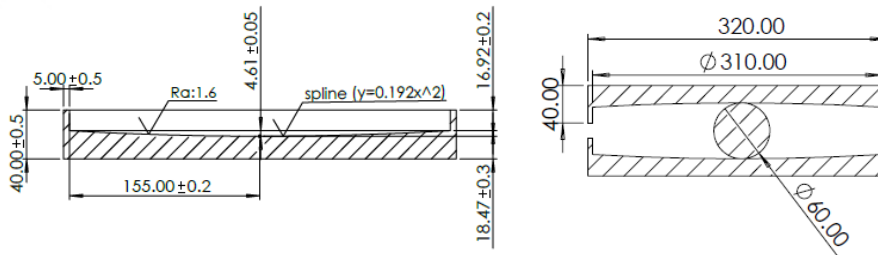


Figure 3.9 Two-dimensional CAD drawings of the second prototype of the RPI

The parametric study was re-performed using the damping ratios calculated in Chapter 3.3 and the geometry of the second prototype was selected according to the findings. As a result of the analytical investigation, the acceleration reduction rate for this parabolic isolator was calculated as 82.5% and the displacement capacity utilization ratio was determined as 50.9%. The parabolic surface equation of the

second prototype is given in Equation 3.15 and the production drawings in accordance with this equation are presented in Figure 3.9. This prototype was manufactured by using mentioned CAD drawings and dynamic tests were performed. The results obtained and the discussions about these results are presented in CHAPTER 6.

### **3.5 Brief Summary of Analytical Study**

This chapter presents the analytical derivation of the equation of motion for RPFI, and the subsequent parametric studies used to determine its design geometry. The equation of motion was formulated. A parametric solution set was generated using MATLAB (2024), where displacement capacity ( $x_{\max}$ ) and isolator depth ( $z_{\max}$ ) were systematically varied to evaluate acceleration reduction and displacement utilization performance under strong ground motions. The first prototype geometry was selected with  $x_{\max} = 0.25$  m and  $z_{\max} = 0.03$  m, achieving an acceleration reduction ratio of 41% and displacement utilization of 75%. Later, damping ratios were calculated analytically and validated by using experimental results of the first prototype. By using these damping ratios, the parametric study was repeated, leading to the design of a second prototype. After this optimization, the second prototype was selected with an acceleration reduction of 82.5% and a displacement utilization ratio of 50.9%. The chapter concludes by finalizing the parabolic surface equations and CAD models for both prototypes, establishing a balance between seismic performance, manufacturability, and modularity.



## CHAPTER 4

### EARTHQUAKE GROUND MOTIONS

Two different sets of strong ground motion records were compiled to facilitate the solution of the equation of motion and to perform dynamic tests. The selection of these records was based on specific criteria to ensure their suitability for the intended analyses. The earthquake ground motion data set consists of recordings from seismic events with moment magnitudes greater than 6.0 ( $M_w > 6.0$ ), sourced from the PEER-NGA (2024) strong ground motion database. In addition to this, only records with peak ground accelerations exceeding 0.05g ( $PGA > 0.05g$ ) were considered. Furthermore, the selected records were obtained from stations located on sites classified as ZC, which corresponding shear wave velocities in the range of  $360 \text{ m/s} < V_{s,30} \leq 720 \text{ m/s}$ . Ground motion recordings in both principal directions that met these criteria were included in the dataset, and acceleration response spectra were subsequently derived from these records.

At this stage, the target acceleration response spectrum to be used for scaling has been identified. The objective is to define a representative seismic hazard that captures the general characteristics of seismic activity across various regions of Turkey while also imposing sufficiently demanding conditions to evaluate the performance of the devices under investigation. This developed system has a wide range of potential applications in critical infrastructure and facilities such as data centers, museums, and power transmission lines. Since there is no specific standard or design protocol directly defined in the literature for the seismic protection of sensitive contents in data centers and museums, this study has utilized specifications defined for power transmission systems. In this context, the acceleration response spectrum proposed by Sucuoğlu et al. (2021) and Kaatsız et al. (2024) was adopted. This spectrum, defined for a 5% damping ratio, corresponds to the moderate level

specified in the Design Specification for Electrical Transmission Systems and Communication Facilities Under Earthquake Effects (2021). The corresponding linear elastic design spectrum is illustrated in Figure 4.1. This response spectrum represents a significant seismic hazard due to its characteristics, including elevated peak ground acceleration values and high acceleration demands in the short-period range. The floor isolation systems to be developed are intended for use in applications such as data center hardware and equipment within electrical transmission facilities. Therefore, it was deemed appropriate to conduct the analysis and testing of prototype devices under a seismic hazard level representative of the demands expected in these operational environments.

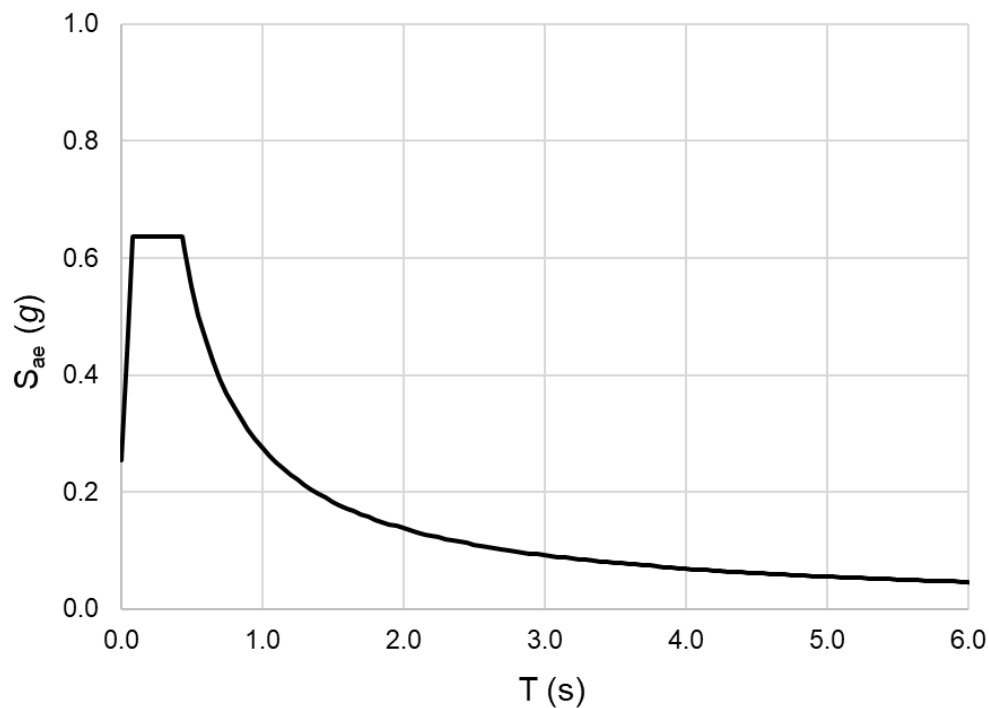


Figure 4.1 Moderate level, 5% damped acceleration design spectrum according to Design Specification for Electrical Transmission Systems and Communication Facilities Under Earthquake Effects (2021)

The strong ground motion set, compiled based on the criteria outlined above, was subjected to an amplitude scaling procedure in accordance with the provisions of TEC (2018), allowing the determination of individual scaling coefficients for each

record. These coefficients were subsequently evaluated, and records requiring scaling factors outside the range of 0.5 to 4.0 were excluded from the dataset. The use of extremely small- or large-scale factors in the scaling process of ground motions may distort the characteristic of strong ground motions. For this reason, the lower limit for the scaling of the ground motions to be used in the analyses was set as 0.5 and the upper limit as 4. Additionally, it has been observed that when the scale factor exceeds a value of 4, there is a significant increase in displacement demands from strong ground motions. These high displacement values exceed the physical capacity limits of the test setup detailed in Chapter 5. According to this limitation, strong ground motions with a scale factor greater than 4 were excluded from the scope of the study to ensure the safe execution of the experiments and to preserve the operational limits of the test setup. Ground motions with scale factors outside this range were not taken into consideration.

To enhance the reliability of both analytical and experimental results, an additional filtering process was conducted to eliminate pulse-type ground motions from the remaining set. This decision was based on the consideration that pulse-type records may not be compatible with testing systems employing hydraulic actuators, as the high velocity and displacement demands associated with such motions could exceed the stroke capacity and performance limits of the hydraulic actuators discussed in Chapter 5, potentially causing mechanical damage. To identify pulse-like characteristics in the records, the  $I_D$  index (shown in Equation 4.1), proposed by Manfredi (2001), was computed for all motions within the defined set.

$$I_D \cong 1.1t_d * \frac{PGA}{PGV} * \frac{\int_0^1 a^2(t) d\left(\frac{t}{t_d}\right)}{PGA^2} \quad (4.1)$$

According to López-Almansa et al. (2013), ground motions with an  $I_D$  index lower than 10 ( $I_D < 10$ ) can be classified as ordinary (non-pulsive) records. Based on this criterion, all records exhibiting an  $I_D$  index of 10 or greater were excluded from the dataset.

Following the filtering processes, the reference period intervals for scaling the strong ground motions have been determined. In determining these intervals, the theoretical natural vibration periods of the two different prototypes to be produced were taken as the basic parameters. Accordingly, considering the predicted 1-2 second natural vibration period of the first prototype, the first strong ground motion set was scaled to focus on this period band. Similarly, for the second prototype, in accordance with the targeted dynamic characteristics, the second ground motion set was scaled to the 3-4 second range. This selection aimed to observe the dynamic behavior and resonance effects of the devices under seismic inputs with frequency contents close to their own natural periods under the most critical conditions. Due to geometric and material-based variations that emerged during the final design and production stages of the isolators, the actual natural vibration periods of the prototypes showed partial deviations from the planned target ranges. However, despite these differences, the proximity of the obtained final period values to the reference ranges selected for scaling has been maintained; thus, the methodological consistency between the seismic input and the structural response has been preserved.

After determining target period ranges, the selected strong ground motions were scaled within these ranges, and the final set of records to be utilized in the study was determined based on this scaling procedure. For ground motions that satisfied the criteria mentioned above, records in both principal directions were compiled, and the corresponding acceleration response spectra were derived for each motion. Furthermore, the operational constraints of the testing equipment were taken into account during the selection process. In particular, the hydraulic actuators' displacement capacity ( $\pm 15$  cm) and maximum velocity capacity (250 mm/s) were considered to ensure the compatibility of the selected ground motions with the experimental setup discussed in detail in Chapter 5.

In this study, a spectrum scaling process was carried out to match the selected ground motions to the target spectrum. The reference spectrum is given in Figure 4.1 and the scaling process was carried out over the selected period ranges. For each ground motion record, elastic response spectrum was generated and scaled to be compatible

with the target spectrum. In the scaling process, the main criterion was to ensure that the spectral acceleration values obtained at the selected period intervals were not below the target spectrum. Thus, while preserving the dynamic characteristics of each ground motion, it is aimed to reach an amplitude level suitable for the target spectrum. Two distinct ground motion sets were employed in the study. The first set, referred to as GM Set-1, was derived by scaling the records within the period range of 1–2 seconds. The corresponding acceleration response spectra, together with the design spectrum obtained from this scaling procedure, are presented in Figure 4.2.

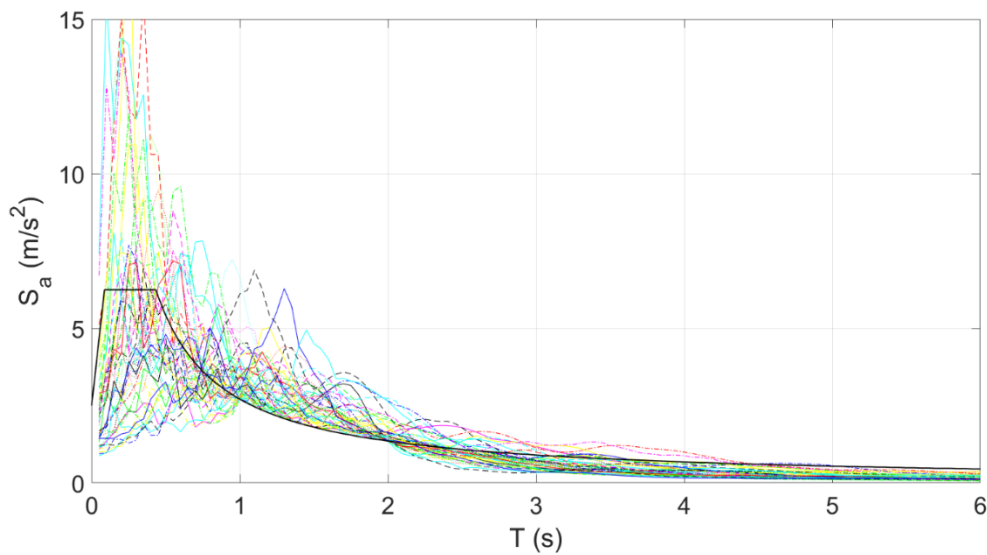


Figure 4.2 Acceleration spectra of scaled seismic ground motion records and design acceleration spectrum for GM Set-1

As a result of the scaling process, a total of 17 strong ground motion records that remained within the operational capacity of the experimental setup were selected, constituting the GM Set-1. This ground motion set was subsequently employed in the analytical study conducted to determine the geometry of the first prototype to be tested, as well as in the experimental investigations carried out on both the first and second prototypes. General information and seismic parameters of the strong ground motions in GM Set-1 are summarized in Table 4.1 and Table 4.2, respectively.

Table 4.1 General information about strong ground motions in GM Set-1

<b>Earthquake Code</b>	<b>Record Number</b>	<b>Earthquake Name</b>	<b>Component</b>	<b>Year</b>	<b>Mw</b>
<b>GM01</b>	RSN216	Livermore-01	STP093	1980	5.8
<b>GM02</b>	RSN1575	Chi-Chi, Taiwan	East	1999	7.62
<b>GM04</b>	RSN1266	Chi-Chi, Taiwan	North	1999	7.62
<b>GM05</b>	RSN1361	Chi-Chi, Taiwan	East	1999	7.62
<b>GM07</b>	RSN3273	Chi-Chi, Taiwan-06	North	1999	6.3
<b>GM08</b>	RSN4871	Chuetsu-oki, Japan	East-West	2007	6.8
<b>GM11</b>	RSN216	Livermore-01	STP183	1980	5.8
<b>GM14</b>	RSN1053	Northridge-01	PHP000	1994	6.69
<b>GM16</b>	RSN3867	Chi-Chi, Taiwan-06	West	1999	6.3
<b>GM18</b>	RSN3756	Landers	MVP090	1992	7.28
<b>GM19</b>	RSN358	Coalinga-01	SC4000	1983	6.36
<b>GM20</b>	RSN2498	Chi-Chi, Taiwan-03	East	1999	6.2
<b>GM22</b>	RSN4884	Chuetsu-oki, Japan	East-West	2007	6.8
<b>GM23</b>	RSN3273	Chi-Chi, Taiwan-06	West	1999	6.3
<b>GM28</b>	RSN347	Coalinga-01	Z09000	1983	6.36
<b>GM29</b>	RSN356	Coalinga-01	SC2090	1983	6.36
<b>GM30</b>	RSN3274	Chi-Chi, Taiwan-06	North	1999	6.3

Table 4.2 Seismic parameters of selected strong ground motions in GM Set-1

<b>Earthquake Code</b>	<b>D<sub>5-95</sub> (sec)</b>	<b>Fault Mechanism</b>	<b>R<sub>jb</sub> (km)</b>	<b>R<sub>rup</sub> (km)</b>	<b>V<sub>s,30</sub> (m/s)</b>
<b>GM01</b>	20.2	Strike Slip	53.4	53.8	650
<b>GM02</b>	39.1	Reverse, Oblique	50.5	54.3	528
<b>GM04</b>	21	Reverse, Oblique	47.0	51.1	453
<b>GM05</b>	40.4	Reverse Oblique	72.2	74.5	373
<b>GM07</b>	17.6	Reverse	43.5	44.7	379
<b>GM08</b>	18.9	Reverse	38.0	41.8	425
<b>GM11</b>	20.2	Strike Slip	53.4	53.8	650
<b>GM14</b>	18	Reverse	41.4	41.7	552
<b>GM16</b>	17.5	Reverse	47.4	48.4	539
<b>GM18</b>	32.9	Strike Slip	40.7	40.7	368
<b>GM19</b>	15	Reverse	30.3	31.6	492
<b>GM20</b>	11.1	Reverse	49.7	50.1	665
<b>GM22</b>	31.1	Reverse	37.8	41.6	551
<b>GM23</b>	17.6	Reverse	43.5	44.7	379
<b>GM28</b>	19.9	Reverse	30.4	31.7	372
<b>GM29</b>	18.9	Reverse	35.3	36.4	566
<b>GM30</b>	13.2	Reverse	40.4	41.6	573

Particular attention was given to ensuring that the strong ground motions included in GM Set-1 did not exceed the displacement and velocity capacities of the experimental setup. Accordingly, the selection criteria required that the peak ground displacement (PGD) of each record be less than 0.15 m and the peak ground velocity (PGV) be less than 0.25 m/s. The scale factors, along with the PGD, PGV, and peak ground acceleration (PGA) values of the selected motions, are presented in Table 4.3.

Table 4.3 Characteristic properties of scaled strong ground motions in GM Set-1

<b>Earthquake Code</b>	<b>Scale Factor</b>	<b>PGD (m)</b>	<b>PGV (m/s)</b>	<b>PGA (m/s<sup>2</sup>)</b>
<b>GM01</b>	2.964	0.060	0.197	1.417
<b>GM02</b>	2.113	0.148	0.198	0.924
<b>GM04</b>	1.433	0.138	0.205	1.010
<b>GM05</b>	1.611	0.120	0.206	0.865
<b>GM07</b>	1.445	0.082	0.217	1.408
<b>GM08</b>	2.034	0.068	0.219	2.527
<b>GM11</b>	3.298	0.057	0.221	2.552
<b>GM14</b>	3.039	0.056	0.225	1.831
<b>GM16</b>	2.117	0.057	0.227	2.439
<b>GM18</b>	1.174	0.075	0.236	1.621
<b>GM19</b>	3.010	0.082	0.237	2.130
<b>GM20</b>	3.191	0.146	0.237	1.848
<b>GM22</b>	1.194	0.056	0.239	1.424
<b>GM23</b>	1.857	0.091	0.240	1.827
<b>GM28</b>	2.127	0.074	0.244	1.031
<b>GM29</b>	3.301	0.047	0.246	2.899
<b>GM30</b>	1.506	0.079	0.248	2.413

The second ground motion set employed in the study, referred to as GM Set-2, was obtained by scaling the records within the period range of 3–4 seconds. Figure 4.3 illustrates the acceleration response spectra and the design spectrum used in the selection of this set.

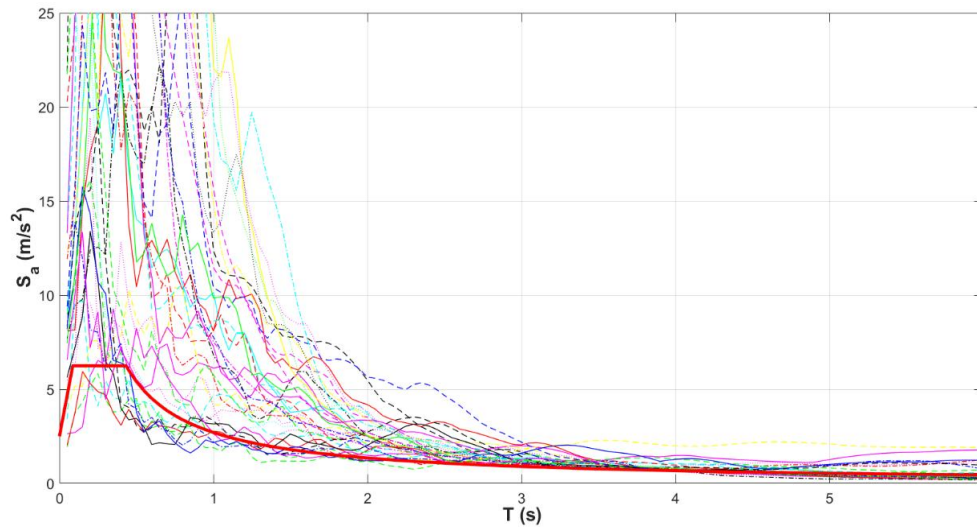


Figure 4.3 Acceleration spectra of scaled seismic ground motion records and design acceleration spectrum for GM Set-2

The scaling procedure resulted in the selection of seven strong ground motion records that remained within the operational limits of the experimental setup to form the GM Set-2. This set was specifically developed to account for the relatively long fundamental period of the second prototype of the parabolic isolator. It was subsequently employed in the experimental program conducted on this prototype. The general information and seismic parameters of the strong ground motions comprising GM Set-2 are provided in Table 4.4 and Table 4.5, respectively.

Table 4.4 General information about strong ground motions in GM Set-2

<b>Earthquake Code</b>	<b>Record Sequence Number</b>	<b>Earthquake Name</b>	<b>Direction</b>	<b>Year</b>	<b>Mw</b>
<b>GM1</b>	RSN1219	Chi-Chi, Taiwan	North	1999	7.62
<b>GM2</b>	RSN1762	Hector Mine	ABY090	1999	7.13
<b>GM3</b>	RSN5465	Iwate, Japan	East-West	2008	6.9
<b>GM4</b>	RSN5472	Iwate, Japan	East-West	2008	6.9
<b>GM5</b>	RSN5668	Iwate, Japan	East-West	2008	6.9
<b>GM6</b>	RSN5799	Iwate, Japan	East-West	2008	6.9
<b>GM7</b>	RSN5799	Iwate, Japan	North-South	2008	6.9

Table 4.5 Seismic parameters of selected strong ground motions in GM Set-2

<b>Earthquake Code</b>	<b>D<sub>5-95</sub> (sec)</b>	<b>Fault Mechanism</b>	<b>R<sub>jb</sub> (km)</b>	<b>R<sub>rup</sub> (km)</b>	<b>V<sub>s,30</sub> (m/s)</b>
<b>GM1</b>	34.3	Reverse	56.9	57.5	603
<b>GM2</b>	26.7	Strike Slip	41.8	43.1	383
<b>GM3</b>	76.9	Reverse	90.5	91.4	425
<b>GM4</b>	23.4	Reverse	31.4	33.8	643
<b>GM5</b>	59.1	Reverse	43.2	43.2	540
<b>GM6</b>	20.3	Reverse	39.9	41.7	552
<b>GM7</b>	20.3	Reverse	39.9	41.7	552

In the development of the second ground motion set (GM Set-2), a multi-parameter selection strategy was employed, according to the physical constraints of the experimental apparatus and the study's objectives. The principal factors governing this selection procedure included the displacement and load capacity of the shake table, the defining characteristics of the records, scaling factor not exceeding the top limit of 4, and the specified period range. The necessity to achieve spectral matching within the specified long period range of 3 to 4 seconds, along with additional strict filtering criteria, considerably restricted the availability of robust ground motions appropriate for the investigation in the current datasets. Owing to this constraint in the database, a necessary method was implemented to maintain the integrity of the dataset. To determine the ground motions labeled GM3, GM4, GM5, GM6, and GM7, it was necessary to employ multiple station recordings from the same seismic event. Consequently, GM Set-2 comprises a restricted quantity of events. A significant number of earthquake records pertain to the Iwate, Japan earthquake for the reasons explained above.

Seven different strong ground motions were identified using criteria similar to those used for GM Set-1. General information about these identified strong ground motions is provided in Table 4.6.

Table 4.6 Characteristic properties of scaled strong ground motions in GM Set-2

<b>Earthquake Code</b>	<b>Scale Factor</b>	<b>PGD (m)</b>	<b>PGV (m/s)</b>	<b>PGA (m/s<sup>2</sup>)</b>
<b>GM1</b>	4.247	0.081	0.218	2.087
<b>GM2</b>	0.728	0.099	0.201	1.300
<b>GM3</b>	3.016	0.104	0.154	1.951
<b>GM4</b>	2.099	0.126	0.212	2.852
<b>GM5</b>	2.066	0.144	0.202	2.315
<b>GM6</b>	1.940	0.133	0.237	3.140
<b>GM7</b>	1.558	0.110	0.195	3.089

As a result of the study, two distinct sets of strong ground motions, each scaled to a different period range, were developed. GM Set-1 was employed both in the analytical study and in experimental investigations conducted on the two prototypes. However, GM Set-2 was only used in the tests of the second prototype. During the selection process of these strong ground motion sets, the target period ranges were strategically determined to be compatible with the natural vibration periods of the designed prototypes. This ensured that the spectral acceleration values of ground motions were concentrated in the critical frequency bands where the seismic performance of the isolators could be most clearly observed. Two distinct sets of strong ground motions, whose selection criteria and applications were outlined above, were established. All subsequent stages of the study were conducted using these two ground motion sets.

## CHAPTER 5

### INTRODUCTION OF TEST SETUP AND INSTRUMENTATION

#### 5.1 Test Setup

A test setup was designed to meet the experimental requirements to carry out the floor isolator tests. Accordingly, it was decided to manufacture a uniaxial shake table in order to test the floor isolator. This shake table is placed in the METU Structural Mechanics Laboratory, where the tests are carried out. A hydraulic actuator available in the laboratory inventory is used for horizontal movements. The hydraulic actuator, which has a horizontal force capacity of 50 kN, fully meets the needs of the study with its ability to apply a real-time dynamic effect. The hydraulic actuator has a displacement capacity of  $\pm 150$  mm horizontally. The capacity of the hydraulic system and the hydraulic actuator was effective in selecting the strong ground motions, which is discussed in Chapter 4.

The final geometry and structural components of the experimental setup were achieved through the systematic implementation of three steps. The work carried out in these steps is discussed in detail in the following sections.

##### 5.1.1 Determination of Experimental Setup Requirements

The maximum loads to be applied were first identified to guide the design of the experimental setup. Key parameters, including the horizontal force capacity of the actuator, loading rates, and displacement amplitudes, were determined. Preliminary assessments conducted at the Structural Mechanics Laboratory of Middle East Technical University (METU) indicated that the hydraulic actuator has a force capacity of 50 kN. Therefore, it is assumed that the maximum load affecting the shaking table will be 50 kN. In addition to horizontal load analyses determining the

seismic performance of the system, comprehensive research was also conducted to determine the vertical load capacity that will affect the isolator. During this process, the standard weights and operational loads of equipment such as server racks and electrical cabinets, in which the designed floor isolator can be used, were examined in detail. As a result of this, it was determined that the nominal vertical load per device would be approximately 1 ton (10 kN). To simulate this weight during testing, steel masses from the laboratory's inventory were utilized, each weighing 2 kN. By stacking five such units, a total design weight of 10 kN (equivalent to 1 ton) was achieved. Finally, the maximum horizontal displacement of the hydraulic actuator was also determined at this stage. As a result of the work carried out, the maximum horizontal displacement of the hydraulic actuator was determined to be  $\pm 150$  mm. These specifications served as the basis for defining the loading scenarios applied to the shaking table and its components, as well as for evaluating their structural response under test conditions.

Another issue to be considered is the geometrical requirements of the shake table. The dimensions of hydraulic actuator and of the floor isolator devices to be mounted on the shake table are important factors determining these parameters. Within the scope of the project, 4 units of isolators have been produced, and it is planned to bring the produced isolators together by means of a modular platform. In other words, the floor isolator system is aimed at being in a geometry where 4 isolator devices work together by means of a platform. The dimensions of this platform were decided to be 1000x1000 mm, taking into account the dimensions of the equipment to be carried. A more detailed discussion on the selection of dimensions of the isolated slab is provided in Chapter 5.1.3.

The length of the hydraulic actuator to be used in the tests and in the laboratory inventory is 2000 mm. The hydraulic actuator was mounted to the strong wall in the laboratory from its fixed end with a connection apparatus designed and manufactured within the scope of this study and the necessary anchorage will be provided. According to the geometry of the experimental setup, the centre of the hydraulic actuator was designed to be 82 mm above the laboratory floor. The assembly was

completed by mounting the hydraulic actuator on the shake table supported by frictionless linear guide that allow frictionless movement in one direction. A schematic representation of the experimental setup with the hydraulic actuator and strong wall connection is presented in Figure 5.1. An overview of the overall CAD model of the experimental setup consisting of hydraulic actuator anchorage, shake table, modular platform and safety frame is given in Figure 5.2.

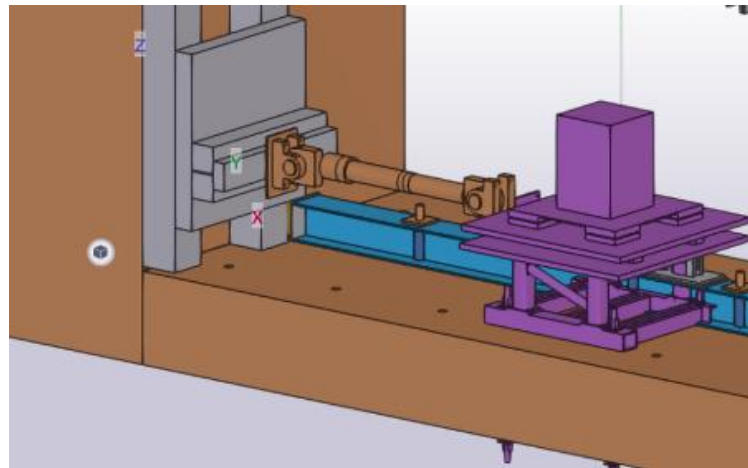


Figure 5.1 Schematic representation of the elements that make up the experimental setup.

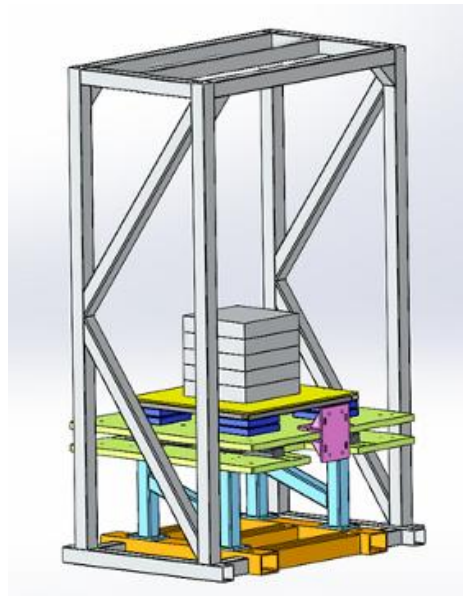


Figure 5.2 CAD Model of the experimental setup consisting of support legs, shake table, modular platform, and the safety frame.

### 5.1.2 Design of Test Setup

The experimental setup was designed to resist both static and dynamic effects. To evaluate the reliability and strength of the design, finite element analyses were conducted using ANSYS (2023). In these analyses, the most adverse loading scenarios were considered by assuming that the linear trolleys, which are located under shake table and enable frictionless movement in one direction, remain fixed. Under this assumption, the analyses were performed with the load fully transmitted to the bearings. This condition was regarded as the most unfavorable scenario for the experimental setup, as the immobilization of the trolleys would subject the bearings to the applied load. The maximum force capacity of the hydraulic actuator to be used in the experimental setup was declared as 50 kN by the manufacturer and during the analyses, this force was applied horizontally to the numerical model in two different cases as both pull and push from the hydraulic actuator fastener. The effect that creates the highest stress between this pulling and pushing force is taken into consideration. In addition, the effects of the payload to be placed on the isolated slab were also taken into account. A load of 14 kN, which is 1.4 times the payload above the isolator, was applied to the system in the vertical direction. The application of this load to the system was done to determine how the experimental setup would perform under such loads in general. During the application of this load to the system, the stresses and deformations to which the system would be subjected were analysed in detail.

The maximum stress values obtained from the analyses were compared with the safety stress values obtained by dividing the strength of the materials from which the elements of the experimental setup are made by the safety factors according to the Allowable Stress Limit (ASD). By examining the maximum stress values obtained as a result of the analyses, it was determined that the experimental setup is sufficiently resistant to both static and dynamic effects and can operate safely under the prescribed load conditions. After designing and manufacturing process, the assembled shake table in the laboratory is shown in Figure 5.3.



Figure 5.3 Shaking table which installed in the laboratory

### 5.1.3 Design and Finite Element Analysis of Isolated Slab

The planned floor isolator consists of a system in which four devices operate together on a modular platform. The final design aims to ensure that this modular platform can be easily combined with other modules. This maximizes field applicability and facilitates the integration of modular systems. The modular structure of the system provides flexibility in different application areas, enabling the provision of customized solutions according to user needs.

The dimensions of the modular platform were determined as 1000x1000 mm, taking into account the isolator dimensions and the requirements of the loads to be carried. Three main factors were prioritized in determining these dimensions. Firstly, the four isolators to be placed under the modular platform should not extend outward from the platform and should be securely connected to the isolators. This is a critical element to ensure the effectiveness and stability of the isolators. Secondly, the modular platform's ability to support the axial load generated by the equipment to be installed was considered. It is essential that the frame does not experience any collapse in the static state or under dynamic effects and can serve continuously. In this context, the durability of the modular platform on the isolator has been analyzed under both static and dynamic loads. Third and lastly, the frame structure should be modular and should be able to be easily connected with other modules. This feature also provides significant advantages in system expandability and maintenance processes. Considering these three basic elements, it was decided to design the frame on the isolator as 1000x1000 mm. Moreover, the choice of these dimensions allows the system to be flexible and adaptable in various application scenarios. CAD drawings of the isolated slab are presented in Figure 5.4.

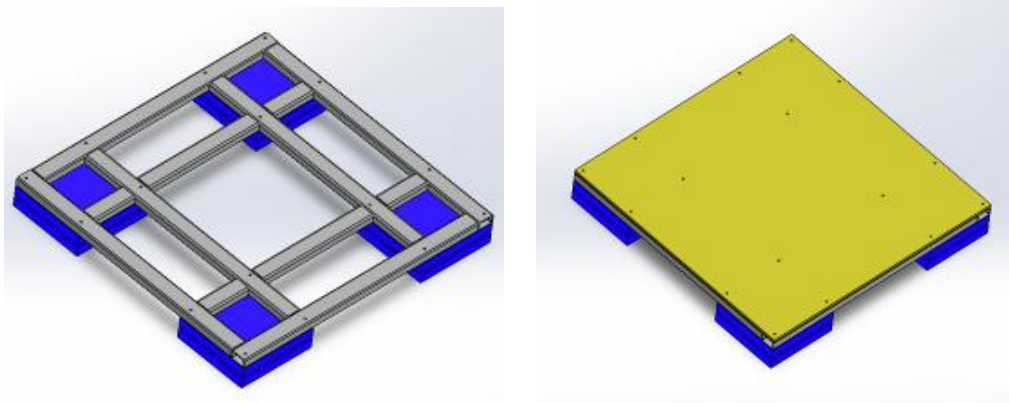


Figure 5.4 CAD drawings of modular platform (isolated slab).

The modular platform is designed as a square plate geometry with each side of 1000 mm. Each edge of this square is formed by box profiles. In order to provide the connection between the inner corners of the isolator and the frame, 60x60x4 mm box profiles in S355 steel were used on the opposite edges of the isolator, coinciding with

the inner edges of the isolator, and a steel grid was obtained. This structure ensures the stability of the isolators and their integration with the platform. Moreover, it is planned to use a 1 cm thick steel plate to place the load or device on this modular platform. This steel plate will ensure that the load is evenly distributed and structural integrity is maintained.

Static analyses of the modular platform were performed in finite element analysis software. The maximum stress values obtained from the analyses were compared with the safety stress values obtained by dividing the strength of the materials from which the elements of the experimental setup are made by the safety factors according to the Allowable Stress Limit (ASD). By examining the maximum stress values obtained as a result of the analyses, it was determined that the modular platform is sufficiently resistant to both static and dynamic effects and can operate safely under the prescribed load conditions. After designing and manufacturing process, the final form of the isolated slab is shown in Figure 5.5.



Figure 5.5 The installed isolated slab in the laboratory

## 5.2 Instrumentation and Data Calibration Process

Obtaining reliable data during the experiment is of critical importance, as the accuracy of the experimental results depends directly on the performance of the data acquisition system. In this context, an accelerometer-based measurement system was integrated into the experimental setup. The configuration and details of this measurement system are presented in the following sections.

The measuring instruments used in experimental studies are of great importance for the accuracy and reliability of the obtained data. In this context, two types of measuring instruments stand out in particular: potentiometers (LVDT - Linear Voltage Displacement Transducer) and accelerometers. Potentiometers are the first type of measuring instruments preferred for displacement measurement. The position of the potentiometers used during the experiments is shown in Figure 5.6. These devices measure the displacement value over the potential difference depending on the resistance change. The data provided by potentiometers are highly accurate and produce reliable results. Therefore, they are widely used in various engineering and physics experiments. The simple structure of potentiometers and the principle of measurement based on the direct relationship between displacement and potential difference make them an ideal device especially for monitoring linear motions. However, these devices may not provide sufficient accuracy in experimental setups where dynamic effects, in other words, rapid motion changes are observed. In this respect, it is considered that measurements made only by using potentiometers may be insufficient in dynamic experiments to be carried out within the scope of the study.

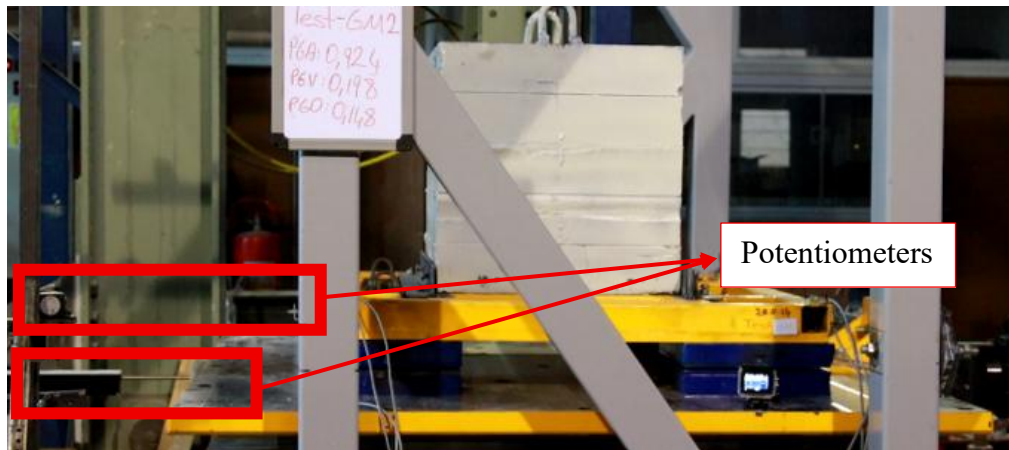


Figure 5.6 The position of the potentiometers used during the experiments

Accelerometers, as the second type of measuring device, are capable of providing more complex and multidimensional data than potentiometers. Accelerometers are designed to measure the acceleration of a body and can track motion, usually in three orthogonal axes ( $x$ ,  $y$ ,  $z$ ). The data obtained from accelerometers is referred to as raw data and needs to be processed before it can be analyzed. Processing raw data is considered a critical step to improve the accuracy of the acceleration detected by the device and to reduce noise in the environment where the device is measuring. Raw data processing involves various filtering and correction techniques. These techniques have been developed with the aim of optimizing the sensitivity and accuracy of the accelerometer. However, the accuracy of the processed data needs to be checked. This step is necessary to verify whether the data obtained from the accelerometer are in agreement with the experimental findings.

Although potentiometers and accelerometers are the basic measurement devices frequently used in experimental research, the application areas, advantages and limitations of both devices are different. Therefore, the selection of the right instrument and the correct processing of the data obtained is critical factors for the success of the experiments. Considering the fact that the experiments carried out within the scope of the project are based on dynamic motion, the displacement capacities of the prototype devices and the number of existing potentiometer (LVDT) devices in the inventory of METU Structural Mechanics Laboratory, it was seen that

these devices would be insufficient in terms of capacity and quantity. For this reason, it was decided to install an accelerometer-based measurement system. In the first verification of the installed system, it is planned to carry out verification studies with potentiometers available in the laboratory inventory and to verify the analytically obtained displacement data within the scope of this study.

For the reasons mentioned above, the design of a device to record the response of the isolated slab system with accelerometers was initiated. In this context, it was decided to place 3 accelerometers, each of which can receive data from three different principal directions, at each corner of the isolated slab. Thus, it is aimed to obtain motion data in x, y and z (both horizontal and vertical directions) axes from each corner of the platform. With this positioning, accelerations that may occur in different axes at each corner of the platform will be monitored separately. In total, 12 accelerometers will be used in the isolated slab with 3 accelerometers at each of the four corners. By analytical processing of the obtained data, it will also be possible to obtain velocity and displacement data in three principal directions at each corner of the isolated slab.

In addition to the isolated slab, it is also planned to install an accelerometer on a shake table in order to analyze the dynamic movements of the experiment in more detail. This accelerometer placed on the shake table will enable direct measurement of the dynamic effect generated by the hydraulic actuator. In this way, acceleration data of both the isolated slab and the shake table will be collected simultaneously and a more comprehensive analysis will be possible. At the same time, the displacement data sent by the control system during the dynamic effect on the hydraulic actuator will be verified. As explained above, a total of 13 accelerometers will be used for this setup, and the layout plan of these accelerometers is shown in the 3D CAD drawing in Figure 5.7.

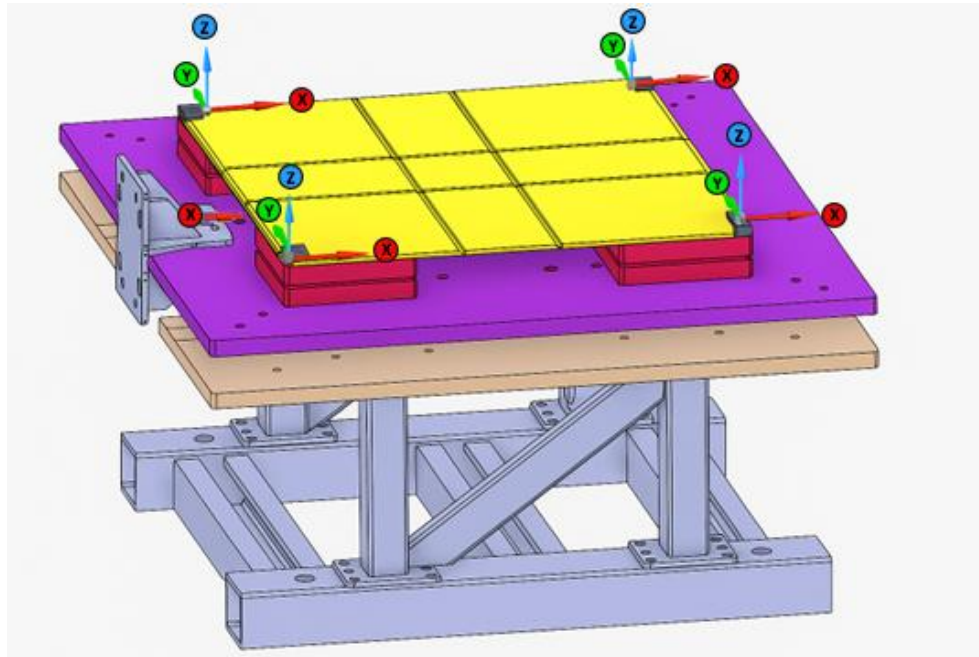


Figure 5.7 Test measurement system layout.

Figure 5.7 shows the locations of a total of 13 accelerometers used during the experiment. Three of these accelerometers are uniaxial devices available in the laboratory inventory and the verification processes have been completed. The remaining ten accelerometers were manufactured in the laboratory using ADXL335-5V type sensors. The main technical specifications of these sensors are summarized in Table 5.1.

Table 5.1 Technical specifications of accelerometers used in the measurement system

<b>Input Voltage</b>	5 – 5.5 V
<b>Measurement Range</b>	$\pm 3g$
<b>Sensitivity</b>	330 mV/g
<b>Operating Current</b>	0.5 mA

All wired and ready-to-use devices were connected to a 16-channel 24-bit ADC digitizer (data acquisition system) unit available in the laboratory inventory. From this data acquisition system, data will be received simultaneously from all channels to which the measuring devices are connected during the experiments.

After the manufacturing and wiring were completed, a verification study was carried out to verify that the accelerometers produced in the laboratory environment were accurately recorded. With the same verification study, it was also checked that the data obtained from the data acquisition system could be received accurately. One of the accelerometers in the laboratory inventory was placed at the center point of the modular platform in the direction of the experiment (coincident with the hydraulic actuator motion axis) and 10 devices prepared by the project team were fixed one by one next to this device as shown in Figure 5.8. After each device was fixed, a harmonic effect of certain amplitude and frequency was given by means of the hydraulic actuator, and acceleration recordings were taken. The data obtained from the branded accelerometer and the accelerometers prepared by the laboratory team were compared and it was determined that the records were consistent. At this stage, in addition to the raw acceleration data, the velocity and displacement data obtained from this data were also compared. The basic comparison was carried out by plotting and comparing the data obtained on top of each other. As a result of this study, it was ensured that the manufactured accelerometers operate with sufficient accuracy and precision.



Figure 5.8 Mounting the accelerometers manufactured in the laboratory side by side to compare the measurements of branded accelerometers.

After the installation of the accelerometers was completed, preliminary data collection started. Firstly, data were collected to test the system with various harmonic effects and randomly selected strong ground motion records. In the first measurements, the behavior of the conical surface sample or what kind of harmonic / ground motion effect was given was not examined and the focus was on examining the data obtained. In order to confirm the accuracy of the data collected with accelerometers, displacement measurements were also taken from these experiments using 3 potentiometers (LVDT) available in the inventory of METU Structural Mechanics Laboratory. One potentiometer was placed on the shake table concentrically from the hydraulic actuator axis and the other two potentiometers were attached to both corners of the isolated slab. It was possible to compare the data obtained from the first potentiometer with the displacement data derived from the data obtained from the accelerometer presented in Figure 5.9, which measures the dynamic effect generated by the hydraulic actuator.



Figure 5.9 The accelerometer fixed directly on the hydraulic actuator connecting piece on the direction of excitation.

With the displacement data given by the other two potentiometers, the displacement data derived from the acceleration measured at the corners where they were placed were verified. The visualization of these potentiometers mounted together with the accelerometers is presented in Figure 5.10.



Figure 5.10 Potentiometers and accelerometers are placed on both corners of the isolated slab for acceleration data verification.

An example of the raw acceleration data obtained from the dynamic effects applied with the hydraulic actuator is presented in Figure 5.11. As can be seen from the acceleration record, it is naturally determined that there is a significant amount of noise in the data. When Fourier transformation is applied to the obtained acceleration data in MATLAB (2024) environment, it is determined that there are frequency foci with high amplitudes below 0.25 Hz and above 30 Hz. While the amplitudes above 30 Hz appear in the recording as noise from sources such as mains voltage (50 Hz) (Figure 5.11, last 15 seconds), the source of low frequency unwanted amplitudes could not be detected. Since the frequency content of the effects (harmonics, ground motion, etc.) applied during the recordings is above 0.25 Hz, it is considered that there is no data from dynamic effects. It is concluded that this artifact, which is thought to be caused by the measurement/data collection system, should be filtered from the data obtained.

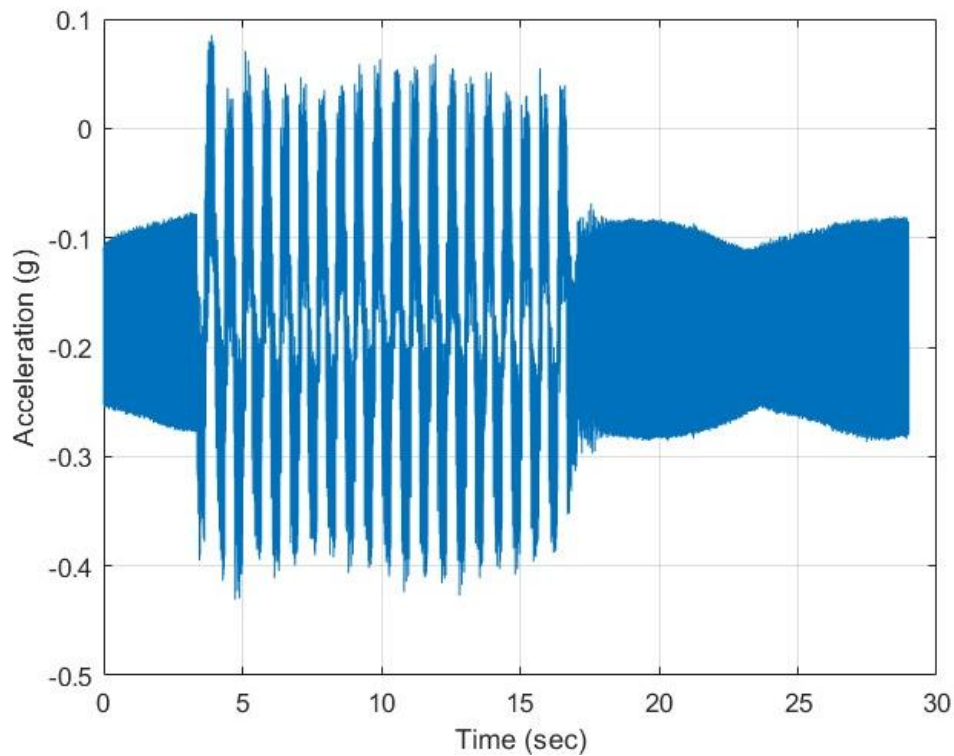


Figure 5.11 Raw acceleration data from one of the accelerometers under dynamic action.

As discussed above, it was decided to apply a filtering process to the acceleration data in order to reduce the noise in the raw acceleration data and to derive velocity and displacement data properly from acceleration data. In order to minimize the effect of unwanted amplitudes at the frequencies discussed, a bandpass filter was applied to all acceleration records. For this purpose, a routine was prepared in MATLAB (2024) to apply a fourth-order Butterworth filter to all of the raw acceleration data from 13 channels (4 corners of the isolated slab and a shake table). In addition, de-offsetting and de-trending were applied to the acceleration records by using the MATLAB (2024) signal processing library to minimize offsets and trends in the signals. By using the filtered and processed acceleration records, numerical integration was applied at a time interval ( $dt = 0.005$  s) compatible with the 200 Hz sampling rate at which measurements were taken, and velocity and displacement data were derived, respectively. In order to eliminate offsets and trends that may

occur in the derived velocity and displacement data, the de-offsetting and de-trending procedures were also applied. This entire procedure was written as a post-processing MATLAB (2024) code routine and a scripting tool was obtained to be used in the data to be obtained from all experiments.

As a result of these procedures, Figure 5.12 presents a comparison between the displacement response derived from the processed acceleration data at the corner and the raw displacement measurements directly obtained from the potentiometer under the excitation of a random strong ground motion. As can be seen in Figure 5.12, the displacement data derived from the accelerometer and the displacement data obtained from the potentiometer match to a large extent. In general, it is observed that there are deviations in the displacement data obtained from the accelerometer in low amplitude regions due to the error in the numerical integration and data processing steps, as observed in Figure 5.12. However, in the regions where the amplitude of the response is high, the matching is found to be largely compatible.

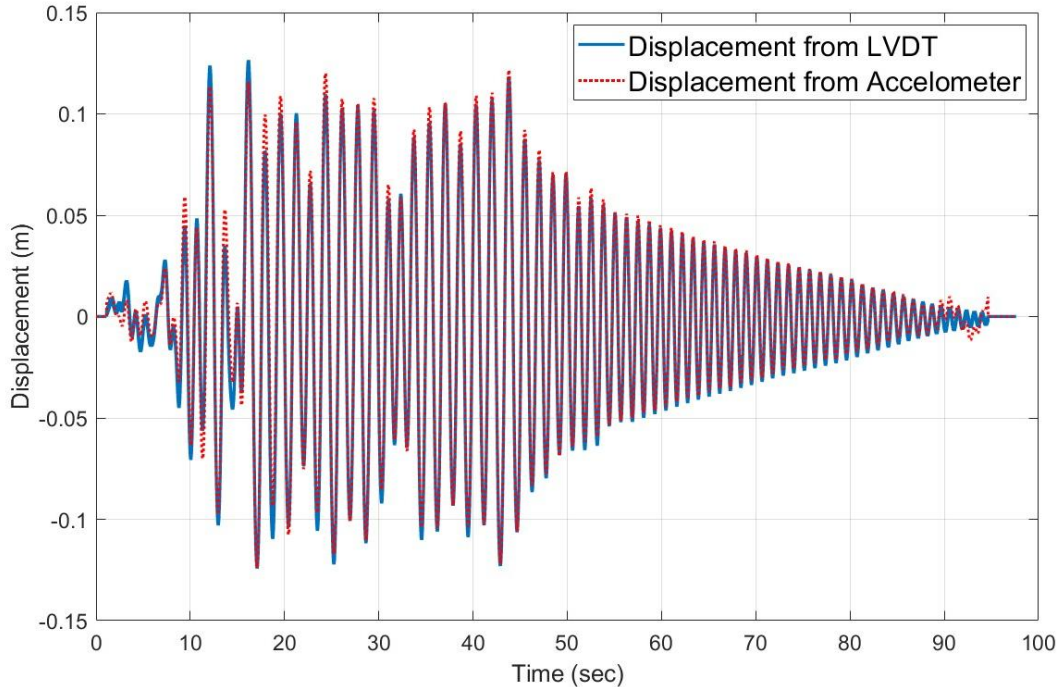


Figure 5.12 Comparison of displacement data derived from calibrated and processed accelerometer data and raw displacement data from the potentiometer.

At this stage of the study, a comparison between the accelerometer data and the potentiometer measurements confirmed that the processed accelerometer data provided sufficiently accurate results. Thus, the calibration and verification study was completed. Within the scope of this study, the preparation processes of the post-processing MATLAB (2024) routines to be used in the compilation of the data to be obtained in the experiments were also completed.

### **5.3 Discussion about the Test Setup and Instrumentation**

The experimental setup presented in this section was designed to reliably determine the mechanical and dynamic properties of the rolling-based parabolic-surface floor isolator (RPFI), taking into account both the expectations derived from analytical studies and the existing laboratory constraints. The fundamental constraints of the experimental system are defined as the maximum stroke and speed capacity of the hydraulic actuator, the limits of the vertical load that can be applied, measurement accuracy, and safety requirements. Within these constraints, the isolated slab, the support legs, and the safety frame were considered together to create a modular and rigid test platform. This aims to observe the isolator behavior independently of any flexibility or boundary condition effects arising from the test setup.

The experiments were conducted using a single-axis hydraulic shaking table. This situation creates a limitation in that the system cannot directly represent multi-axis earthquake effects. However, since the main objective of this study is to determine the isolator's rolling behavior, recall mechanisms, and damping characteristics primarily in the horizontal direction, the single-axis effect provides sufficient representation for this purpose. Furthermore, since the dominant dynamic behavior of rolling-based isolators occurs in the horizontal plane, it is possible to reliably determine the system's fundamental stiffness, damping, and acceleration reduction characteristics using single-direction shaking.

The structural safety and rigidity of the designed test setup were analyzed using the finite element method in the ANSYS (2023) environment prior to the experiments. The isolated floor, safety frame, and connection elements were evaluated under maximum anticipated vertical loads, maximum horizontal forces, and dynamic effects, demonstrating that the system operates safely within its elastic limits. These analyses enabled the elimination of any potential stability issues that could arise during the experiment.

The measurement system is based on a structure that uses accelerometers and potentiometers together to determine the dynamic response of the isolator with high accuracy. Accelerometers directly measure the accelerations transmitted to the isolated floor, enabling the determination of acceleration reduction ratios, which are the fundamental performance indicators of the isolator. However, displacements obtained through double integration of acceleration data may be susceptible to errors caused by drift and filtering, especially in low-frequency movements. Therefore, potentiometers that directly measure displacement were used in the system to independently verify the displacement data derived from acceleration. By comparing the two measurement systems, the signal processing steps were calibrated, and measurement reliability was increased.

In conclusion, the experimental setup and instrumentation system described in this section provide an adequate experimental environment for reliably and reproducibly determining the stiffness, damping, displacement capacity, and acceleration reduction performance of the parabolic surface plate isolator. Despite the limitation of a single-axis shaking table, it is evident that the fundamental dynamic characteristics of the system can be accurately captured and that the analytical model can be validated.

## CHAPTER 6

### DYNAMIC TESTS AND RESULTS

#### 6.1 Production of Prototypes

Two different prototypes were produced within the scope of this study. The parabolic surface equations of these prototypes are  $z = 0.48x^2$  and  $z = 0.192x^2$ . Details regarding the production process and specifications of the prototypes are discussed in this section.

The surface of the first device prototype designed and tested within the scope of this study is based on the analytical study discussed in Chapter 3. The vertical coordinate of this prototype, designed according to the equation  $z = 0.48x^2$ , is shown in Figure 6.1. In accordance with its dimensions and design requirements, a 3D model of the RPFI was created, and a CAM model was prepared. Using the prepared CAM model, the sliding surfaces of the isolator support plates were machined with vertical lathes according to the specified parabolic equation. The CAD drawings of the manufactured rolling-type parabolic-surface floor isolator (RPFI) are given in Figure 6.1.

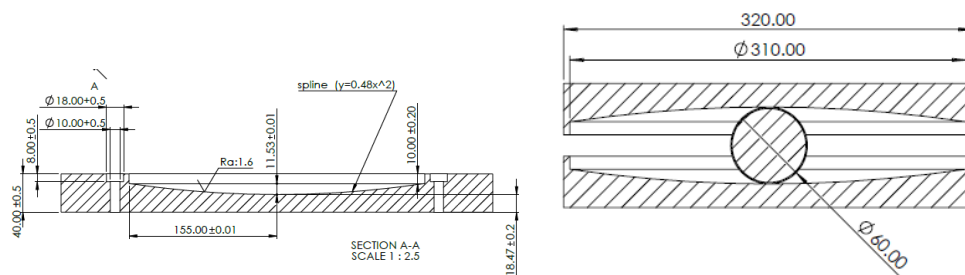


Figure 6.1 Technical drawings of the first prototype of the RPFI

The completed production of the first RPF1, whose production drawings are given in Figure 6.1, and its modular form attached to the shaking table are shown in Figure 6.2.



Figure 6.2 Image of the first prototype of the RPF1

The second prototype with a parabolic surface  $z=0.192x^2$  was produced by reworking the isolator surface of the first prototype, which was tested and had a surface equation  $y = 0.48x^2$ . The technical drawing and manufactured support plate for the second prototype of the RPF1 are shown in Figure 6.3.

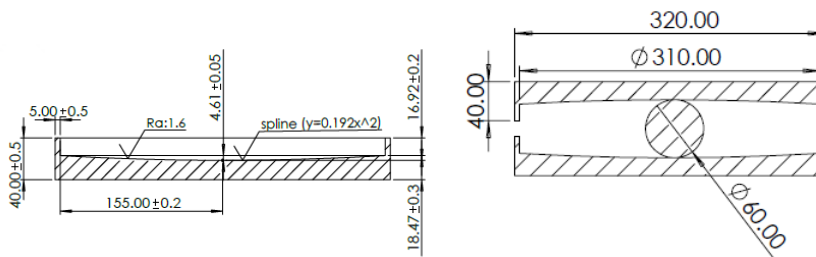


Figure 6.3 Technical drawings of the second prototype of a RPF1

The production of the second RPF1, whose production drawings are shown in Figure 6.3, has been completed and its attached state to the shaking table is shown in Figure 6.4.

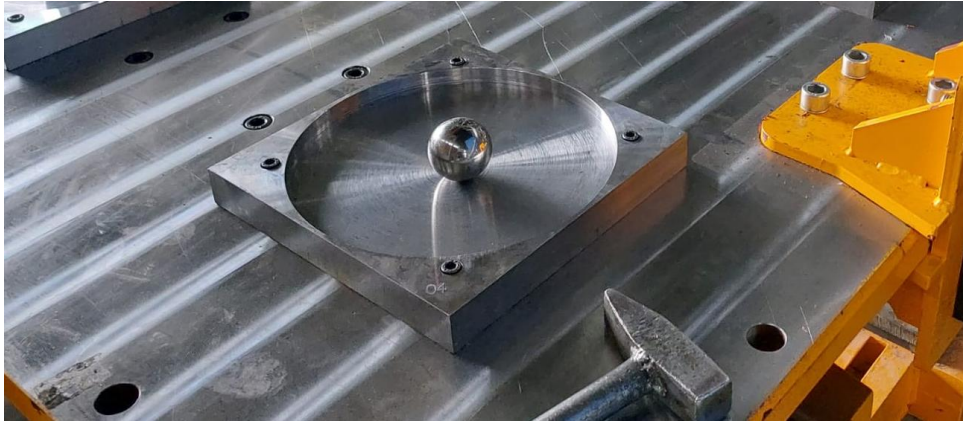


Figure 6.4 Images of the second prototype of the RPF

Production drawings for the RPF to be used in the experiment have been discussed. Based on these drawings, prototypes required for testing have been produced. The appearance of the produced prototypes is shown in Figure 6.2 and Figure 6.4. Using these prototypes, experimental studies were conducted to determine the dynamic characteristics of the devices and are discussed in the following sections.

## 6.2 Introduction of Tests

Tests for the first prototype, which has a parabolic surface defined as  $z = 0.48x^2$ , were carried out on 24–25 December 2025 at the METU Structural Mechanics Laboratory. Four different type experiments were performed on this prototype. The flowchart for these experiments is shown in Figure 6.5.

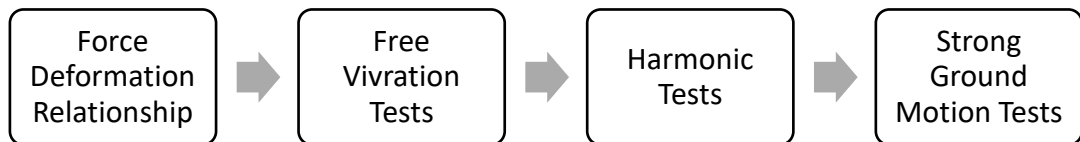


Figure 6.5 Flowchart showing dynamic tests

The first set of tests aimed to characterize the hysteretic behavior of the device. In these tests, the horizontal movement of the isolated slab was restricted, and harmonic

excitations were applied through the shaking table to obtain the force–deformation response of the isolator. The second experiment consisted of free-vibration testing. For this purpose, the isolated slab of the isolator was displaced to its maximum allowable deformation and released, allowing the free-vibration response to be recorded. Based on the measured free-vibration data, the damping ratio and friction coefficient of the device were calculated. The third experiment involved harmonic loading tests, in which harmonic excitations with various frequencies were applied through the shaking table to examine the dynamic behavior of the isolator. The fourth type of test was the strong ground motion experiment. Using GM Set-1 defined in Chapter 4, the acceleration reduction performance of the first prototype was evaluated.

The second prototype, featuring a parabolic surface defined as  $z = 0.192x^2$ , was tested between 9–16 April 2025 in the METU Structural Mechanics Laboratory. A similar testing procedure was followed for this prototype. Sequentially, the hysteresis test, free-vibration test, and harmonic loading test were conducted in the same manner as for the first prototype. However, in the strong ground motion experiment, two different GM sets were used, namely GM Set-1 and GM Set-2 provided in Chapter 4. The reason for employing two different strong ground motion sets is discussed in Chapter 4.

A general overview of the experimental protocols applied to each prototype has been presented above. Detailed descriptions of each experiment are provided in the corresponding sections of the following chapters. The results obtained for each prototype have been compiled and discussed in later sections.

### **6.3 Determination of Force-Deformation Relationship**

The initial stage of the experimental program conducted within the scope of this study was designed to identify the theoretical behavioral characteristics of the devices intended for use in the structural analysis model. In this context, the primary

objective was to determine the force–deformation relationships of each floor isolator prototype. This phase aimed to systematically examine the response behavior of the isolators under various loading conditions and to obtain reliable validation parameters for subsequent numerical modeling. To achieve this, a specialized testing tool was established to accurately capture the force–deformation curves representing the mechanical performance of the isolators.

In the development of the experimental test setup, it was considered essential to accurately control the behavior of both the isolated slab and the loading element, which together represent the equipment positioned on the isolator prototypes. As illustrated in Figure 6.6, the horizontal movement of the isolated slab was constrained by steel profiles, ensuring that lateral displacements were restricted at this level. Consequently, only horizontal motion at the shake table level was permitted, allowing the prototype isolator units to exhibit their natural response in this direction of movement without interference.



Figure 6.6 The modified test setup for obtaining the force-deformation curves of floor isolators (the element that prevents horizontal movement and allows vertical movement is enclosed in a red circle).

Nevertheless, during horizontal loading of the floor isolators, a degree of vertical displacement was anticipated due to alterations occurring along the sliding interfaces. To facilitate this behavior, the test setup was intentionally designed to avoid constraining vertical movement. In order to achieve this, ball bearings were installed at the contact points between the two tie rods positioned on the steel profiles, thereby facilitating unrestricted vertical displacement (marked Figure 6.6). Through this configuration, the experimental system was rendered capable of realistically replicating both horizontal and vertical displacements, providing a test environment that closely captures the true mechanical behavior of the isolators under simulated loading conditions.

A series of experiments were carried out at varying loading speeds and amplitudes to obtain the force–deformation relationships of the two isolator prototypes tested. When selecting harmonic loads, the maximum speed limit of the hydraulic actuator described in Chapter 5 was taken into account. Equation 6.1 was used to calculate the amplitude at variable frequencies.

$$V_{max} = 2 * \pi * f * A \quad (6.1)$$

To assess the potential rate dependency of the devices, each test was repeated under different loading velocities, allowing an evaluation of the isolators' sensitivity to changes in loading speed. The maximum displacement capacity of the manufactured RPII prototypes was determined to be 250 mm. Accordingly, the loading protocol employed in the experiments was established based on the maximum displacement capacity of the actuator used in the test setup. The details of this testing protocol are summarized in Table 6.1.

Table 6.1 Information on harmonic loads used to determine force-deformation relationship

<b>Test No</b>	<b>Amplitude (m)</b>	<b>Velocity (m/s)</b>	<b>Frequency (Hz)</b>	<b>Axial Load (kN)</b>	<b>Number of Cycles</b>
<b>1</b>	±0.038	0.001	0.005	12.5	3
<b>2</b>	±0.075	0.002	0.005	12.5	3
<b>3</b>	±0.038	0.002	0.01	12.5	3
<b>4</b>	±0.075	0.005	0.01	12.5	3
<b>5</b>	±0.150	0.009	0.01	12.5	3
<b>6</b>	±0.150	0.019	0.02	12.5	3
<b>7</b>	±0.150	0.047	0.05	12.5	3
<b>8</b>	±0.150	0.094	0.10	12.5	3
<b>9</b>	±0.150	0.188	0.20	12.5	3
<b>10</b>	±0.100	0.251	0.40	12.5	3
<b>11</b>	±0.075	0.236	0.50	12.5	10

The force–displacement behavior of the RPF1, characterized by the surface equation  $z = 0.48x^2$ , was determined through a series of experiments conducted under varying horizontal displacement conditions. In harmonic tests requiring high speeds, some distortions were observed in the results due to the internal friction of the hydraulic actuator. Therefore, the harmonic test results that best demonstrate the force-deformation relationship were taken into consideration. The hysteresis response obtained for this prototype under harmonic loading with an amplitude of 0.15 m and a frequency of 0.05 Hz (Test No: 7 given in Table 6.1) is presented in Figure 6.7. Analysis of the experimental results revealed that the mechanical behavior of the RPF1 could be effectively idealized using a bi-linear model. This observation provided the basis for the development of a corresponding mathematical representation capable of capturing the fundamental nonlinear response of the system. Figure 6.7 illustrates a comparison between the experimentally derived

force–displacement curve and the theoretical curve generated from the proposed mathematical bi-linear model, demonstrating a strong correlation and confirming the validity of the modeling approach.

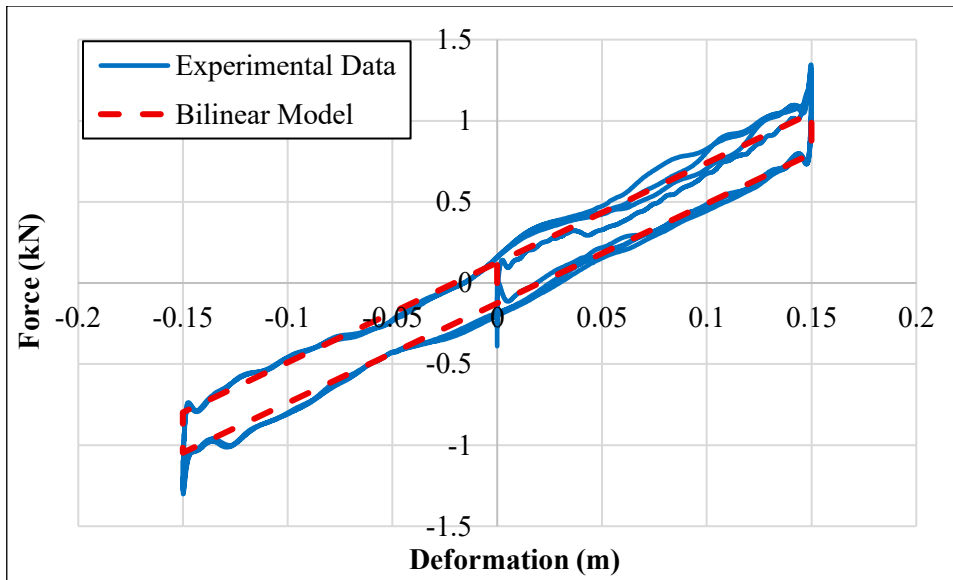


Figure 6.7 Hysteresis results obtained from Test 7 for the floor isolator with a parabolic surface whose surface equation is  $z=0.48x^2$

The force–displacement relationships of the RPF, defined by the surface equation  $z = 0.192x^2$ , were determined through a series of experiments conducted under varying horizontal displacement conditions. As stated in the first prototype, since distortions occurred in the experiments conducted at high speeds due to internal friction of hydraulic actuator, the experiments that best represent the force–deformation relationship were used. The hysteresis curve obtained under harmonic loading with a frequency of 0.05 Hz and an amplitude of 0.15 m (Test No: 7) is presented in Figure 6.8. Analysis of the experimental data indicated that the mechanical response of the RPF could be effectively characterized by a bi-linear behavior model. This modeling approach enabled the theoretical representation of the isolator’s nonlinear response and facilitated the development of a corresponding mathematical formulation. A comparison between the experimentally measured and theoretically predicted force–displacement curves is provided in Figure 6.8,

demonstrating strong agreement and confirming the reliability of the proposed mathematical model in capturing the isolator’s essential behavioral characteristics.

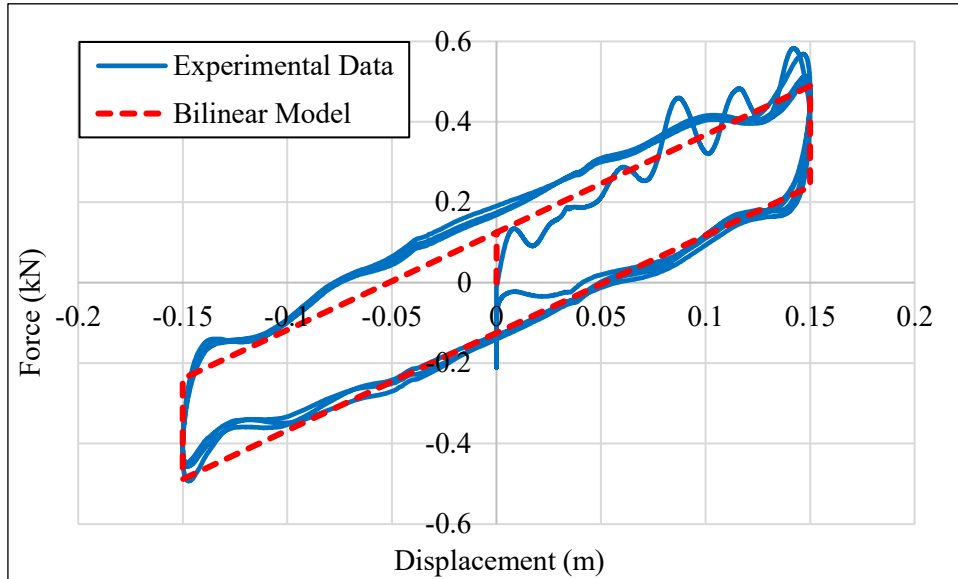


Figure 6.8 Hysteresis results obtained from Test 7 for the floor isolator with a parabolic surface whose surface equation is  $z=0.192x^2$

The effective period, effective horizontal stiffness, and effective damping of the device were calculated by using the experimental results given in Figure 6.7 and Figure 6.8. Furthermore, the bilinear models are obtained by using these experimental results. The device characteristics are presented in Table 6.2.

Table 6.2 Device parameters obtained from bilinear models derived using experimental data

Parabolic Surface Equation	$z=0.48x^2$	$z=0.192x^2$
Effective Period, $T_{\text{eff}}$	2.76 sec	4.15 sec
Effective Stiffness, $K_{\text{eff}}$	1.647 kN/m	0.731 kN/m
Effective Damping, $\xi_{\text{eff}}$	4.82%	10.88%

A comparative evaluation of the dynamic behavior of the two different floor isolator prototypes, characterized by distinct parabolic surface equations ( $z = 0.48x^2$  and  $z = 0.192x^2$ ), reveals the pronounced influence of surface geometry on isolation

performance. The prototype defined by  $z = 0.192x^2$  exhibits a substantially lower effective stiffness (0.731 kN/m) compared to the  $z = 0.48x^2$  prototype (1.647 kN/m), indicating that the reduction in curvature significantly enhances the flexibility of the isolation system. This decrease in stiffness results in a notable increase in the effective period from 2.76 s to 4.15 s, aligning with the fundamental objective of seismic isolation by shifting the structural response away from the short-period range where the dominant seismic energy is concentrated.

Moreover, the prototype with the flatter surface demonstrates more than twice the effective damping ratio (10.88% compared to 4.82%), signifying a considerable improvement in the energy dissipation capacity of the system. Consequently, the isolator with the  $z = 0.192x^2$  surface geometry simultaneously achieves a longer vibration period and higher damping efficiency, both of which are desirable characteristics for seismic performance enhancement. However, this improvement comes at the cost of increased displacement demand. Despite its enhanced ability to dissipate energy under identical loading conditions, the system with the flatter parabolic surface experiences larger horizontal displacements, implying higher deformation requirements for this isolator configuration.

As a result of the experimental investigations, comprehensive force–deformation data were obtained for two different floor isolator prototypes designed with different parabolic surface geometries. The collected force–deformation responses were utilized to develop an idealized bilinear mathematical model capable of representing the dynamic performance of the isolators with sufficient accuracy.

The use of such a simplified yet representative model enables efficient analytical evaluations and facilitates extensive parametric studies, particularly within the context of structural analysis and seismic design. Based on the derived bilinear models, the characteristic parameters of each floor isolator were systematically calculated. In the final stage of the study, these parameters—corresponding to the two parabolic surface geometries—were compared in detail to identify the key differences and similarities in their seismic isolation performance and energy

dissipation mechanisms. This comparative evaluation provided valuable insights into the influence of surface curvature on isolator behavior and contributed to the establishment of a more reliable foundation for the design and optimization of future isolation systems.

#### **6.4 Free Vibration Tests**

Free vibration tests were performed to determine the frictional characteristics and damping ratios of the RPI. In these tests, each isolator was subjected to a vertical load of 12.5 kN applied through the deck positioned above it. Detailed information regarding vertical load is discussed in detail in Chapter 5.1. The system was then displaced to its maximum allowable horizontal deformation and subsequently released, allowing the isolator to oscillate freely under its own restoring force. This procedure produced a damping curve representing the natural decay of motion over time. By analyzing this curve, the friction coefficient and equivalent damping ratio of each device were calculated, providing critical parameters for evaluating the energy dissipation capacity of the isolators. The detailed results obtained from these free vibration tests for the two parabolic surface configurations are presented and discussed separately in 6.4.1 and 6.4.2.

##### **6.4.1 Free Vibration Test Result for the First Prototype with Surface Equation $z=0.48x^2$**

The displacement-time data obtained from the isolated slab with the parabolic surface equation  $z=0.48x^2$  is shown in Figure 6.9.

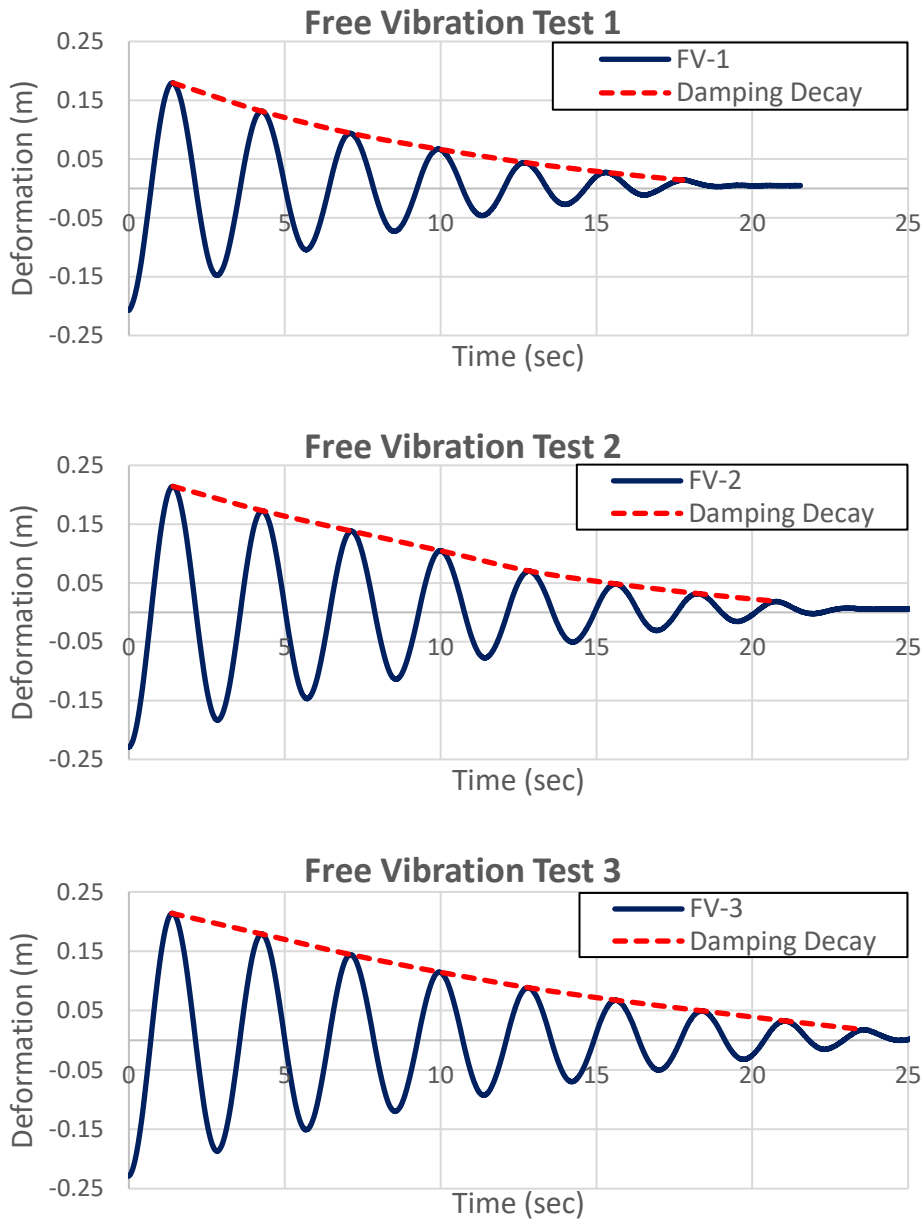


Figure 6.9 Displacement-time plot of the isolated slab with a parabolic surface whose surface equation is  $z=0.48x^2$ , obtained from free vibration experiments

Using the displacement–time data presented in Figure 6.9, the approximate friction coefficient of the device was determined. The friction that occurs between the two parabolic surfaces and the intermediate steel ball in the RPFJ was evaluated using Coulomb’s friction model, based on the free vibration data obtained from the free vibration experiments (Chopra, 2020). To estimate the frictional resistance of the

device, the damping curve generated during the free vibration test was analyzed by identifying the peak displacement values at each oscillation cycle. These peak amplitudes were then used in the friction coefficient calculation. By selecting any two consecutive maximum amplitude points, the free vibration period and corresponding natural frequency of the prototype were computed using Equation 6.2. This approach provided a reliable means of quantifying both the frictional characteristics and the dynamic response behavior of the tested devices.

$$T_n = \frac{\text{Elapsed Time}}{\text{Number of Cycle}} \rightarrow \omega_n = \frac{2\pi}{T_n} \quad (6.2)$$

The effective stiffness of the device, given the known values of its natural frequency and mass, was calculated using the relationship  $k = m\omega_n^2$ . According to the Coulomb friction model (Chopra, 2020), the displacement difference between two successive peak points during free oscillation can be expressed as  $4u_f$ . Furthermore, since the system undergoes free vibration, the only resisting force acting on the moving mass is the frictional force. Based on this principle, the friction coefficient ( $\mu$ ) of the prototype isolator can be determined using the expression provided in Equation 6.3.

$$F = k * u_f \rightarrow mg\mu * \cos(\theta) = m\omega_n^2 * u_f \rightarrow \mu = \frac{u_f * \omega_n^2}{g} \quad (6.3)$$

The friction of the prototype was calculated by using Equation 6.3 and the data in Figure 6.9. The results obtained from the experiments are given in Table 6.3.

Table 6.3 Friction coefficient calculated by using the free oscillation test results of the first prototype of RPF1 whose surface equation is  $z=0.48x^2$

<b>Experiment</b>	<b>Friction Coefficient</b>
FV-1	0.0035
FV-2	0.0036
FV-3	0.0031
<b>Average</b>	<b>0.0034</b>

The average value of the friction coefficients calculated from three different free vibration experiments was determined to be 0.0034. The fact that the absolute value of the calculated friction coefficient is quite small indicates that it is negligible in the relevant calculations and models.

Another value obtained from free vibration tests is the damping ratio of the device. The damping ratio, which is a characteristic of prototype devices, was calculated by using the displacement and time data given in Figure 6.9. The damping ratios of prototype devices can be calculated using Equation 6.4 by utilizing the points where the highest amplitudes occurring in each cycle during free vibration behavior are observed (Chopra, 2020).

$$\frac{u_i}{u_{i+1}} = \exp\left(\frac{2\pi\xi}{\sqrt{1-\xi^2}}\right) \quad (6.4)$$

In Equation 6.4, when  $\xi$  is less than 0.2,  $\sqrt{1-\xi^2}$  is approximately equal to 1. Therefore, Equation 6.4 can be simplified to obtain Equation 6.5.

$$\frac{u_i}{u_{i+1}} = \exp(2\pi\xi) \rightarrow \xi = \frac{\ln(u_i/u_{i+1})}{2\pi} \quad (6.5)$$

The damping calculation given in Equation 6.5 can be adapted for non-consecutive cycles. The damping ratios of prototype devices can be calculated as in Equation 6.6 by using any two points, named  $i$  and  $i+j$ , where the highest amplitude is observed.

$$\xi = \frac{1}{2\pi j} \ln\left(\frac{u_i}{u_{i+j}}\right) \quad (6.6)$$

The damping ratio was calculated by using the binary combinations of all specified points which is given Figure 6.9, and the average value of the calculated values was calculated. The results obtained from the experiments are presented in Table 6.4.

Table 6.4 Damping ratio calculated by using the free vibration test results of the first prototype of RPF1 whose surface equation is  $z=0.48x^2$

<b>Experiment</b>	<b>Damping Ratio (%)</b>
FV-1	6.56
FV-2	5.51
FV-3	4.75
<b>Average</b>	<b>5.61</b>

The average damping ratio obtained from three independent free vibration tests was calculated to be 5.6%. The overall experimental outcomes exhibit acceptable consistency and reliability. Furthermore, the experimental findings provided strong validation for the analytical model. As detailed in Chapter 3.3, the analytical study demonstrated that the damping ratio values derived from the FV-3 test series showed close agreement with the corresponding analytical predictions. This consistency between experimental and analytical results supports the accuracy and reliability of the modeling approach described in Chapter 3.

### 6.4.2 Free Vibration Test Result for the Second Prototype with Surface Equation $z=0.192x^2$

The displacement-time data obtained from the isolated slab with the parabolic surface equation  $z = 0.192x^2$  is shown in Figure 6.10.

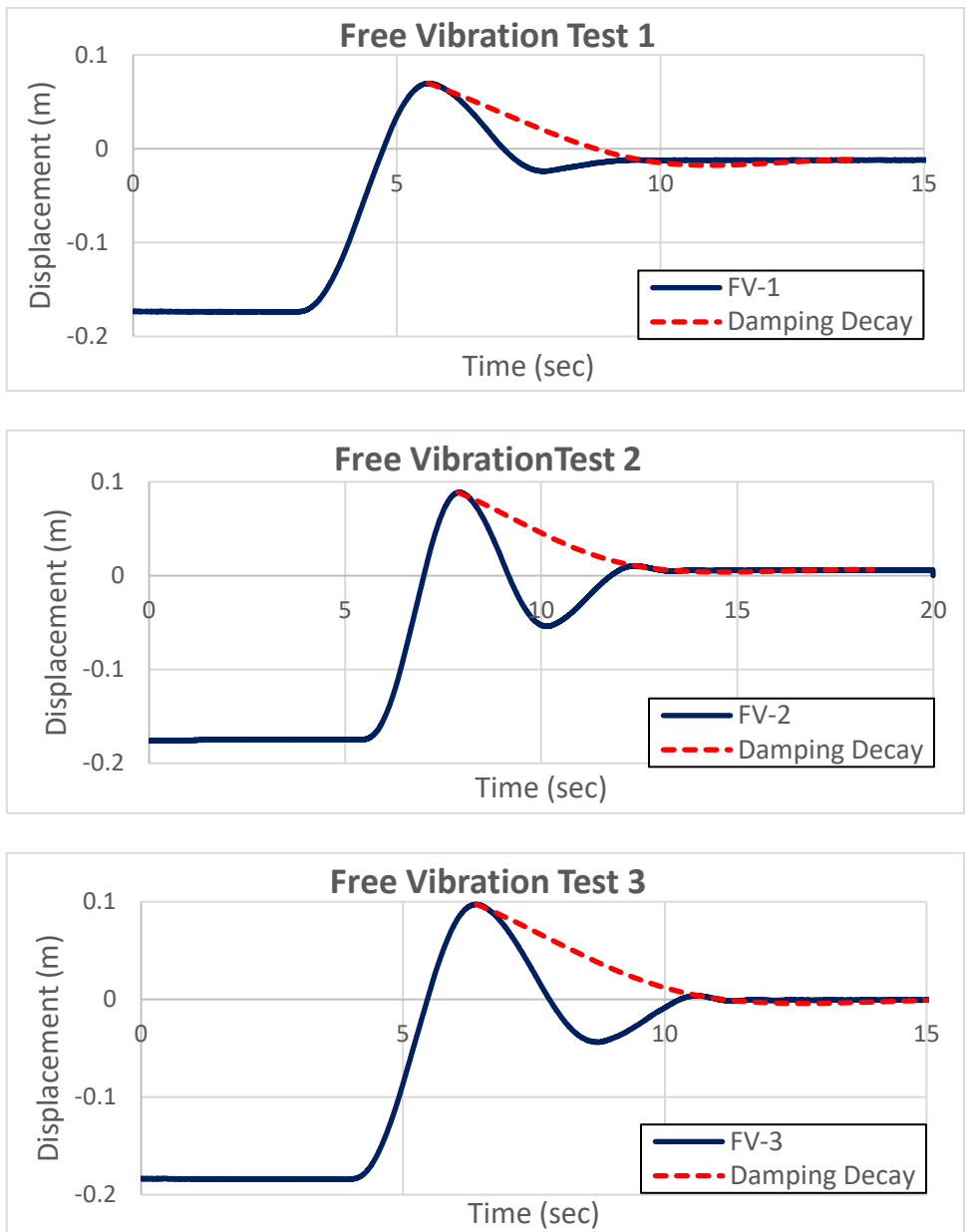


Figure 6.10 Displacement-time plot of the isolated slab with a parabolic surface whose surface equation is  $z=0.192x^2$ , obtained from free vibration experiments

As a result of three separate free vibration experiments, the damping ratio of the system could not be reliably calculated by using the method described in Chapter 6.4.1. It was difficult to determine the damping ratio because the amplitudes could not be tracked for a sufficient number of cycles. Therefore, the damping ratio of the second prototype of RPF1 with a surface equation of  $z = 0.192x^2$  could not be calculated by using experimental methods. The damping ratio of this prototype was calculated using the method described in Chapter 3.3, which was confirmed by the first prototype's experimental data. Considering the geometric properties of the parabolic surface, the system was idealized based on the equivalent radius, and thus the isolator in question was considered as a pendulum-type isolator. Thus, the damping ratio was calculated by comparing the dynamic behavior of the system to a pendulum motion. To evaluate the accuracy of the method, the first prototype tests of floor isolator with a surface equation of  $z = 0.48x^2$  were used. The damping ratio for the first prototype was calculated by using the equation given in TEC (2018) Section 14, Item 14B.5. As a result of this calculation, the damping ratio of the first prototype was calculated as 4.8%. It was observed that this calculated damping value was very close to the 4.75% damping ratio calculated from the free vibration test coded FV-3 presented in Chapter 6.4.1. This confirms the reliability and usability of the approach in question. In the evaluations performed for the second prototype of the parabolic floor isolator, the equivalent radius value was determined to be 5.216 m. By using this value and assuming a friction coefficient of 0.01, the damping ratio was determined to be 10.99%. This result is very close to the damping ratio obtained from the hysteresis presented in Figure 6.8. This situation demonstrates that calculations based on the equivalent radius approach can produce results that are both consistent and close to physical reality. Therefore, this method can be used as an effective tool for evaluating damping characteristics in similar systems.

## 6.5 Harmonic Tests

The dynamic responses of the evaluated floor isolators were characterized by experiments under various harmonic excitations. Throughout this procedure, harmonic excitations at several frequencies were imposed, and the vibration responses of the isolators were recorded. The amplitudes of harmonic effects at different frequencies were determined based on the relationship in Equation 6.1. Owing to the devices possessing varying effective durations, the studies were executed according to two distinct experimental protocols for each prototype. The fundamental strategy was minimizing the loading frequency spectrum in frequency ranges adjacent to the natural frequency of the floor isolator. This method enabled the observation of the device's dynamic behavior and resonance response around its effective period with enhanced resolution and clarity. Comprehensive analyses of the two distinct experimental methodologies employed and the results derived from these methodologies are delineated in Chapter 6.5.1 and Chapter 6.5.2.

### 6.5.1 Results of the Harmonic Tests for the First Prototype with Surface Equation $z=0.48x^2$

Experiments were conducted by using RRFI characterized by the surface equation  $z = 0.48x^2$ , with measurements obtained from the isolated slab and shake table under ten distinct harmonic effects. The frequency and amplitude values for the harmonic loads are presented in Table 6.5.

Table 6.5 Harmonic test protocol used in the experiments of the first prototype with surface equation  $z=0.48x^2$

<b>Test Code</b>	<b>frequency (Hz)</b>	<b>Amplitude (mm)</b>	<b>Number of Cycles</b>
<b>C1</b>	4	20	10
<b>C2</b>	2	20	10
<b>C3</b>	1.5	25	10
<b>C4</b>	1.2	30	5
<b>C5</b>	1.0	30	5
<b>C6</b>	0.8	30	5
<b>C7</b>	0.6	30	5
<b>C8</b>	0.5	60	5
<b>C9</b>	0.35	30	5
<b>C10</b>	0.25	30	5

In the experimental technique, movement at isolated slab was detected in all tests conducted on the prototype devices. In other words, the devices were activated in all harmonic loadings. In the C9 experiment, which is very close to the prototype device's fundamental frequency of 0.345 Hz, a notable rise was recorded, resulting in the device attaining its displacement threshold. The findings of relative displacement derived from the harmonic tests are illustrated in Figure 6.11.

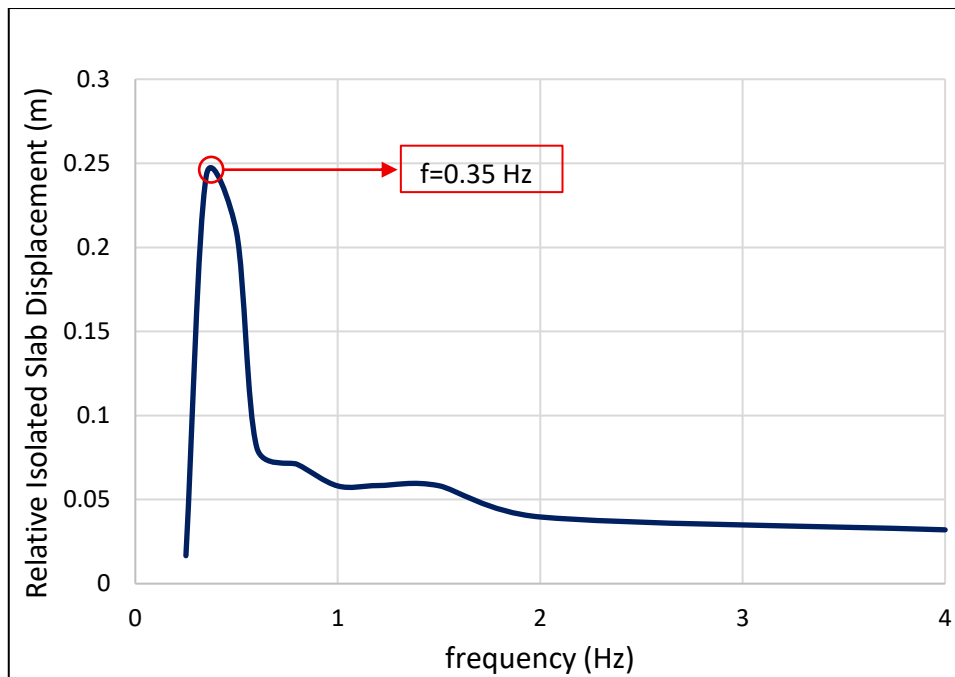


Figure 6.11 Displacement demands during harmonic tests obtained on the isolated slab located above the floor isolator with surface equation  $z=0.48x^2$

Figure 6.11 shows the correlation between the vibration frequency (Hz) and the relative displacement above the isolator under harmonic loads. A specific resonance phenomenon is seen in the system's dynamic behavior when viewing the given curve. The maximum displacement was observed in the C9 test, which featured a load around the device's effective frequency of 0.345 Hz. The device's maximum displacement requirement does not exceed 0.25 m. Displacement exhibits a fast decline at frequencies below and somewhat over 0.35 Hz, with a significant reduction in displacement amplitude noted at 1 Hz and higher frequencies, subsequently followed by a progressively damped, more level trajectory. This declining reaction illustrates the isolator's capacity to efficiently disperse and attenuate high-frequency vibrational energy. Consequently, these test results distinctly demonstrate the dynamic properties of the isolator system in its fundamental mode and its efficacy within the operating frequency spectrum.

### 6.5.2 Results of the Harmonic Tests for the Second Prototype with Surface Equation $z=0.192x^2$

During experiments on RPF1 with a surface equation of  $z = 0.192x^2$ , measurements were taken from the isolated slab and shake table under 10 different harmonic effects. The frequency and amplitude values for the harmonic loads are given in Table 6.6.

Table 6.6 Harmonic test protocol used in the experiments of the prototype with surface equation  $z=0.192x^2$

<b>Test Code</b>	<b>frequency (Hz)</b>	<b>Amplitude (mm)</b>	<b>Number of Cycle</b>
<b>C1</b>	4	20	20
<b>C2</b>	2	20	20
<b>C3</b>	1.5	25	20
<b>C4</b>	1	30	10
<b>C5</b>	0.8	30	10
<b>C6</b>	0.5	60	10
<b>C7</b>	0.35	60	10
<b>C8</b>	0.25	60	10
<b>C9</b>	0.22	60	10
<b>C10</b>	0.1	100	5

In the applied test protocol, movement was observed in all tests on the prototype device. In the C9 test conducted at 0.22 Hz, the fundamental frequency of the prototype device, a significant increase was observed, and the device reached its displacement limit. The relative displacement results obtained from the harmonic tests are given in Figure 6.12.

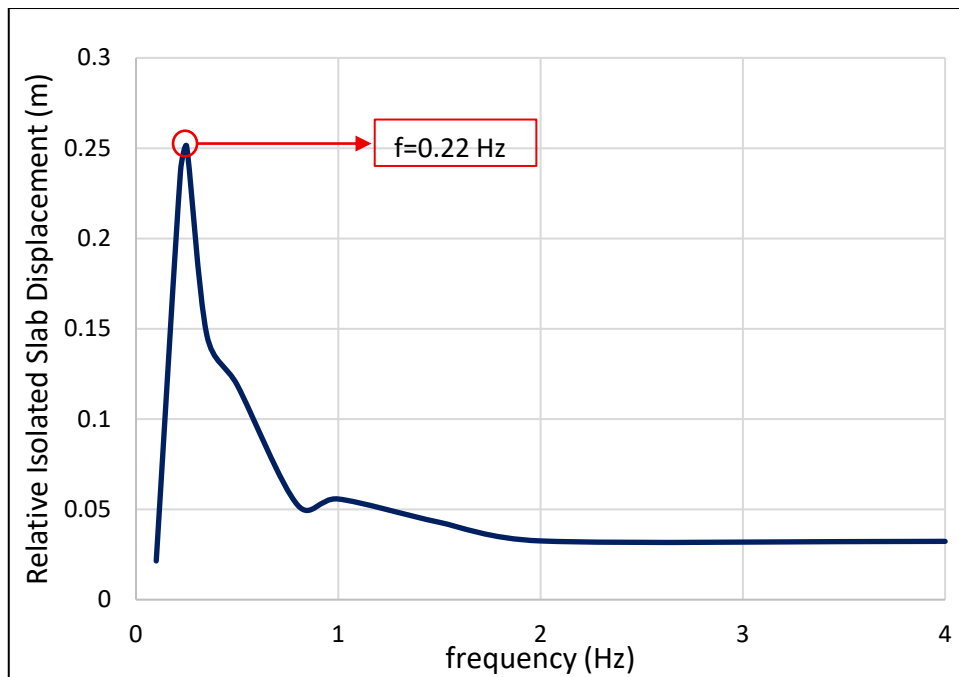


Figure 6.12 Displacement demands during harmonic tests obtained on the isolated slab located above the floor isolator with surface equation  $z=0.192x^2$

Upon examining the given curve, it is observed that the system behaves similarly to the first prototype which has surface equation  $z = 0.48x^2$ . The maximum displacement demand was observed in the C9 test with a loading frequency of 0.22 Hz, which is the fundamental frequency of the device. The device's highest displacement demand occurred in the C9 test and was of order of 0.25 m. Displacement showed a rapid decrease at frequencies below and just above 0.22 Hz. The device did not exhibit high displacement demands at high frequencies. Displacement demands showed a significant decrease above 1 Hz, resulting in low displacement demands.

Harmonic tests were conducted to evaluate the frequency-dependent dynamic behavior of the system for RPII prototypes. Within the scope of the tests, harmonic excitations were applied at different frequencies, and the displacement responses of the isolators were recorded. The results showed that the largest displacement demands in both prototypes occurred at loads close to the dominant fundamental frequencies of the devices. This is consistent with parabolic surface systems

exhibiting approximately linear dynamic behavior in small displacement regions and an equivalent natural period being definable in this region. It was observed that displacement demands decreased significantly at frequencies below and above the fundamental frequency. Furthermore, the fact that both prototypes exhibit similar trends under harmonic excitation demonstrates that the frequency–response character of the parabolic surface is consistent, despite the differences in surface geometry. These results confirm that the isolators operate stably with limited displacements outside resonance region.

## **6.6 Strong Ground Motion Tests**

To investigate the dynamic behavior of the developed floor isolators under real earthquake conditions, the specimens were tested under selected strong ground motions. Within this scope, two different ground motion sets, GM Set-1 and GM Set-2, were defined. The records included in GM Set-1 were applied to both prototypes, while the records within the scope of GM Set-2 were used only in the experiments of the second prototype. The primary reason for this is to examine the dynamic match between the fundamental vibration periods of the prototypes and the seismic inputs. GM Set-1 was scaled based on the fundamental period of the first prototype; however, it was also used in the second prototype tests to observe the performance differences between the two prototypes and provide a comparative analysis. In contrast, GM Set-2 was selected directly according to the dynamic characteristics of the second prototype. Since the data provided by GM Set-1 offered sufficient statistical significance for inter-prototype comparison, GM Set-2 was applied only to the second prototype to verify the responses of the second prototype within its fundamental period. Detailed information regarding the strong ground motion sets used in the experiments and the selection criteria for these records is provided in Chapter 4.

The experimental data obtained from both  $z = 0.48x^2$  and  $z = 0.192x^2$  prototypes are presented in detail under Chapter 6.6.1 and Chapter 6.6.2, respectively.

### **6.6.1 Analysis of Strong Ground Motion Test Results for the Prototype with Surface Equation $z=0.48x^2$**

In the experiments of the first prototype, the GM Set-1, consisting of 17 acceleration records detailed in Chapter 4, was used. The system's acceleration and displacement responses were recorded as a result of these ground motions applied via a single axis shaking table. The changes in the displacement of the isolated slab in the X-axis and Y-axis directions and the deck rotation demands around the Z-axis for the selected experiments are presented in Figure 6.13. In the axis definitions, the X-axis represents the direction of excitation, the Y-axis represents the horizontal axis orthogonal to direction excitation, and the Z-axis represents the vertical direction. The blue line on the displacement plot in Figure 6.13 represents the displacement of the isolated slab in the X direction. The displacement of the isolated slab in the Y direction, which is perpendicular to the direction of excitation, is likewise depicted by the red dashed line in the same plot. The rotation around the vertical axis, or Z-axis, is displayed in the rotation plot. The angle created by the horizontal axis is represented by this rotation.

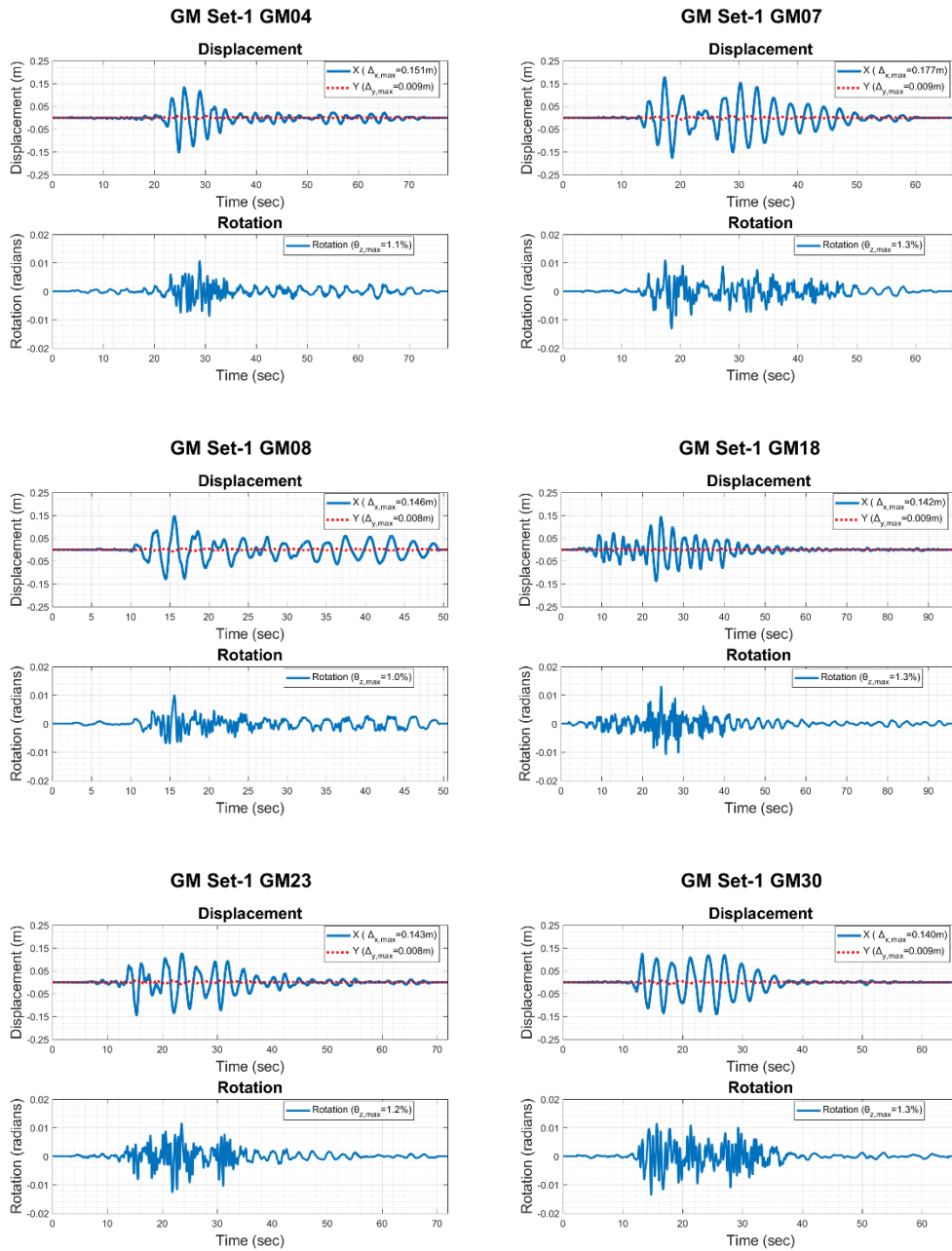


Figure 6.13 Displacement responses of the first prototype under selected strong ground motions from GM Set-1

To determine the seismic performance of the first prototype, the results of dynamic tests conducted using all records within the GM Set-1 were subjected to detailed analysis. Within this scope, the maximum absolute displacement and deck rotation demands to which the system was subjected for each applied ground motion were

analyzed. The maximum response parameters have been compiled in Table 6.7 to summarize the system's behavior in a comprehensive manner.

Table 6.7 Maximum displacement and rotation responses of isolated slab of the first prototype under GM Set-1

<b>GM Set</b>	<b>Earthquake Code</b>	<b><math>\Delta_{x,max}</math> (m)</b>	<b><math>\Delta_{y,max}</math> (m)</b>	<b><math>\theta_{z,max}</math> (Radian)</b>
<b>GM Set-1</b>	<b>GM01</b>	0.200	0.010	0.016
<b>GM Set-1</b>	<b>GM02</b>	0.222	0.012	0.016
<b>GM Set-1</b>	<b>GM04</b>	0.151	0.009	0.011
<b>GM Set-1</b>	<b>GM05</b>	0.076	0.005	0.006
<b>GM Set-1</b>	<b>GM07</b>	0.177	0.009	0.013
<b>GM Set-1</b>	<b>GM08</b>	0.146	0.008	0.010
<b>GM Set-1</b>	<b>GM11</b>	0.174	0.011	0.034
<b>GM Set-1</b>	<b>GM14</b>	0.103	0.005	0.019
<b>GM Set-1</b>	<b>GM16</b>	0.125	0.005	0.007
<b>GM Set-1</b>	<b>GM18</b>	0.142	0.009	0.013
<b>GM Set-1</b>	<b>GM19</b>	0.163	0.009	0.020
<b>GM Set-1</b>	<b>GM20</b>	0.176	0.013	0.012
<b>GM Set-1</b>	<b>GM22</b>	0.104	0.007	0.008
<b>GM Set-1</b>	<b>GM23</b>	0.143	0.008	0.012
<b>GM Set-1</b>	<b>GM28</b>	0.182	0.014	0.021
<b>GM Set-1</b>	<b>GM29</b>	0.094	0.008	0.007
<b>GM Set-1</b>	<b>GM30</b>	0.140	0.009	0.013
<b>GM Set-1</b>	<b>Average</b>	<b>0.148</b>	<b>0.009</b>	<b>0.014</b>

When evaluating the analysis results presented in Table 6.7, it is observed that the displacement demands in the X-axis, which is the direction of excitation, remain within the design displacement capacity of the prototype. The highest displacement recorded in the X-axis occurred in the GM02 ground motion at 0.222 m, while the lowest displacement occurred in the GM05 ground motion at 0.076 m. It was determined that the displacements on the Y-axis, which is orthogonal to the direction of excitation, remained at a very limited level. The maximum value on this axis was measured as 0.014 m in the GM28 record. On the other hand, it was found that the deck rotation responses around the Z-axis averaged below 0.02 radians. This situation, which is consistent with the harmonic test findings, indicates that the isolators did not exhibit significant torsion behavior under single-axis excitation.

Consequently, it is understood that the displacement capacity of the first prototype of RPF1 is not exceeded, and that movements in the orthogonal direction and torsional effects are negligible.

Within the scope of strong ground motion tests, another critical performance parameter examined alongside displacement demands is the acceleration reduction ratio. To evaluate the performance of limiting inertial forces transmitted to the superstructure, which is the fundamental objective of the seismic isolation system, the changes in the time domain of the isolated slab and shaking table accelerations were examined comparatively. The acceleration-time histories obtained for selected records are presented in Figure 6.14. The acceleration reduction ratio, which numerically expresses the isolation efficiency, was calculated by dividing the difference between the maximum acceleration of the ground motion applied to the shaking table and the maximum response acceleration measured at the level of the isolated floor during the test by the maximum acceleration of the applied ground motion. This ratio clearly demonstrates the extent to which the system dissipates seismic energy and reduces acceleration demands on the superstructure. The calculation method for the acceleration reduction ratio is provided in Chapter 3. The data shown by the blue line in the plots in Figure 6.13 is the acceleration data measured from the isolated slab, referred to as floor acceleration. The data shown by the red dashed line in the same plot is the acceleration data associated with strong ground motion.

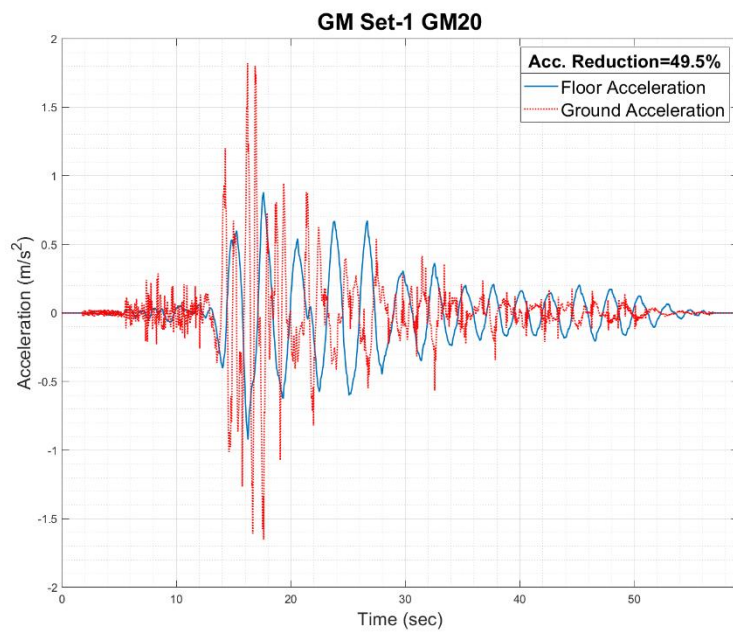
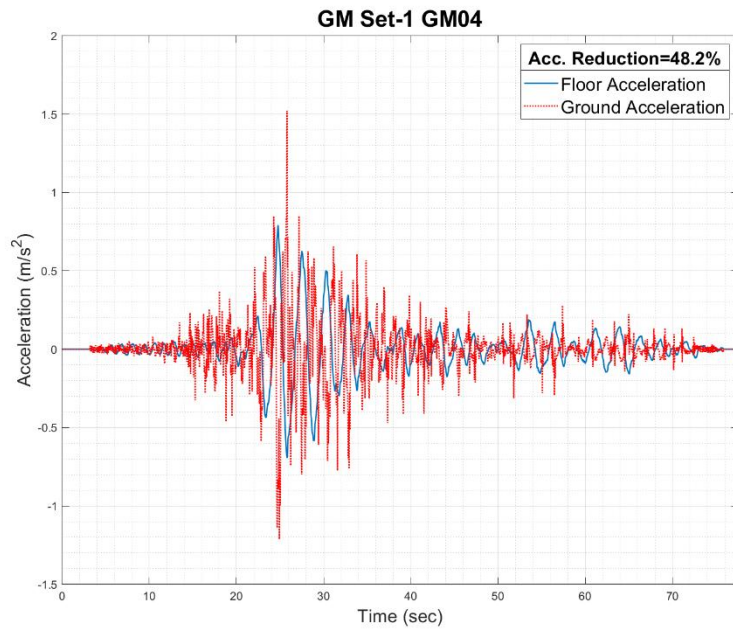


Figure 6.14 Acceleration responses for the first prototype obtained under selected strong ground motions from GM Set-1

The performance of acceleration reduction, derived from the selected records in Figure 6.14, is summarized in Table 6.8 for the complete set of strong ground motions. Upon comprehensive evaluation of the experimental results, it is evident that the acceleration demands imposed on the isolated slab are markedly reduced across all loading scenarios. The mean acceleration reduction ratio for the complete test series was determined to be 55.6%. Moreover, analysis of Table 6.8 indicates that under specific ground motions, the system neared the 80% reduction ratio aimed for during the design phase and exhibited significant acceleration reduction.

Table 6.8 Acceleration Reduction Ratios from Experiments Conducted with GM Set-1 Acceleration Records for the First Prototype

<b>GM Set</b>	<b>Earthquake Code</b>	<b>Acceleration Reduction (%)</b>
<b>GM Set-1</b>	<b>GM01</b>	36.2%
<b>GM Set-1</b>	<b>GM02</b>	4.8%
<b>GM Set-1</b>	<b>GM04</b>	48.2%
<b>GM Set-1</b>	<b>GM05</b>	57.9%
<b>GM Set-1</b>	<b>GM07</b>	44.8%
<b>GM Set-1</b>	<b>GM08</b>	71.9%
<b>GM Set-1</b>	<b>GM11</b>	63.5%
<b>GM Set-1</b>	<b>GM14</b>	75.4%
<b>GM Set-1</b>	<b>GM16</b>	74.6%
<b>GM Set-1</b>	<b>GM18</b>	57.0%
<b>GM Set-1</b>	<b>GM19</b>	58.6%
<b>GM Set-1</b>	<b>GM20</b>	49.5%
<b>GM Set-1</b>	<b>GM22</b>	60.7%
<b>GM Set-1</b>	<b>GM23</b>	61.4%
<b>GM Set-1</b>	<b>GM28</b>	25.1%
<b>GM Set-1</b>	<b>GM29</b>	83.3%
<b>GM Set-1</b>	<b>GM30</b>	72.6%
<b>GM Set-1</b>	<b>Average</b>	55.6%

Strong ground motion tests conducted on the first prototype of RPII characterized by the equation  $z=0.48x^2$  have yielded significant findings revealing the system's seismic performance. Experimental data revealed that the system exhibited consistent behavior in terms of reducing the accelerations transmitted to the superstructure, with an average acceleration reduction rate of 55.6%. In all strong

ground motion scenarios, it was observed that the isolated slab accelerations were reduced compared to strong ground motion accelerations, confirming the isolation efficiency of the system. On the other hand, when examining displacement demands, a critical parameter in terms of safety, it was observed that the displacement capacity of the floor isolator was not exceeded in any test and that the motion was safely damped within the design limits. Although the average acceleration reduction ratio fell below the 80% target, the fact that this target was approached in some specific loadings. Upon comprehensive evaluation, it was concluded that the first prototype of the RPI demonstrated effective and satisfactory seismic performance in terms of both minimizing acceleration demands and maintaining displacement limits.

## **6.6.2 Analysis of Strong Ground Motion Test Results for the Prototype with Surface Equation $z=0.192x^2$**

Two different sets of strong ground motion data were used for the strong ground motion tests of the second prototype of the RPI. General information about both sets of strong ground motion data is provided in Chapter 4. The results obtained from GM Set-1 and GM Set-2 were examined in Chapter 6.6.2.1 and Chapter 6.6.2.2, respectively.

### **6.6.2.1 Results of Strong Ground Motion Tests by Using GM Set-1**

The experimental assessment of the second prototype, the GM Set-1, utilized 17 acceleration recordings as outlined in Chapter 4. The system's acceleration and displacement responses were recorded under these ground motions applied by a single-axis shaking table. The displacements of the isolated slab in the X and Y principal directions, along with the deck rotation demands around the Z principal axis for the chosen experiments, are given in Figure 6.15. Figure 6.14 shows the displacement of the isolated slab in the X direction, or in other words, the displacement in the direction of excitation, indicated by the blue line on the

displacement plot. Similarly, the red dashed line in the same plot shows the displacement of the isolated slab in the Y direction, which is perpendicular to the direction of excitation. The rotation plot shows the rotation around the Z-axis, which is the vertical axis. This rotation represents the angle formed with the horizontal axes.

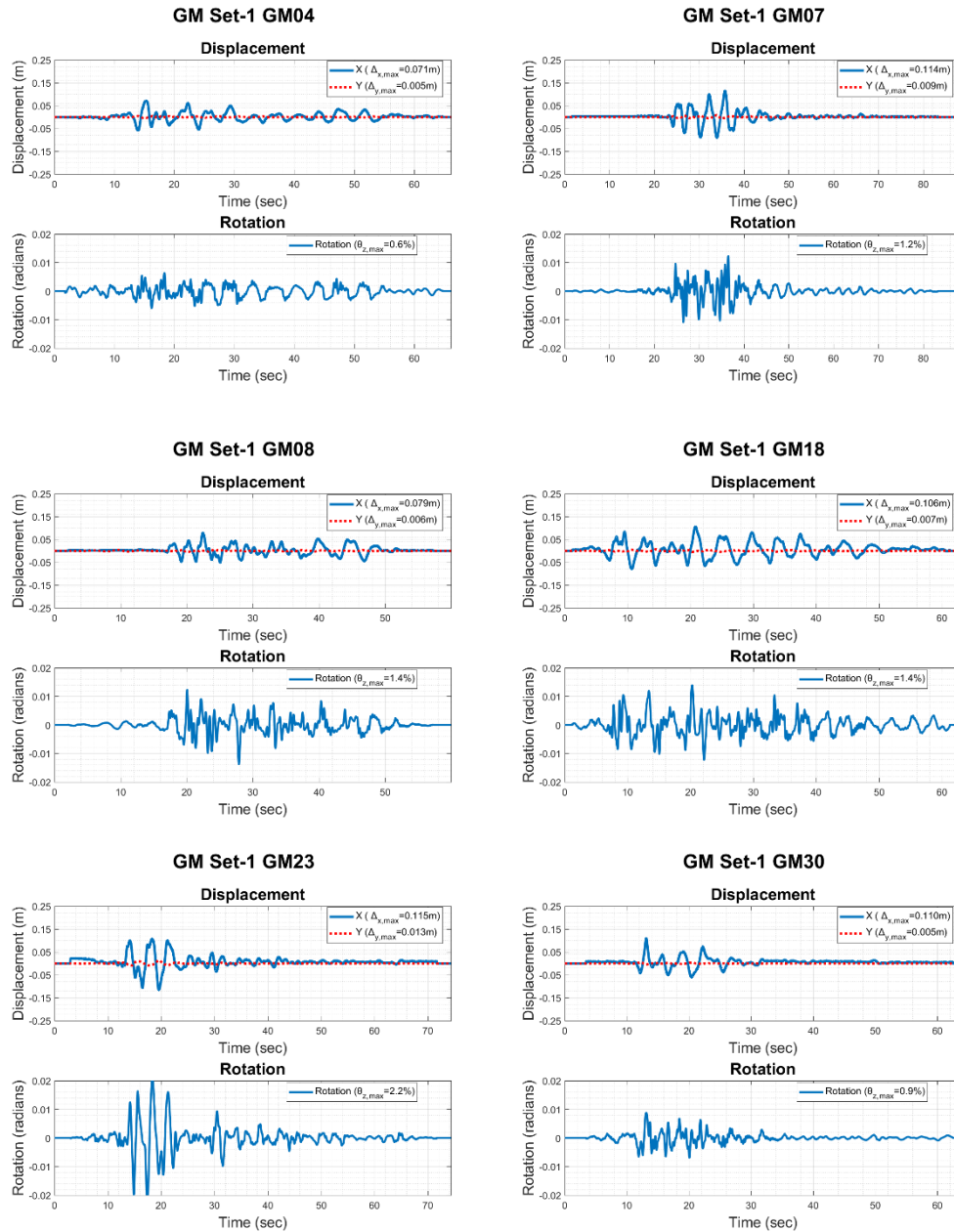


Figure 6.15 Displacement and deck rotation responses of the second prototype under selected strong ground motions from GM Set-1

The seismic performance of the second prototype was assessed by analyzing the results of dynamic tests conducted with all records in GM Set-1. The maximum absolute displacement on the X and Y axes, as well as the deck rotation demands around the vertical axis, were computed for each ground motion effect. The essential reaction parameters indicative of the system's overall behavior is included in Table 6.9.

Table 6.9 Maximum displacement and rotation responses of isolated slab of the second prototype under GM Set-1

<b>GM Set</b>	<b>Earthquake Code</b>	<b><math>\Delta_{x,max}</math> (m)</b>	<b><math>\Delta_{y,max}</math> (m)</b>	<b><math>\theta_{z,max}</math> (Radian)</b>
<b>GM Set-1</b>	<b>GM01</b>	0.134	0.006	0.021
<b>GM Set-1</b>	<b>GM02</b>	0.254	0.013	0.037
<b>GM Set-1</b>	<b>GM04</b>	0.071	0.005	0.006
<b>GM Set-1</b>	<b>GM05</b>	0.087	0.007	0.012
<b>GM Set-1</b>	<b>GM07</b>	0.114	0.009	0.012
<b>GM Set-1</b>	<b>GM08</b>	0.079	0.006	0.014
<b>GM Set-1</b>	<b>GM11</b>	0.081	0.004	0.007
<b>GM Set-1</b>	<b>GM14</b>	0.103	0.004	0.008
<b>GM Set-1</b>	<b>GM16</b>	0.082	0.005	0.010
<b>GM Set-1</b>	<b>GM18</b>	0.106	0.007	0.014
<b>GM Set-1</b>	<b>GM19</b>	0.128	0.008	0.013
<b>GM Set-1</b>	<b>GM20</b>	0.150	0.006	0.023
<b>GM Set-1</b>	<b>GM22</b>	0.074	0.004	0.014
<b>GM Set-1</b>	<b>GM23</b>	0.115	0.013	0.022
<b>GM Set-1</b>	<b>GM28</b>	0.141	0.010	0.031
<b>GM Set-1</b>	<b>GM29</b>	0.076	0.008	0.011
<b>GM Set-1</b>	<b>GM30</b>	0.110	0.005	0.009
<b>GM Set-1</b>	<b>Average</b>	<b>0.112</b>	<b>0.007</b>	<b>0.015</b>

Upon reviewing the experimental findings in Table 6.9, it is seen that the displacement demands along the X-principal axis, the direction of excitation, stay within the displacement capacity of the prototype, with the exception of GM02. The maximum displacement observed on the X-principal axis was 0.254 m in GM02, while the minimum displacement recorded was 0.071 m in GM04. The displacement

capacity of the second prototype was exceeded in GM02, resulting in the ball striking the device walls. Displacements along the Y-axis, which is orthogonal to the direction of excitation, were found to be minimal, with a maximum value of 0.013 m recorded in GM02. Conversely, the mean deck rotation responses around the Z-axis remained around 0.02 radians. This scenario demonstrates that the isolators displayed consistent performance without considerable deck rotation under uniaxial excitation. The second prototype of the RPF1 was found to remain within displacement limitations, with the exception of GM02. Moreover, perpendicular movement to the direction of excitation is negligible, and deck rotation was minimal.

The acceleration demands measured in strong ground motion tests are presented in Figure 6.16 for the selected records. The acceleration measured from the isolated slab and the acceleration record associated with strong ground motion were plotted on the same plot for comparison, and the acceleration reduction ratio was calculated. Chapter 3 provides the acceleration reduction ratio calculating method. The floor acceleration, or acceleration data taken from the isolated slab, is shown by the blue line in the figures in Figure 6.16. The acceleration data related to strong ground motion is represented by the red dashed line in the same plot.

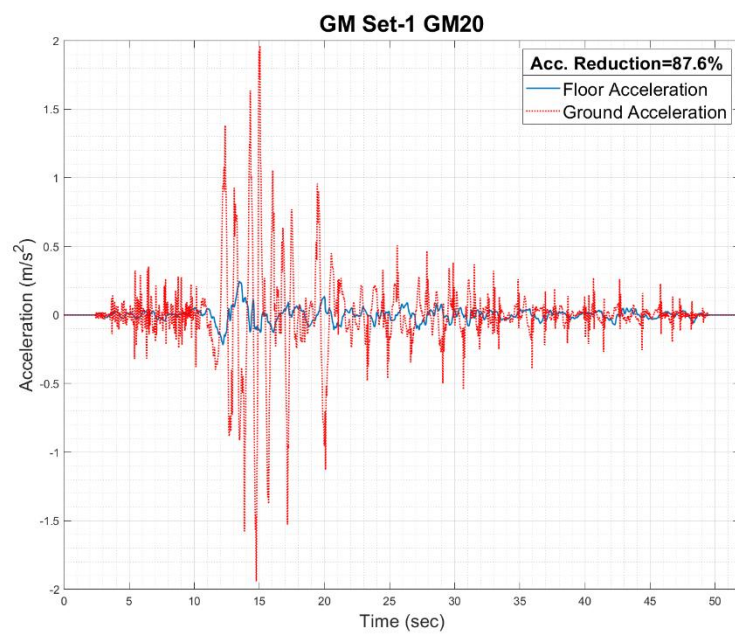
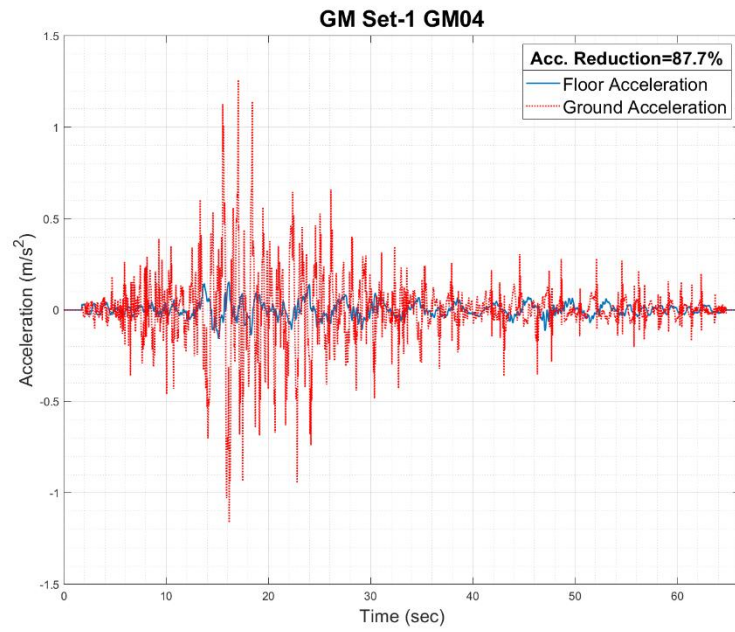


Figure 6.16 Acceleration responses for the second prototype obtained under selected strong ground motions from GM Set-1

The acceleration reduction ratios obtained for all records except GM02 are given in Table 6.10. Acceleration reduction could not be achieved in the GM02 ground motion where the displacement limit was reached. On the contrary, the floor response acceleration for GM02 reached 2.28 times the maximum ground motion acceleration, showing a significant amplification. For this reason, GM02 is not shown in Table 6.10. When this exceptional case was removed from the data set, the average acceleration reduction ratio for the remaining 16 ground motions was calculated as 88.3%. Table 6.10 shows that all of these records achieved a reduction performance of over 80%, with the GM29 record reaching the highest level at 94.9%.

Table 6.10 Acceleration reduction rates from experiments conducted with GM Set-1 acceleration records for the second prototype

<b>GM Set</b>	<b>Earthquake Code</b>	<b>Acceleration Reduction (%)</b>
<b>GM Set-1</b>	<b>GM01</b>	84.1%
<b>GM Set-1</b>	<b>GM04</b>	87.7%
<b>GM Set-1</b>	<b>GM05</b>	81.7%
<b>GM Set-1</b>	<b>GM07</b>	85.3%
<b>GM Set-1</b>	<b>GM08</b>	94.0%
<b>GM Set-1</b>	<b>GM11</b>	94.0%
<b>GM Set-1</b>	<b>GM14</b>	89.5%
<b>GM Set-1</b>	<b>GM16</b>	93.4%
<b>GM Set-1</b>	<b>GM18</b>	89.7%
<b>GM Set-1</b>	<b>GM19</b>	88.2%
<b>GM Set-1</b>	<b>GM20</b>	87.6%
<b>GM Set-1</b>	<b>GM22</b>	87.1%
<b>GM Set-1</b>	<b>GM23</b>	85.6%
<b>GM Set-1</b>	<b>GM28</b>	77.1%
<b>GM Set-1</b>	<b>GM29</b>	94.9%
<b>GM Set-1</b>	<b>GM30</b>	92.5%
<b>GM Set-1</b>	<b>Average</b>	88.3%

The results of the strong ground motion tests conducted on the second prototype under the GM Set-1 show that the system meets its overall performance objectives. When examining displacement and rotation behaviors, it was determined that displacements in the direction of excitation remained within design limits except for

the GM02 record, orthogonal movements were quite limited, and deck rotation around the vertical axis were negligible. In terms of acceleration performance, a reduction efficiency of over 80% was achieved in all records except GM02. Consequently, it is understood that, excluding extraordinary instances that challenge capacity limits, the system provides effective acceleration reduction under strong ground motions and exhibits stable behavior.

### 6.6.2.2 Results of Strong Ground Motion Tests Using GM Set-2

Due to the long natural period of the second prototype, it was necessary to use strong ground motions scaled to longer periods in the experiments. For this purpose, a special set of strong ground motions, consisting of a total of 7 records and named GM Set-2, was created. The selection criteria and general characteristics of these ground motions are detailed in Chapter 4.

Displacement and rotation responses obtained from experiments conducted using GM Set-2 were analyzed. To illustrate the system's behavior, displacement and deck rotation histories for selected recordings are presented in Figure 6.17.

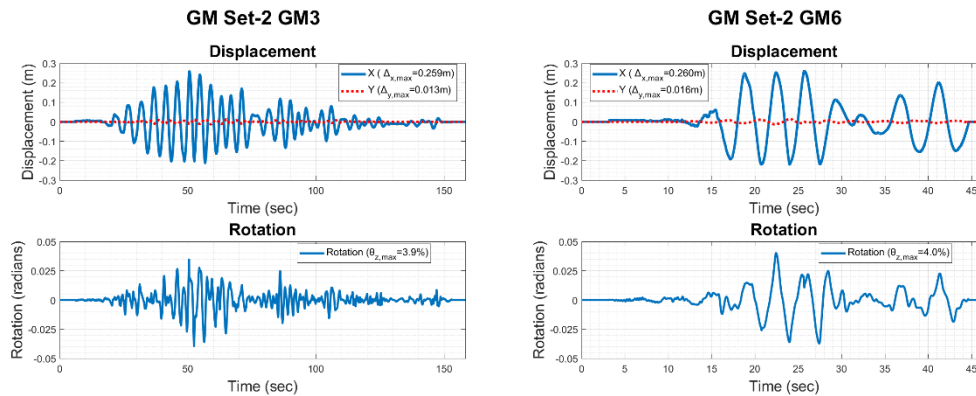


Figure 6.17 Displacement and deck rotation responses of the second prototype under selected strong ground motions from GM Set-2

The maximum displacement and maximum rotation results obtained from all experiments conducted using GM Set-2 are summarized in Table 6.11.

Table 6.11 Maximum displacement and deck rotation responses of the second prototype at isolated slab under GM Set-2

<b>GM Set</b>	<b>Earthquake Code</b>	$\Delta_{x,max}$ (m)	$\Delta_{y,max}$ (m)	$\theta_{z,max}$ (Radian)
<b>GM Set-2</b>	<b>GM1</b>	0.261	0.025	0.047
<b>GM Set-2</b>	<b>GM2</b>	0.257	0.018	0.048
<b>GM Set-2</b>	<b>GM3</b>	0.259	0.013	0.039
<b>GM Set-2</b>	<b>GM4</b>	0.262	0.023	0.094
<b>GM Set-2</b>	<b>GM5</b>	0.260	0.018	0.055
<b>GM Set-2</b>	<b>GM6</b>	0.260	0.016	0.040
<b>GM Set-2</b>	<b>GM7</b>	0.258	0.023	0.070
<b>GM Set-2</b>	<b>Average</b>	<b>0.259</b>	<b>0.019</b>	<b>0.056</b>

When examining the displacement time history data obtained from experiments conducted under strong ground motion, it was determined that the displacement capacity of 0.25 m, which is the design limit value of the seismic isolation unit, was exceeded in all loading protocols applied. Upon reaching this limit displacement value, it was observed that the rolling element (steel ball) moving between the curved surfaces made impact effect with the edge frame defining the geometric limits of the isolator. The deterioration and irregularities in the hysteretic behavior of the isolator caused by this impact mechanism can be clearly seen in the plots presented in Figure 6.17. Following the impact moment, sudden changes occurred in the dynamic response of the system, and significant increases were recorded, particularly in rotational demands. This undesirable mechanical interaction and excessive rotational demands inevitably cause increases in inertial forces transmitted to the superstructure and base shear forces beyond what was anticipated.

The acceleration responses obtained from experiments conducted using the GM Set-2 ground motion set are presented in Figure 6.18 for the selected characteristic records. When examining the acceleration-time histories, it was determined that sudden and sharp spikes in the acceleration records occurred when the design

displacement capacity of the isolator unit was exceeded, as a result of the rolling element impacting the device's boundary frame.

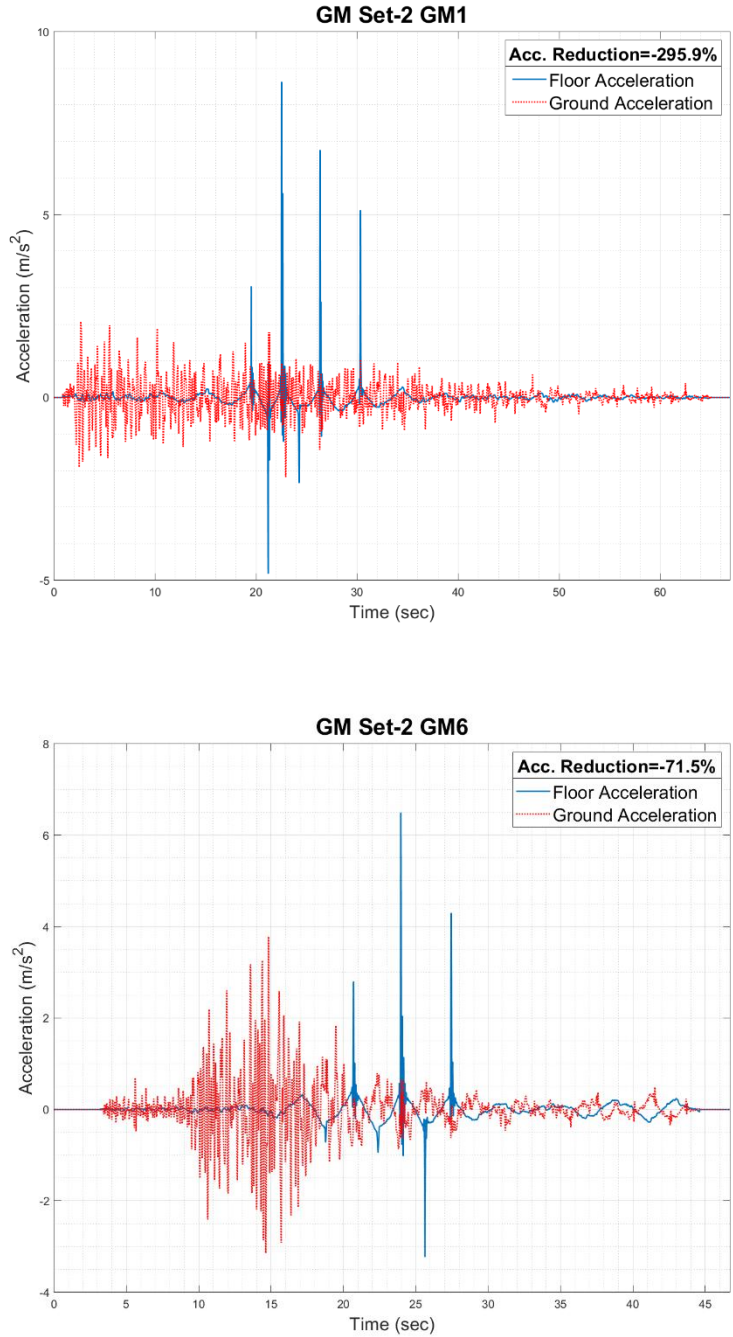


Figure 6.18 Acceleration responses for the second prototype obtained under selected strong ground motions from GM Set-2

Figure 6.18 illustrates the instantaneous acceleration spikes associated with the impact effect. The amplification in the maximum acceleration demands experienced by the superstructure upon the impact mechanism engaging has been quantitatively determined. The amplification in the isolated floor during the tests can be calculated using Equation 6.7.

$$Amplification = \frac{\max|\ddot{x}_{isolated\ floor}|}{\max|\ddot{x}_{ground}|} \quad (6.7)$$

The acceleration amplifications in the experiments conducted under GM Set-2 have been calculated by using Equation 6.7 and summarized in Table 6.12.

Table 6.12 Acceleration amplifications at isolated slab from experiments conducted with GM Set-2 acceleration records for the second prototype

<b>GM Set</b>	<b>Earthquake Code</b>	<b>Amplification</b>
<b>GM Set-2</b>	<b>GM1</b>	3.95
<b>GM Set-2</b>	<b>GM2</b>	3.52
<b>GM Set-2</b>	<b>GM3</b>	3.47
<b>GM Set-2</b>	<b>GM4</b>	2.81
<b>GM Set-2</b>	<b>GM5</b>	3.17
<b>GM Set-2</b>	<b>GM6</b>	1.72
<b>GM Set-2</b>	<b>GM7</b>	1.66
<b>GM Set-2</b>	<b>Average</b>	<b>2.90</b>

When the data in Table 6.12 was examined, it was determined that exceeding the design displacement limit of the isolator and the impact of the rolling element resulted in significant increases in acceleration demands. Specifically, for GM1 ground motion, it was observed that the maximum acceleration transmitted to the superstructure reached 3.95 times the peak acceleration of the strong ground motion. In other words, acceleration amplification at the seismic isolation interface occurred at approximately a 4 times floor acceleration. For the total of 7 strong ground motions evaluated within the scope of GM Set-2, it was calculated that the superstructure accelerations amplified by an average of 2.9 times due to the impact effect.

It is determined that the displacement capacity of the seismic isolator is exceeded in all applied strong ground motion scenarios for GM Set-2. Exceeding the capacity limit and the resulting impact mechanism negatively affect the seismic performance of the isolation unit. The findings reveal that this situation can lead to critical amplification of up to four times in the acceleration demands affecting the superstructure.

## **6.7 Discussion about the Test Results**

The experimental studies presented in this section aim to reveal the actual dynamic behavior of two different RRFI prototypes identified as a result of the analytical studies conducted in Chapter 3. Using an analytical model, two separate surface geometries with different performance targets in terms of acceleration reduction ratio and displacement capacity utilization ratio were defined; accordingly, two different RRFI prototypes were produced and experimentally tested. Thus, the validity of analytical predictions on the physical system could be directly evaluated.

In the first phase of the experimental program, force-deformation relationships were determined for both prototypes. These experiments are critical for revealing the effective stiffness of the isolator, the energy dissipation capacity, and its nonlinear character. The results obtained show that the RRFI exhibits approximately bilinear behavior at small displacement levels. In this region, the slope of the rolling surface is limited, so the effective stiffness of the system remains relatively constant, and a classic friction pendulum-like behavior is observed. However, as the displacement increases, the slope of the parabolic surface increases, the restoring force increases rapidly, and the system stiffness changes significantly. Therefore, at large displacement levels, it is not possible to represent the isolator behavior with a simple bilinear model; the system acquires a distinctly nonlinear character. However, at low displacement levels, the bilinear model represents the force-deformation relationship of the devices.

Free vibration tests have provided important information for determining the friction coefficient and effective damping ratio of the floor isolators. In the first prototype, the free vibration response of the system could be clearly observed, and the friction coefficient and damping ratio could be calculated using the logarithmic decay. In contrast, the second prototype exhibited overdamped behavior due to its flatter and rough surface. In this case, it was not possible to determine the friction coefficient and damping ratio using classical free vibration-based methods.

Harmonic tests were used to examine the frequency-dependent behavior of the floor isolators. In both prototypes, significant amplitude increases were observed when the applied harmonic excitation frequency approached the system's dominant vibration range, and the system approached a resonance-like behavior. An important feature is that parabolic surface isolators do not theoretically have a fixed natural period, because the surface slope and thus the effective stiffness vary with displacement. However, since the parabolic surface can be represented by equivalent radius in small displacement regions, an approximate fundamental period can be defined for the system in this region. The resonance tendencies observed in harmonic tests also correspond primarily to this equivalent period at small displacements.

Strong ground motion tests have constituted the most critical stage in evaluating the performance of isolators under realistic earthquake conditions. GM Set-1 was applied to both prototypes, enabling a direct comparison between the two systems. However, since the dominant periods of the two prototypes were different, GM Set-2, consisting of long-period ground motions, was additionally created for the second prototype. Detailed information on the selection criteria for strong ground motions was provided in Chapter 4. This approach aims to evaluate each prototype under strong ground motions compatible with its own dynamic characteristics.

The first prototype demonstrated highly successful performance, exhibiting high acceleration reduction ratios under GM Set-1, which was scaled close to its dominant period. In contrast, the second prototype failed to deliver the expected performance under GM Set-2, which was scaled to its fundamental period, and acceleration

reduction was not observed. However, acceleration reduction performance of the second prototype is better than the first prototype under GM Set-1, but this does not provide a meaningful comparison. The main reason for this is that GM Set-1 is not compatible with the dominant period of the second prototype and, therefore, the system has not been tested under the most challenging dynamic conditions realistically. Therefore, the high acceleration reduction ratios obtained under GM Set-1 do not represent the behavior of the second prototype. Consequently, the final product determined in the study was selected considering the reasons discussed above.

In conclusion, the findings obtained in Chapter 6 reveal that the performance of RPFIs is highly sensitive not only to the surface geometry but also to the match between the dominant period corresponding to this geometry and the spectral content of the applied seismic input. This situation clearly demonstrates the critical importance of jointly evaluating analytical modeling and appropriate earthquake sets in the design of RPFIs.

## CHAPTER 7

### SUMMARY AND CONCLUSION

In this study, a rolling-type parabolic-surface floor isolator (RPFI) has been developed to protect non-structural elements from seismic effects. The mechanical properties of the developed system have been thoroughly investigated using analytical and experimental methods. The primary objective of the study is to propose an alternative solution that can directly and effectively reduce the accelerations affecting non-structural components located on floors. The proposed floor isolator aims to reduce the accelerations experienced by valuable equipment in critical structures such as data centers, hospitals, and electrical transmission facilities during earthquakes. In this context, unlike the spherical or conically surfaced rolling-type floor isolators commonly used in the literature, a floor isolator design with a parabolic surface geometry has been proposed.

Within the scope of the study, an analytical study was first conducted. For this purpose, the system's equation of motion was derived based on the dynamic behavior of a ball rolling on a parabolic surface. The Newmark method was used to solve the obtained equation of motion under strong ground motions. Following the Newmark solutions performed by using earthquake records selected to be compatible with the target design spectrum, acceleration reduction ratios and displacement capacity utilization ratios were calculated for different parabolic surfaces. Taking these parameters into account, two different prototypes meeting the target performance criteria were identified.

Based on the findings obtained from analytical studies, two RPFI prototypes with different parabolic surface equations were identified and manufactured. Within the scope of experimental studies conducted on the produced prototypes, hysteresis tests, free vibration tests, harmonic loading tests, and dynamic tests under strong ground

motions were performed. The experimental results demonstrated a strong correlation with the analytical model, thereby validating the suggested mathematical technique.

By analyzing the force-displacement curves obtained, information regarding the energy dissipation capacity of the proposed floor isolators was obtained. Furthermore, bi-linear models for the devices were created using the force-deformation curves. Following experiments and analytical studies, it was observed that the RRFI converges to a spherical surface at small displacements. In this case, the parabolic surface could be represented by an equivalent radius, and the force-deformation curve could be modeled bilinearly. These models form the basis for creating numerical models in future studies. The damping ratio of the devices was determined through free vibration experiments. It was also observed that the damping ratio is dependent on the equation of the parabolic surface.

Experiments conducted under harmonic loads measured the responses of the RRFI at different frequencies under dynamic effects. These responses showed that the system's displacement demand increased at harmonic loads close to the fundamental vibration period of the RRFI. As the frequency deviates from the fundamental vibration period, it was observed that the displacement demand increases very rapidly and is at very low levels. This situation indicates that RRFI has an approximate fundamental period because the parabolic surface approximates the spherical surface at small displacements. Since the parabolic surface is represented by an approximate equivalent radius at small displacements, there is a fundamental vibration period. This situation indicates that RRFI behaves like a spherical surface at small displacements.

Strong ground motion tests have been decisive in evaluating the performance of RRFI under realistic seismic effects. In the experiments conducted under GM Set-1, it was observed that both the first and second prototypes significantly reduced the accelerations transmitted to the isolated floor. For particular records in the second prototype, the acceleration reduction ratio reached 90%. However, it should be emphasized that these high acceleration reduction values cannot be directly used for

the selection of the final prototype. The main reason for this is that the scaled period range of GM Set-1 is not compatible with the fundamental vibration period of the second prototype. Therefore, the results obtained under GM Set-1 do not represent the behavior of the second prototype under realistic dynamic conditions. The ground motion set that should be primarily evaluated for the performance of the second prototype is GM Set-2, which is scaled to be close to the fundamental vibration period. In the experiments conducted with GM Set-2, it was observed that the second prototype could not provide the expected acceleration reduction. On the contrary, it caused acceleration amplifications in the isolated floor under some records. These findings clearly demonstrate that the second prototype cannot provide the desired seismic protection performance under long-period ground motions. In contrast, the first prototype exhibited consistent and high acceleration reduction performance under GM Set-1, scaled to its dominant period, and the experimental results were found to be consistent with analytical predictions. Therefore, when all findings from the strong ground motion tests are evaluated together, it is concluded that the first prototype represents a more balanced, reliable, and successful design for a RRFI.

The results of this study represent an important step in revealing the fundamental mechanical and dynamic properties of the RRFI. However, some areas for improvement are also clearly evident for future studies. Firstly, all experiments conducted were performed using a single-axis shaking table in this study. This approach provided an adequate and appropriate framework for determining the isolator's dominant horizontal rolling behavior, recall mechanism, and acceleration reduction capacity, as well as for validating the analytical model. However, considering that roll-based systems may exhibit multi-axial excitations, simultaneous rotational movements, and interactions between directions under real earthquake effects, conducting multi-axial dynamic tests would allow for a more comprehensive understanding of the isolator's actual behavior. Another important issue that stands out for future studies is the development of a direct damping model for parabolic surface floor isolators. The damping calculation used in this study was adapted to the parabolic surface geometry based on approaches commonly used in

the TEC (2018) for friction pendulum-type isolators. It is clear that the damping mechanism has a more complex structure due to the variable slope of the parabolic surface. Therefore, the development of new damping definitions based on experimental and analytical foundations specific to RPFIs is considered an important research topic for the future. Furthermore, since this study was conducted in the context of floor isolators, the experiments and analyses were primarily limited to relatively small displacement levels. Within this displacement range, the parabolic surface geometry converges towards the spherical surface in terms of behavior, and the advantages of the variable slope of the parabolic surface are not fully represented. Future studies involving the development and testing of prototypes with greater displacement capacities will enable clearer observation of the advantages offered by parabolic surfaces, particularly at large displacements, such as increased stiffness and restoring force. In this case, since the bi-linear model used for small displacements will be insufficient, a new force-deformation model for RPFIs can be implemented in future studies. Thus, the actual effect of the parabolic surface can be observed in performance.

The results of this study demonstrate that RPFIs based on rolling principles offer a strong alternative to traditional rolling-based floor isolators. The ability to adjust the system's dynamic properties through a single geometric parameter provides significant design flexibility and enables the optimization of isolator performance according to different earthquake hazard levels and usage scenarios. Furthermore, the proposed system's entirely passive nature eliminates the need for an external energy source and complex control algorithms, offering significant advantages in terms of reliability and applicability.

In conclusion, this study introduces a new surface geometry to the field of rolling-based floor isolation. The analytical modeling, experimental validation, and performance evaluation of RPFIs provide a unique contribution to the literature. The findings demonstrate that RPFIs offer an effective solution for the seismic protection of non-structural components.

## REFERENCES

- ANSYS. (2023). ANSYS Inc.
- Bin, P., & Harvey, P. S. (2022). A dual-mode floor isolation system to achieve vibration isolation and absorption: Experiments and theory. *Journal of Sound and Vibration*, 525. <https://doi.org/10.1016/j.jsv.2022.116757>
- Chopra, A. K. (2020). *Dynamics of Structures* (5th ed.). Pearson Education Limited.
- Chung, L. L., Yang, C. Y., Chen, H. M., & Lu, L. Y. (2009). Dynamic behavior of nonlinear rolling isolation system. *Structural Control and Health Monitoring*, 16, 32–54. <https://doi.org/10.1002/stc.305>
- Cui, S. (2012). *Integrated Design Methodology For Isolated Floor Systems In Single-Degree-of-Freedom Structural Fuse Systems*. The University at Buffalo, State University of New York.
- Cui, S., & Bruneau, M. (2008, October). Experimental Study of Isolated Floor Systems. *The 14th World Conference on Earthquake Engineering*.
- Design Specification for Electrical Transmission Systems and Communication Facilities Under Earthquake Effects*. (2021). Ministry of Energy and Natural Resources.
- Gavin, H. P., & Zaicenco, A. (2007). Performance and reliability of semi-active equipment isolation. *Journal of Sound and Vibration*, 306(1–2), 74–90. <https://doi.org/10.1016/j.jsv.2007.05.039>
- Harvey, P. S., & Gavin, H. P. (2013). The nonholonomic and chaotic nature of a rolling isolation system. *Journal of Sound and Vibration*, 332(14), 3535–3551. <https://doi.org/10.1016/j.jsv.2013.01.036>

- Harvey, P. S., Zéhil, G. P., & Gavin, H. P. (2014). Experimental validation of a simplified model for rolling isolation systems. *Earthquake Engineering and Structural Dynamics*, 43(7), 1067–1088. <https://doi.org/10.1002/eqe.2387>
- Ismail, M., Rodellar, J., & Ikhouane, F. (2009). An innovative isolation bearing for motion-sensitive equipment. *Journal of Sound and Vibration*, 326(3–5), 503–521. <https://doi.org/10.1016/j.jsv.2009.06.022>
- Ivovich, V. A., & Savovich, M. K. (2001). Isolation of floor machines by lever-type inertial vibration corrector. *Structures & Buildings*, 146(4), 391–402. <https://doi.org/10.1680/stbu.2001.146.4.391>
- Kaatsız, K., Alici, F. S., & Erberik, M. A. (2024). Seismic Assessment of Electrical Equipment in Power Substations: A Case Study for Circuit Breakers. *Turkish Journal of Civil Engineering*, 35(4), 49–68. <https://doi.org/10.18400/tjce.1241107>
- Koumoussis, V., & Moysidis, A. (2019). On the dynamic behavior of nonlinear lightweight isolator for museum artifacts. *Soil Dynamics and Earthquake Engineering*, 117, 251–262. <https://doi.org/10.1016/j.soildyn.2018.09.011>
- Lin, P.-Y., & Loh, C.-H. (2008). Semi-active control of floor isolation system using MR-damper. *Sensors and Smart Structures Technologies for Civil, Mechanical, and Aerospace Systems 2008*, 6932, 69320U. <https://doi.org/10.1117/12.776095>
- López-Almansa, F., Yazgan, A. U., & Benavent-Climent, A. (2013). Design energy input spectra for high seismicity regions based on Turkish registers. *Bulletin of Earthquake Engineering*, 11(4), 885–912. <https://doi.org/10.1007/s10518-012-9415-2>
- Mahmoud, H., & Chulawat, A. (2015, August). Floor Slab Isolation for Mitigating the Seismic Response of Building Systems. *6th International Conference on Advances in Experimental Structural Engineering*.

- Manfredi, G. (2001). Evaluation of seismic energy demand. *Earthquake Engineering & Structural Dynamics*, 30(4), 485–499. <https://doi.org/10.1002/eqe.17>
- MATLAB* (R2024b). (2024). MathWorks Inc.
- Miranda, E., Mosqueda, G., Retamales, R., & Pekcan, G. (2012). Performance of nonstructural components during the 27 February 2010 Chile earthquake. *Earthquake Spectra*, 28(1), 453–471. <https://doi.org/10.1193/1.4000032>
- Morales, E., Filiatrault, A., & Aref, A. (2018). Seismic floor isolation using recycled tires for essential buildings in developing countries. *Bulletin of Earthquake Engineering*, 16, 6299–6333. <https://doi.org/10.1007/s10518-018-0416-7>
- Nacamuli, A. M., & Sinclair, K. M. (2011). Seismic Isolation: Applications of WorkSafe Technologies Ball-N-Cone Isolator. *Structures Congress 2011*, 852–863.
- PEER-NGA. (2024). <https://ngawest2.berkeley.edu/>.
- Shi, Y., Becker, T. C., Furukawa, S., Sato, E., & Nakashima, M. (2014). LQR control with frequency-dependent scheduled gain for a semi-active floor isolation system. *Earthquake Engineering and Structural Dynamics*, 43(9), 1265–1284. <https://doi.org/10.1002/eqe.2352>
- Solidworks*. (2024). Dassault Systèmes.
- Sucuoğlu, H., Erberik, M. A., Kaatsız, K., & Alıcı, F. S. (2021, October). Seismic Assessment of Electric Transmission Systems. *6th International Conference on Earthquake Engineering and Seismology*.
- TEC. (2018). *Turkish Earthquake Code for Buildings*. Disaster and Emergency Management Directorate.
- Vargas, B. A. C., Harvey, P. S., Cao, L., Ricles, J. M., Al-Subaihawi, S., & Villalobos Vega, E. (2022). Characterization and real-time hybrid simulation testing of rolling pendulum isolation bearings with different surface treatments.

- Earthquake Engineering and Structural Dynamics*, 51(11), 2668–2689.  
<https://doi.org/10.1002/eqe.3694>
- Vargas, R. E., & Bruneau, M. (2006). *Experimental Investigation of the Structural Fuse Concept*.
- Walsh, K. K., Marin-Artieda, C., & McElroy, K. (2024). Adaptive Passive Seismic Isolation System for Mitigating the Acceleration Response of Floor-Nouted Equipment. *Journal of Structural Engineering*, 150(1).  
<https://doi.org/10.1061/jsendh.steng-12688>
- Xu, Y. L., & Li, B. (2006). Hybrid platform for high-tech equipment protection against earthquake and microvibration. *Earthquake Engineering and Structural Dynamics*, 35(8), 943–967. <https://doi.org/10.1002/eqe.564>
- Xu, Y. L., Yu, Z. F., & Zhan, S. (2008). Experimental study of a hybrid platform for high-tech equipment protection against earthquake and microvibration. *Earthquake Engineering and Structural Dynamics*, 37(5), 747–767. <https://doi.org/10.1002/eqe.784>
- Zavala, E., Proaño, R., Torres, M., Estacio, L., & Garcia, F. (2020, September). Floor Isolation System for Museum Contents. *17th World Conference on Earthquake Engineering, 17WCEE*.